UNIVERSITY OF CALIFORNIA SAN DIEGO

Toward Practical Deployment of Photoacoustic Imaging

A dissertation submitted in partial satisfaction of the
requirements for the degree Doctor of Philosophy

in

Nanoengineering

by

Ali Hariri

Committee in charge:

Professor Jesse V. Jokerst, Chair
Professor James Friend
Professor David J. Hall
Professor Nisarg Shah
Professor Donald Sirbuly

2021

The Dissertation of Ali Hariri is approved, and it is acceptable in quality and form for publication on microfilm and electronically:

University of California San Diego

2021

TABLE OF CONTENTS

LIST OF FIGURES

ACKNOWLEDGEMENTS

This PhD journey was full of seemingly unsolvable challenges; however, I was extremely fortunate to have meaningful guidance and assistance from my mentors and colleagues, ultimately leading to my success.

First off, I must acknowledge my research mentor Professor Jesse V. Jokerst. He took a chance on me as a transfer from Wayne State University and taught me an incredible amount from scratch in our research field. There were days when Professor Jokerst would use his personal time to teach me techniques like large animal handling for 3 hours. His dedication and passion for science has truly inspired me to keep learning and continuously challenge myself. In addition to his impeccable scientific coaching, Professor Jokerst encouraged me to learn about commercializing research products and allowed me to intern at a biotechnology company, which was critical for my career development. I am extremely grateful for his scientific, moral, and financial support throughout my PhD study.

My committee members: Professor James Friend, Professor David J. Hall, Professor Donald Sirbuly, and Professor Nisarg Shah additionally gave me very helpful direction and guidance for my research.

My lab mates have been of tremendous help as well. I want to thank Dr. Anantha Krishnan and Dr. Soundaram Jeevarathinam for their chemistry education and constant encouragement. I would never have been able to publish that many papers without their help. In addition, Dr. Junxin Wang, Dr. Fang Chen, and Dr. Jeanne E. Lemaster are exceptionally bright researchers and helped me during many experiments, especially because of their creativity in research projects.

Special thanks to my current lab mates Dr. Jorge Palma, Colman Moore, and Yash Mantri. They included me in their research projects and helped me both in terms of learning new concepts and most importantly in terms of emotional support, particularly in the difficult years we faced. I would not have been able to be this successful in my PhD program without their assistance.

Most importantly, I want to thank my dearest parents, my two brothers, and the love of my life, Laila. My family's constant encouragement and insightful suggestions were what led me to success. The essential rules for life I learned always inspired me to seek novel solutions to address difficult problems. My loved ones taught me to never give up, even in the hardest of times, and making them proud has been my ultimate goal in life. That solid foundation is what has truly led me to where I am today.

Finally, I want to make professional acknowledgements to my collaborators:

Chapter 2, in full, is a reprint of the material as it appears in *Photoacoustics* 9 (2018): 10-20. Ali Hariri , Jeanne Lemaster , Junxin Wang , AnanthaKrishnan S. Jeevarathinam , Daniel L. Chao , and Jesse V. Jokerst. The dissertation author was the primary investigator and author of this paper.

Chapter 3, in full, is a reprint of the material as it appears in *Biomedical Optics Express* 11, no. 6 (2020): 3360-3373.. Ali Hariri, Kamran Alipour, Yash Mantri, Jurgen P. Schulze, and Jesse V. Jokerst. The dissertation author was the primary investigator and author of this paper.

Chapter 4, in full, is a reprint of the material as it appears in *Scientific* 9, no. 1 (2019): 1-10. Ali Hariri, Eric Zhao, Ananthakrishna Soundaram Jeevarathinam, Jeanne Lemaster, Jianjian Zhang, and Jesse V. Jokerst. The dissertation author was the primary investigator and author of this paper.

Chapter 5, in full, is a reprint of the material as it appears in *Wound Repair and Regeneration*, 27, no. 5 (2019): 488-496. Ali Hariri, Fang Chen, Colman Moore, Jesse V. Jokerst. The dissertation author was the primary investigator and author of this paper.

Chapter 6, in full, is a reprint of the material as it appears in *Photoacoustics*, 22, p.100245. Ali Hariri, Jorge Palma Chavez, Keith A. Wear, T. Joshua Pfefer, Jesse V. Jokerst, William C. Vogt. The dissertation author was the primary investigator and author of this paper.

VITA

2013	BSc in Biomedical Engineering, Amirkabir University of Technology
2014	MSc in Biomedical Engineering, Sharif University of Technology
2017-2021	Research Assistant, University of California San Diego
2021	PhD in Nanoengineering, University of California San Diego

ABSTRACT OF THE DISSERTATION

Toward Practical Deployment of Photoacoustic Imaging

by

Ali Hariri

Doctor of Philosophy in Nanoengineering

University of California San Diego, 2021

Professor Jesse V. Jokerst, Chair

Photoacoustic imaging is an emerging modality which the combination of ultrasound and optical imaging. The combination of these two techniques has many advantages including no use of ionizing radiation compared to radiography, high-resolution deep tissue imaging versus optical coherence tomography (OCT), and higher contrast and faster scanning compared to MRI. Most current equipment uses sophisticated and complicated OPO lasers with tuning and stability features inconsistent with broad clinical deployment. Low fluence illumination sources can facilitate clinical transition of photoacoustic imaging because they are rugged, portable, affordable, and safe. In this dissertation, I will present characterization of the commercial available light emitting diode (LED) based photoacoustic imaging in terms of system specifications, light source characterizations, photoacoustic spatial/temporal resolution, and penetration. Since low fluence

light source based photoacoustic imaging devices generate low image quality, I will propose a denoising method using a multi-level wavelet-convolutional neural network to map low fluence illumination source images to its corresponding high fluence excitation map. This part of dissertation will show qualitative and quantitative improvements up to 2.20, 2.25, and 4.3-fold for peak signal-to-noise ratio (PSNR), similarity structural index measurement (SSIM), and contrast-to-noise ratio (CNR) metrics. Next, after improving and enhancing the low fluence light source photoacoustic imaging systems, we report molecular and functional imaging application for LED-based photoacoustic imaging . We demonstrate detection of reactive oxygen and nitrogen species (RONS) with a near-infrared (NIR) absorbing small molecule (CyBA) and LED-based photoacoustic imaging equipment. CyBA produces increasing photoacoustic signal in response to peroxynitrite ($ONOO^-$) and hydrogen peroxide (H_2O_2) with photoacoustic signal increases of 3.54 and 4.23-fold at 50 μM of RONS at 700 nm, respectively. We also introduced photoacoustic imaging as a non-invasive method for detecting early tissue damage that cannot be visually observed while also staging the disease using quantitative image analysis. Finally, Here we introduce polyacrylamide (PAA) hydrogel as a candidate material for fabricating stable phantoms with well-characterized optical and acoustic properties that are biologically relevant over a broad range of system design parameters. These phantoms may also facilitate future standardization of performance test methodology.

Chapter 1 Introduction of Photoacoustic Imaging

1.1 Principle

Photoacoustic Imaging (PAI) is an efficient, noninvasive, and three dimensional imaging modality capable of imaging organs, tissues, and cellular structures with high resolution. It combines the technological advances of both optical and acoustic imaging[1]. PAI exploits the high intrinsic contrast of optical imaging and the spatial resolution of ultrasound imaging. Every material, including bodily substances, has a physiologically specific optical absorption coefficient. It is unique to the endogenous chromospheres of every cell or tissue at a particular wavelength. The substance to be imaged is illuminated by a nanosecond pulsed laser of a specific wavelength at which the absorption coefficient of the subject is highest. This helps in generating images of highest contrast and resolution. In order to generate the PAI the pulse width should be shorter than thermal and stress relaxation time[2] (Equation 2 and 1 respectively) which are based on the physical characteristics of the object and time scale of energy dissipation.

$$T_S = \frac{d}{v} \tag{1}$$

$$T_{th} = \frac{d^2}{4\alpha} \tag{2}$$

Where “d” is the characteristic dimension of the tissue being heated and “α” is the thermal diffusivity of the sample.

The photon absorption by the subject causes a transient temperature change (Equation (3)) which leads to expansion (Equation (4)), thereby producing photoacoustic waves (Equation (5)). These acoustic waves are detected by the ultrasonic transducer.

$$P_0 = \Gamma . A(r) \tag{3}$$

$$\Gamma = \frac{\beta V^2}{C_p} \tag{4}$$

$$\left(\nabla^2 - \frac{1}{v^2}\frac{\partial^2}{\partial t^2}\right) p(r,t) = -\frac{\beta}{C_p}\frac{\partial H}{\partial t} \tag{5}$$

A(r) is the absorbed optical energy density and Γ is the dimensionless Grueneisen parameter. β is the thermal coefficient of volume expansion and C_p is the specific heat capacity at constant pressure and light absorption $H(r,t)^2$. The strength of the PA signal is the product of the incident optical fluence and the absorption coefficient of the subject[3].

1.2 PAI Configurations

PAI is classified into 2 categories, Photoacoustic Computed Tomography (PACT) and Photoacoustic Microscopy (PAM). In PACT, light is diffused over the tissue generating acoustic waves acquired at various points outside the tissue boundary by means of a wideband ultrasound transducer[4]. The detection can be done by a single ultrasound transducer which rotates around the sample or a stationary ultrasound array of 128-256 element transducers. While the stationary array detection configuration offers high imaging speed, this array and the data acquisition unit required makes the system more expensive. The imaging speed of the single transducer configuration can be enhanced by employing a light source with a high repetition rate. Image reconstruction is required to obtain the generated photoacoustic signal from the subject. PACT is employed to image internal organs, skin, and breast and brain while in PAM, the light is focused on the microscopic area to image the cell structures and vasculature with high resolution.

PAM is an appealing imaging modality as it gives detailed information on structural, functional, and molecular aspects[5, 6] of biological samples both in vivo and ex vivo [7]. It appears to be promising in both research and clinical diagnosis[8, 9] as it delivers high resolution, three dimensional images and is a noninvasive procedure. Its application includes vascular biology [10-12], oncology [13, 14], neurology[15, 16], ophthalmology[17, 18], dermatology [19-22], gastroenterology[23-25], and cardiology [26, 27]. PAM provides information on tissue components and the dynamic interactions by magnifying microscopic cellular and subcellular features. PAM is compatible with optical coherence tomography and fluorescence imaging, thus the combination can deliver multimodal images that provide comprehensive anatomic and functional characterization of tissues. This multimodal imaging technique is able to provide both the optical scattering and optical absorption information of a subject simultaneously. Acoustic Resolution-PAM (AR-PAM) and Optical Resolution-PAM (OR-PAM) are the two categories of PAM technology. In the AR-PAM the ultrasound transducer is tightly focused to a microscopic point making it suitable for deep tissue imaging as it provides a penetration depth up to several centimeters. Contrastingly, OR-PAM provides a high focused laser beam providing much higher lateral resolution. In OR-PAM the penetration depth is limited up to one optical transport mean free path [28]. The axial resolution in AR-PAM depends on the ultrasound speed in the tissue and the frequency bandwidth of the transducer [28] . Typically an OR-PAM offers a lateral resolution of 2.6um and a penetration depth of 1.2 mm [29]. Reflection and transmission modes are the two detection configurations of OR-PAM. In the reflection mode, the excitation and the detection occurs on the same side of the sample while in the transmission mode the detection and the reflection are on opposite sides of the subject. The transmission mode offers better lateral resolution and is limited to imaging thin tissues [30-32] whereas the reflection mode provides good axial resolution and is suitable for imaging thick tissues [32-36]. The photoacoustic A-lines contain the signals time of arrival information thus representing the optical properties of the tissue as a function of depth [33].

1.2 PAI Light Sources

Biomedical applications employ lasers as the source of excitation because of its specificity, coherence, and energy. PAI widely uses solid state lasers and dye lasers because of the shorter pulse width and large pulse energy. However, these are not favorable for clinical application as they are bulky, expensive, and require high maintenance. Furthermore In contrast, the diode lasers are compact, inexpensive, and have a high repetition rate for faster imaging. Diode lasers are semiconductor P-N junction diodes that employ current as the pump source. Unlike other classes of lasers, this type of Pulsed Laser Deposition (PLD) is portable sized and requires low operating voltages. Nevertheless, the PA signal needs to be averaged multiple times for an acceptable Signal to Noise Ratio (SNR) as the peak output power of PLD is typically <200W [37-39]. This results in slower imaging speeds.

Chapter 2 The Characterization of an Economic and Portable LED-based Photoacoustic Imaging System to Facilitate Molecular Imaging

Photoacoustic imaging (PAI) is a non-invasive, high-resolution hybrid imaging modality that combines optical excitation and ultrasound detection. PAI can image endogenous chromophores (melanin, hemoglobin, etc.) and exogenous contrast agents in different medical applications. However, most current equipment uses sophisticated and complicated OPO lasers with tuning and stability features inconsistent with broad clinical deployment. As the number of applications of PAI in medicine increases, there is an urgent need to make the imaging equipment more compact, portable, and affordable. Here, portable light emitting diode - based photoacoustic imaging (PLED-PAI) was introduced and characterized in terms of system specifications, light source characterizations, photoacoustic spatial/temporal resolution, and penetration. The system uses two LED arrays attached to the sides of a conventional ultrasound transducer. The LED pulse repetition rate is tunable between 1K Hz, 2K Hz, 3K Hz, and 4K Hz. The axial resolution was 0.268 mm, and the lateral resolution was between 0.55 and 0.59 mm. The system could detect optical absorber (pencil lead) at a depth of 3.2 cm and the detection limits of indocyanine green (ICG) and methylene blue (MB) were 9 μM and 0.78 mM, respectively. *In vivo* imaging of labeled human mesenchymal stem cells was achieved to confirm compatibility with small animal imaging. The characterization we report here may have value to other groups evaluating commercially available photoacoustic imaging equipment.

2.1 Introduction

Photoacoustic imaging (PAI) is a non-invasive, and non-ionizing imaging modality based on optical absorption/excitation and ultrasound detection [40]. It offers the contrast and spectral behavior of optical imaging combined with the high penetration depth and spatial resolution of acoustic imaging due to weak ultrasound scattering in biological tissue. In PAI, tissue is illuminated by a nanosecond laser pulse. Endogenous or exogenous molecules will absorb this incident energy to produce a fast local temperature increase; acoustic waves then propagate inside the tissue due to thermal expansion. Wideband ultrasound transducers can detect photoacoustic signal via trans-abdominal [41] or intra-vascular [42] settings, and the combination of PAI with ultrasound can offer functional details as well as anatomical and structural information [43, 44]. This high-resolution modality has been used to image endogenous chromophores (melanin, hemoglobin, etc.) and exogenous contrast agents [45] in different medical applications including molecular imaging [46-49], oncology [13, 50], ophthalmology [51, 52], cardiology [26], and neurology [15, 53].

When selecting a photoacoustic excitation source, one should consider the pulse width of the light source, the pulse energy, repetition rate, wavelength, and the spectral width of the source. These should be compared to the absorption behavior of the target tissue/contrast agent. High energy Nd:YAG lasers are the most common PAI excitation sources. These lasers generate 4-7 ns pulses with mJ energy levels. The repetition rates are limited to between 10-30 Hz. NIR optical parametric oscillator (OPO) or dye lasers are the most common [4]. However, dual modality imaging systems (ultrasound/photoacoustic) with these lasers are bulky, expensive, and suffer from wavelength and power intensity fluctuations. These systems typically use a laser enclosure system to shield the operator from the incident irradiation, but this is cumbersome and prevents the operator from directly interacting with the sample or subject. While miniaturized OPOs offer a small footprint [54, 55], they remain delicate and expensive and require regular maintenance.

To overcome these limitations, pulse laser diodes (PLD) have been utilized as an illumination light source in different PAI configurations such as optical resolution microscopy (OR-

PAM) [39, 56] and photoacoustic computed tomography (PACT) [5, 57]. For example, Daoudi et al. [58], developed a compact and ergonomic handheld dual modality (ultrasound/photoacoustic) probe using PLD with axial resolution of 0.28 mm and lateral resolution between 0.4 mm and 0.6 mm as well as considerable penetration depths (15 mm). More recently, light emitting diodes (LEDs) have also been used for PAI [59]. These inexpensive, compact, and multi-wavelength LED-based designs were shown in Allen et al. [60], and Adachi et al. [61] for photoacoustic microscopy (PAM).

Indeed, LEDs solve many issues in the clinical translation of PAI. Most importantly, they offer a significant reduction in cost, are significantly more stable than OPO-based systems, and take up only a fraction of the space. This stability and reduced footprint makes LED-based systems portable [62]. Furthermore, LEDs do not have to be in a light-tight enclosure, which can restrict many clinical procedures. There are several clinical examples were this would be useful including the gastrointestinal imaging of Zhang et al. [63] and the brain resection work of Kircher et al. [64].

In addition, we [65] and others [66, 67] have recently utilized photoacoustic imaging techniques for real-time monitoring of therapeutics or disease biomarkers such as circulating tumor cells, heparin, or lithium [68, 69]. These applications are ideally suited for LED-based illumination because they need low cost and portable excitation sources. They perturb only the first few millimeters of tissue, and thus do not require the high energy of OPO-based lasers. Thus, this work with wearable photoacoustic imaging applications motivated us to pursue a commercially available LED-based photoacoustic scanner.

In this chapter, we characterize a commercially available LED-based photoacoustic system, defined here as a portable LED-based photoacoustic imaging (PLED-PAI). In the following sections, we describe system specification, light source characterization, photoacoustic spatial/temporal resolution, and penetration depth. We then report this system's performance with common exogenous photoacoustic contrast agents including pilot rodent *in vivo* applications.

2.2 Methods and Materials

2.2.1 System Description

The PLED-PAI consists of an optical path and an acoustic path and was purchased from Prexion Corporation. (Tokyo, Japan; **Figure 1**). High density, high power light emitting diodes (Prexion Corporation, Tokyo, Japan) are used as an excitation source. Two LED arrays are attached to either side of an ultrasound transducer. Each LED array includes 4 rows of 36 single embedded LEDs. Each LED array has 2 rows with 850 nm excitation and 2 rows with 690 nm excitation. One array is placed on each side of the transducer for four rows at each wavelength (**Fig. 1D**). Each LED array head has dimensions of 12.4 mm (height), 86.5 mm (length), and 10.2 mm (width). The LED pulse width can be changed from 50 ns – 150 ns with a 5 ns step size. The LED pulse repetition rate is tunable between 1K Hz, 2K Hz, 3K Hz, and 4K Hz; the temporal resolution is dependent on choice of repetition rate. Photoacoustic signals are generated after each LED pulse. The 128 elements of the linear array transducer detect the photoacoustic signal in parallel and this reconstructs one frame. The frame rate in PLED-PAI is equal to the LED repetition rate because it has parallel acquisition channels in this system.

LED systems have lower power, and averaging is used to minimize noise. This affects the frame rate. There are a defined number of averages that change as a function of LED pulse repetition rate. In turn, these averaging options define the frame rate and temporal resolution. Options include: 1K Hz (32, 64, 96, 160, 320, 640, 1600, 3200, and 6400 averages), 2K Hz (64, 128, 192, 320, 640, 1280, 3200, 6400, and 12800 averages), 3K Hz (128, 192, 320, 640, 1280, 3200, 6400, and 12800 averages), and 4K Hz (128, 256, 384, 640, 1280, 2650, 6400, 12800, and 25600 averages). Therefore, the PLED-PAI can have frame rates of 30 Hz, 15 Hz, 10Hz, 6 Hz, 3 Hz, 1.5 Hz, 0.6 Hz, 0.3 Hz, and 0.15 Hz. There are different methods rather than averaging to minimize the noise. Golay codes [70], empirical mode decomposition (EMD)[71], wavelet-based methods, and Wiener deconvolution have been applied to low SNR photoacoustic and are reported in the literature [72, 73].

The acoustic path uses an ultrasound pulse/receive linear array transducer with 128 channels and central frequency of 10 MHz with bandwidth of 80.9%. (PreXion Corporation , Tokyo, Japan). Each element is 3.5 mm long with a pitch of 0.3 mm. An acoustic lens focuses the ultrasound at ~15 mm. The maximum ultrasound detection depth is 38 mm. The data acquisition unit has a dynamic range of 16 bits with 1024 samples for each element. The sampling rates of the photoacoustic and ultrasound modalities are 40 MHz and 20 MHz, respectively. The LED driver triggers and synchronizes the illumination and ultrasound detection (**Figure 1A**). The photoacoustic signals are generated and stored after each LED pulse. B-mode photoacoustic and ultrasound images are reconstructed using a delay-and-sum (DAS) [74] and Fourier transform analysis (FTA) [75]. The transducer can be scanned in one direction to acquire three-dimensional (3D) data.

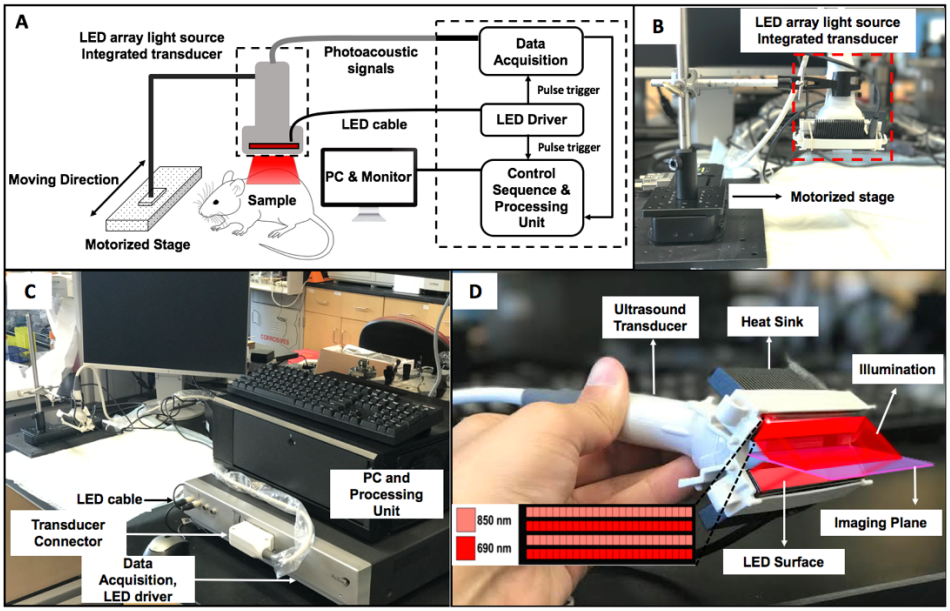

Figure 2. 1 Schematic and photograph of LED-based photoacoustic system. A) Schematic of the PAI system using LED array light source. B) Photograph of PLED-PAI probe associated with motorized stage. C) Whole imaging setup includes PC and processing unit, data acquisition, LED driver, ultrasound transducer, LED light source, and motorized stage. D) PLED-PAI probe with imaging plane and illumination source are shown schematically. LED array design is also shown in the inset—there were alternating rows of LEDs with different wavelengths.

2.2.2 LED Beam Characterization

LED beam Profile. To evaluate the excitation sources, parallel lines were printed 2 mm apart on transparency films and placed inside a 1% agar phantom **(Figure 2A)**. The PLED-PAI was placed 2 cm from the lines. Thus, identical absorbers with the same thickness values at the same depth were used to characterize the LED light source based on the photoacoustic signal that they produce. The probe scans in one direction using a motorized translation stage (OptoSigma Corporation, CA, USA) for 10 mm. A maximum intensity projection (MIP) was used to reconstruct the 3D image. To analyze each line in the MIP, we converted the MIP image to an 8-bit TIFF file using ImageJ 1.48v [76]. Ten different regions of interest (ROI) were used to measure the accumulative photoacoustic intensity on each line.

LED power and stability. To measure the LED stability, a photodiode sensor was positioned 5 mm from the LED sources (small aperture (1 cm) photodiode sensor (S120C, Thorlabs Inc., USA)). We studied the LEDs at four different repetition rates (1, 2, 3, and 4K Hz) while immersed in water (for 500 s) and air (for 200 s)**.** The temperature of the LED surface and the heat sink was recorded. The power delivered from the LED arrays was calculated using a standard photodiode sensor (S120C, Thorlabs Inc., USA) at 690 and 850 nm.

2.2.3 Photoacoustic Spatial Resolution

Axial resolution. To measure the axial resolution, a black human hair was embedded inside a 1% agar phantom. A bright field microscopy imaging system (Life Technologies Inc., Ca, USA) was used to calculate the hair diameter (100.15 ± 5.60 μm) (**Figure 3A**). The hair was positioned 2 cm below the transducer. Photoacoustic images were reconstructed using FTA methods for all conditions (1K Hz (32, 64, 96, 160, 320, 640, 1600, 3200, and 6400 averages), 2K Hz (64, 128, 192, 320, 640, 1280, 3200, 6400, and 12800 averages), 3K Hz (128, 192, 320, 640, 1280, 3200, 6400, and 12800 averages), and 4K Hz (128, 256, 384, 640, 1280, 2650, 6400,

12800, and 25600 averages)). The axial profile was plotted and fitted to a Gaussian distribution. The full width half maximum (FWHM) was calculated using MATLAB software (MathWorks Inc.).

Lateral resolution. To characterize the lateral resolution, parallel lines (150 μm wide) with different distances (from 1.1 mm to 0.55 mm) were printed on a transparency film (**Figure 4A**). After placing the transparency films at various distances inside 1% agar, photoacoustic images were acquired using PLED-PAI with FTA image reconstruction. Bright field microscopy was used to measure the accurate spacing between lines, and PAI line profiles were used to measure the lateral resolution.

2.2.4 Photoacoustic Penetration Depth

To evaluate the PLED-PAI system penetration depth, chicken breast tissue was used as a scattering media. A single pencil lead (0.5 mm HB, Newell Rubbermaid, Inc., IL, USA) was inserted inside chicken breast as an optical absorber at different distances from the transducer surface **(Figure 5A)** [77]; 850 nm LEDs were used as the illumination source. This sample was scanned at different depths (1.8 cm, 2.4 cm, and 3.2 cm) with different frame rates (30 Hz, 15 Hz, 10 Hz, 6 Hz, 3 Hz, 1.5 Hz, 0.6 Hz, 0.3 Hz, and 0.15 Hz). To have a more realistic absorber, ten μL blood were placed inside Teflon light wall tubes (Component Supply Company, FL, USA). These were scanned at a depth of 1.5 and 2.2 cm with different frame rates. Contrast is defined as a ratio of photoacoustic () and background noise () intensity in the photoacoustic image (). The photoacoustic images are reconstructed using FTA methods.

To measure the signal and the noise, a window of 4 pixels × 4 pixels was placed where the image has a high photoacoustic intensity, and the mean intensity of the pixels in this 4 x 4 area was calculated. The same procedure was utilized to measure the background noise intensity: a 4 pixel × 4 pixel window was positioned 2 mm away from the object, and the background noise

intensity mean values are measured—contrast values above 3 are considered recognizable **(Figure 5G)**.

2.2.5 Exogenous Contrast Agent in Photoacoustic Imaging

Indocyanine green (ICG) (Chem-Impex Int'l Inc., IL, USA), methylene blue (MB) (Fisher Science Education Inc., PA, USA), and 1,1'-dioctadecyl-3,3,3',3'-tetramethylindo-tricarbocyanine iodide (DiR) (Biotium Inc., CA, USA) were purchased and dissolved in deionized (DI) water (ICG and MB) or dimethyl sulfoxide (DMSO) (DiR). Ten μL of each solution (36 μM, 18 μM, and 9 μM ICG; 1.5 mM, 0.75 mM, and 0.37 mM MB; and 136 μM, 68 μM, and 136 μM DiR) were used for photoacoustic imaging. Samples were placed inside Teflon light wall tubes (Component Supply Company, FL, USA) and positioned under 1 cm layer of 2% intralipid (20%, emulsion, Sigma-Aldrich Co, MO, USA) mixed with agar. Water or DMSO served as controls. ICG and DiR used 850 nm excitation, and MB used 690 nm excitation. All samples were scanned at a depth of 10 mm from the transducer, and a MIP was used to reconstruct the images. We repeated this at higher concentrations (640 μM, 320 μM, and 160 μM ICG; 6 mM, 3 mM, and 1.5 mM MB; and 592 μM, 296 μM, and 148 μM DiR). ImageJ 1.48v was used to do statistical analysis. Ten different regions of interest (ROI) were used to measure the average photoacoustic intensity for each sample.

2.2.5 *In vivo* Imaging Using PLED-PAI

All animal experiments were performed in compliance with the Institutional Animal Care and Use Committee established by University of California San Diego. Male mice were anesthetized with 2.5% isofluorane in oxygen at 1.5 L/min.

Poietics human mesenchymal stem cells (HMSCs; Lonza, PT-2501, NJ, USA) were grown in supplemented media (Lonza, PT-3001, NJ, USA) and seeded in a T75 flask at a concentration

of 5000 cells/cm^2. Cells (400,000) were labeled with 9.8 mM DiR and incubated under standard conditions for 20 min. The HMSCs were washed with PBS to remove free nanoparticles and detached using TrypLE Express (Life Technologies Inc., Ca, USA). Then, 100 μL of three different materials such as only DiR (positive control), HMSC labelled with DiR (DiR @ HMSC), and HMSC (negative control) were subcutaneously injected on the spinal cord of male mice as an in- vivo experiment. B-mode photoacoustic/ultrasound images were reconstructed using the FTA algorithm.

2.3 Results and Discussion

2.3.1 LED Beam Characterization

The beam characterization is divided into three parts: LED beam profile, illumination stability, and LED power. We first measured the consistency of the LED illumination power across the scanning area, i.e., the beam profile. Since 70 ns pulse width has almost the highest LED fluence for both 690 and 850 nm **(Figure 2B)**, we used this number as pulse width in all experiments. The temporal shape of excitation pulses and LED spectrums are shown in **Supplementary Figure 1S A, B, C**. The power from the LED arrays at 690 nm and 850 nm with 70 ns as pulse width was measured to be 9.85 mW/cm^2 (2.6 μJ/cm^2 per pulse) and 31.55 mW/cm^2 (9 μJ/cm^2 per pulse), respectively for 4 K Hz repetition rate. **Figure 2C** shows the MIP image of the printed transparency. **Figure 2D** is a line profile along the dotted line on **Figure 2C.** The photoacoustic intensities were averaged and are shown in **Figure 2E** for each line. The error bars show the standard deviation along all intensities and ROIs. The average intensity of lines 3 through 14 (6 mm from either side of the transducer) is 18.43% higher than the values seen on the sides (**Figure 2D, E**).

Next, the stability of the LED (850 nm) intensity was measured with a variation (between maximum power and minimum power) of 13.64%, 14.46%, 20.86%, and 25.35% for 1K Hz, 2K Hz, 3K Hz, and 4K Hz, respectively, in air (**Figure 2F)**. In water, the variation is 8.88%, 10.34%,

12.57%, and 15.27% for 1K Hz, 2K Hz, 3K Hz, and 4K Hz, respectively (**Figure 2H)**. The maximum (Max), minimum (Min), mean, and standard deviation (Std.) of the power in water (**Figure 2G)** and air (**Figure 2I)** are reported. There was a 14 ^{o}C temperature increase in the heatsink at a repetition rate of 4K Hz; at 1K Hz this was only 3.5 ^{o}C. For all conditions, we noticed a slight temperature increase (0.2-0.8 degree Celsius) on the actual LED surface.

The LED beam profile is a critical part of PAI systems, and light should be distributed equally on the sample. Different studies have reported different homogenized lateral illumination area. In the first report of handheld ultrasound/photoacoustic using a Q-switched laser, Niederhauser et al. [78] showed a homogenous illumination with a lateral size of 25 mm. Kolkman et al. [43] described a dual modality scanner with 20 mm as the lateral beam size by Nd:YAG laser. Daoudi et al. [58], reported 23 mm lateral beam size for their handheld probe integrating laser diode. The data in **Figure 2D, E** show a homogenous beam over ~25 mm, which is comparable to the literature.

The temperature increase is due to the increased number of pulses—a higher repetition rate means a higher number of pulses in a specific time. In LEDs, the p-n junction diode emits light when activated, and LED light output varies as a function of this junction temperature. This local temperature increase is the main reason for LED power variations. Daoudi et al. [58] mentioned 5 to 10 degree in about 2 minutes of firing with repetition rate of 10K Hz. Here, we noted that the PLED-PAI heatsink increased by 14 ^{o}C at a repetition rate of 4K Hz; however, only a 0.2-0.8 Celsius temperature increase was observed on the LED surface.

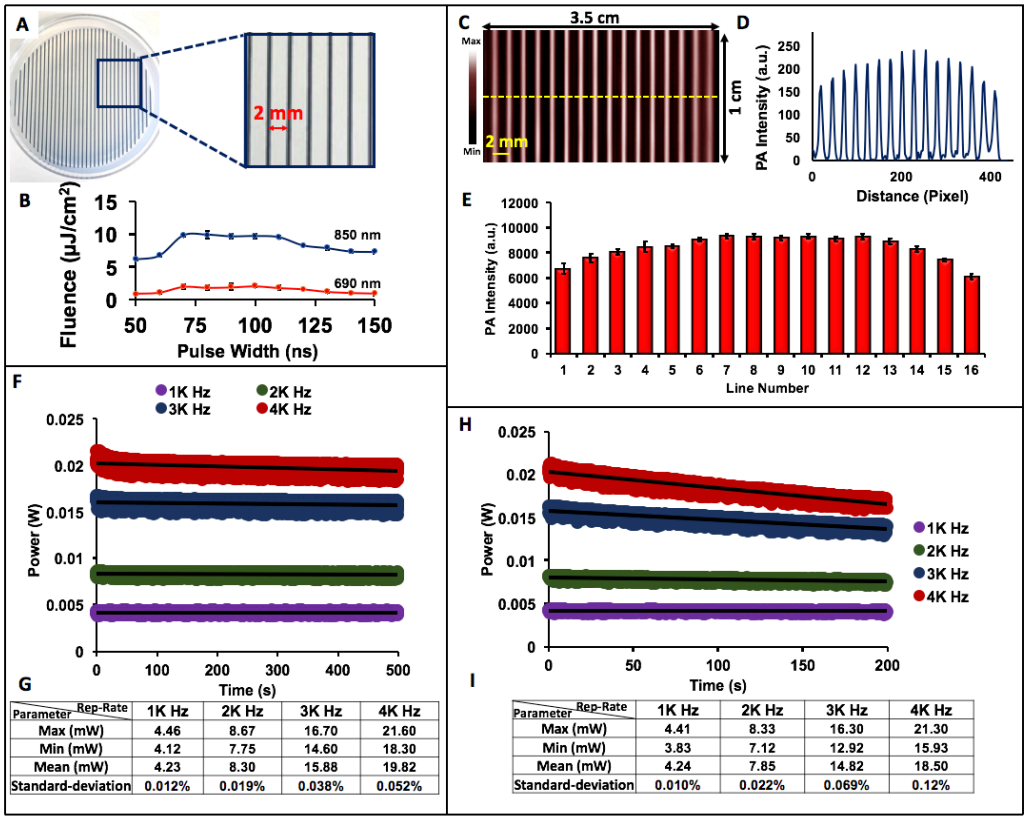

Parameter / Rep-Rate	1K Hz	2K Hz	3K Hz	4K Hz
Max (mW)	4.46	8.67	16.70	21.60
Min (mW)	4.12	7.75	14.60	18.30
Mean (mW)	4.23	8.30	15.88	19.82
Standard-deviation	0.012%	0.019%	0.038%	0.052%

Parameter / Rep-Rate	1K Hz	2K Hz	3K Hz	4K Hz
Max (mW)	4.41	8.33	16.30	21.30
Min (mW)	3.83	7.12	12.92	15.93
Mean (mW)	4.24	7.85	14.82	18.50
Standard-deviation	0.010%	0.022%	0.069%	0.12%

Figure 2. 2 LED beam characterizations of PLED-PAI system. A) Parallel lines were printed on transparency film and placed inside 1% agar. The distance between the lines is 2 mm. B) LED fluence per pulse versus pulse width for 690 and 850 nm. C) MIP image for sixteen parallel lines with a scan size of 10 mm. D) The line profile along the dotted line in C. E) Statistical analysis of each line and the averaged PA intensity along all sixteen lines. Error bars show standard deviation between different ROIs in each printed line. F) LED power stability (in different repetition rates) versus time when PLED-PAI is placed inside the water. G) LED power statistical parameters when PLED-PAI is in water for 500 s. H) LED power stability (in different repetition rates) versus time when PLED-PAI is placed inside the air. I) LED power statistical parameters for PLED-PAI in air for 200 s.

2.3.2 Photoacoustic Spatial Resolution

Spatial resolution is important for imaging systems and is defined as the ability to distinguish two small high contrast objects positioned very close together. **Figure 3B** shows the photoacoustic image of human hair inside agar phantom at a depth of 2 cm. The FWHM was calculated after preparing a Gaussian fit for axial resolution. This was defined as the axial resolution. Both lateral **(Figure 3C)** and axial (**Figure 3D)** profiles were analyzed for all conditions: 1K Hz (32, 64, 96, 160, 320, 640, 1600, 3200, and 6400 averages), 2K Hz (64, 128, 192, 320,

640, 1280, 3200, 6400, and 12800 averages), 3K Hz (128, 192, 320, 640, 1280, 3200, 6400, and 12800 averages), and 4K Hz (128, 256, 384, 640, 1280, 2650, 6400, 12800, and 25600 averages). The axial resolution for PLED-PAI is 268 μm (**Figure 3E)**, and there were no significant differences in lateral and axial profiles (**Figures 3C, D)**.

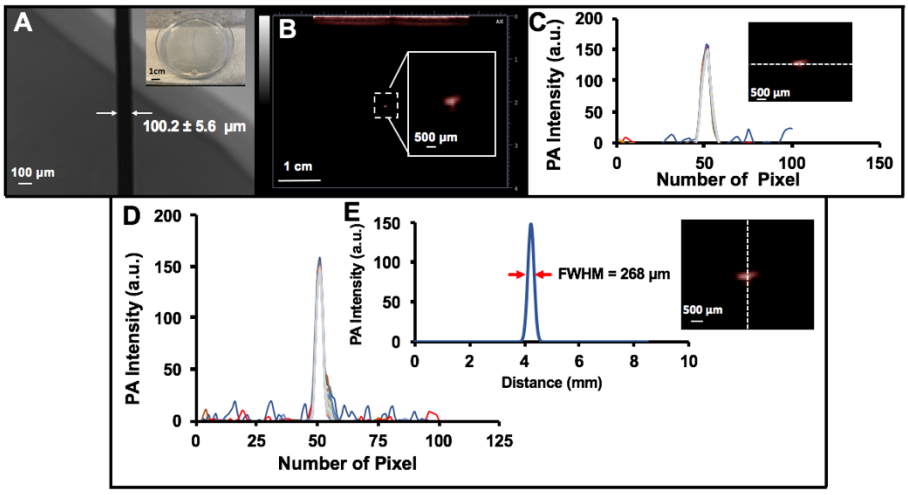

Figure 2. 3 Axial resolution by measuring photoacoustic point spread function using a human black hair. A) Photograph and bright field microscopy image of black hair inside 1% agar phantom. The thickness of the hair is 100.1 ± 5.6 μm. B) Photoacoustic image of hair. Image size is 3.5 cm × 4 cm. The image is reconstructed using the FTA algorithm. C) Lateral profile along dotted line for all conditions with different colors (1K Hz (32, 64, 96, 160, 320, 640, 1600, 3200, and 6400 averages), 2K Hz (64, 128, 192, 320, 640, 1280, 3200, 6400, and 12800 averages), 3K Hz (128, 192, 320, 640, 1280, 3200, 6400, and 12800 averages), and 4K Hz (128, 256, 384, 640, 1280, 2650, 6400, 12800, and 25600 averages). There is no significant difference in lateral profile in this phantom as a function of repetition rate or averages. D) Axial profile for all conditions with different colors. E) Fitted Gaussian distribution on the axial profile with measured FWHM. Axial resolution is 268 μm.

Figure 4B, C, D, E, and **F** show photoacoustic images acquired using PLED-PAI for samples with 1.1 mm, 0.83 mm, 0.75 mm, 0.59 mm, and 0.55 mm line spacing, respectively. Lateral line profiles were plotted for all samples. The 550 μm spacing cannot be resolved (**Figure 4G)**, but the 590 μm spacing can be distinguished (10 peaks/troughs seen in data, which corresponds to the number of parallel lines scanned). Thus, the photoacoustic lateral resolution is between 550 μm and 590 μm (**Figure 4G**). Importantly, these experiments used 70 ns pulse widths. By decreasing the pulse width and having higher frequency ultrasound transducers, we

could improve the lateral and axial resolutions. This work is underway. However, as we emphasized in the introduction, low spatial resolution photoacoustic data has utility in many photoacoustic sensing rather than true photoacoustic imaging.

Spatial resolution in PAI systems highly depends on laser pulse width and ultrasound transducer specification such as number of element, central frequency, and element size. Niederhauser et al. [78] measured the axial resolution of 300 µm with central frequency of 5.5 MHz for their handheld PAI system with near infrared red laser pulses (60 ns) as illumination source and detected individual blood vessels with range of 100-300 µm. Daoudi et al. [58] utilized a diode laser with pulse width of 130 ns as excitation source and 128 element with a length of 5 mm and central frequency 7.5 MHz as ultrasound detection reported 280 µm for axial resolution and wide range of 400 µm – 600 µm as lateral resolution. Kim et al. [79] calculated photoacoustic axial resolution of 400 µm for their handheld dual modality ultrasound/photoacoustic imaging system using a laser pulse of 6.5 ns and a central frequency of 5.5 MHz. Thus, we conclude that this system has spatial and axial resolution comparable to other handheld photoacoustic imaging tools.

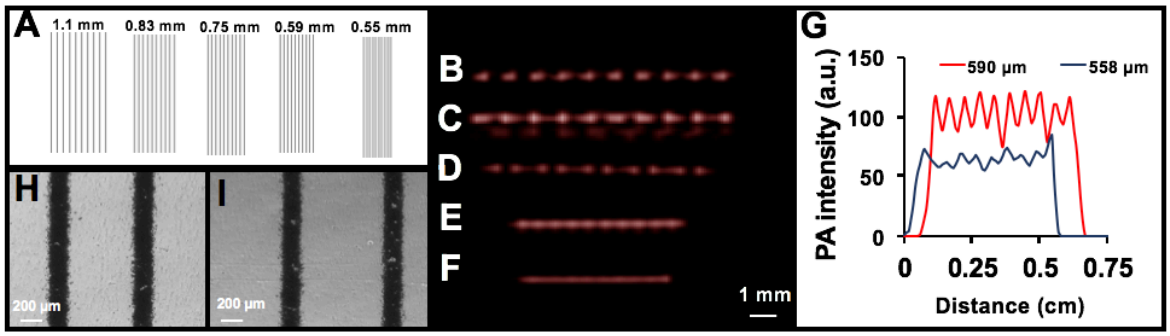

Figure 2. 4 Lateral resolution measurement of LED-based photoacoustic imaging system. A) Parallel lines with various spacing (1.1 mm, 0.83 mm, 0.75 mm, 0.59, and 0.55 mm) are printed on transparency film and placed inside 1% agar phantom. B) Photoacoustic image for 1.1 mm spacing between lines. C) 0.83 mm spacing. D) 0.75 mm. E) 0.59 mm. F) 0.55 mm. G) Lateral profile for two different samples (0.59 mm and 0.55 mm). This plot shows that LED-based photoacoustic imaging can distinguish lines when there is 0.59 mm spacing between lines. The 0.55 mm spacing cannot be resolved by this imaging system. H) Bright field microscopy image for 0.59 mm spacing. I) Bright field microscopy image for 0.75 mm spacing.

2.3.3 Photoacoustic Penetration Depth

The ability to penetrate deep into tissue is important for many imaging applications [80]. We hypothesized that the LED-based system would have lower penetration depth because of its lower energy relative to OPO-based systems. Our goal here was to quantify the exact depth in chicken tissue. The photoacoustic images are shown **Figure 5B, C, D, E,** and **G**, and the results illustrate that at 1.8 cm and 2.4 cm, the target (pencil lead) is recognizable for all frame rates from 30 Hz to 0.15 Hz **(Figure 5B, C)**. However, at 3.2 cm, the target is not detectable at 30 Hz, 15 Hz or 10 Hz **(Figure 5G)**, but can be seen at 3.2 cm with a frame rate of 6 Hz and lower because at lower frame rates there is more averaging, which increases contrast **(Figure 5D, E, F)**. **Figure 5H** shows contrast versus depth. **Figure 5I, J** show a photoacoustic image of a blood sample with a frame rate of 0.15 Hz at 1.5 and 2.2 cm, respectively. **Figure 5K** shows contrast versus two different depths of blood sample. The blood sample is detectable when the contrast is over than 3. The highest frame rate that could detect the blood sample was 1.5 Hz and 0.6 Hz at 1.5 cm and 2.2 cm, respectively. Error bars demonstrate the standard deviation along each measurement.

There are several parameters such as excitation source, excitation wavelength, transducer specification, and imaging target that have a significant effect on photoacoustic penetration depth. Kim et al. [79] demonstrated the capability of PAI using Nd:YAG laser to image 5.2 cm deep inside the tissue. Recently, Zhou et al. [80] showed capability of PAI to image a specific target (stable phosphorus phthalocyanine) through 11.6 cm of chicken breast. While Daoudi et al. [58] reported penetration depth of up to 1.5 cm (frame rate of 0.43 Hz, averaging were used to increase photoacoustic SNR) using diode laser in their handheld PAI setup. Here, we illustrated the capability of the PLED-PAI to detect a strong optical absorber (pencil lead) inside chicken breast up to 3.2 cm deep with a frame rate of 15 Hz.

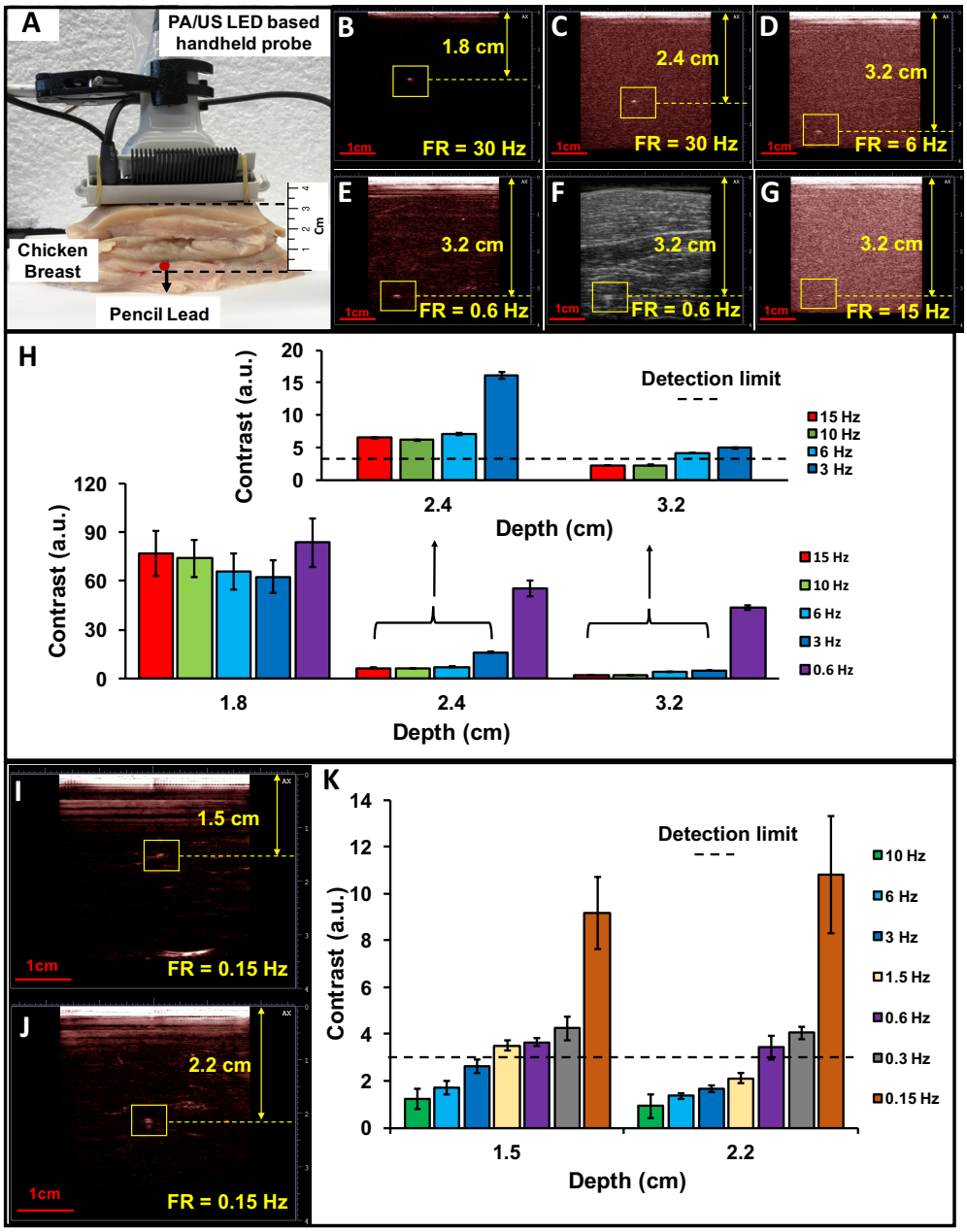

Figure 2. 5 Penetration depth measurement of PLED-PAI. A) Experimental configuration includes chicken breast tissue with pencil lead 3.2 cm deep. B) Photoacoustic image of pencil lead 1.8 cm deep with a frame rate (FR) of 30 Hz. C) Depth of 2.4 cm when FR = 30 Hz. D) Depth of 3.2 cm when FR = 6 Hz. By increasing the depth, the photoacoustic system acquires more averages (decrease the frame rate) to improve SNR. E) Depth of 3.2 cm when FR = 0.6 Hz. F) B-mode ultrasound image of pencil lead 3.2 cm deep with a frame rate of 0.6 Hz. The ultrasound resolution at 10 MHz does not clearly discriminate the target. G) Photoacoustic image of pencil lead 3.2 cm deep when FR = 15 Hz. The SNR decreases by increasing the frame rate. Object is poorly defined with low contrast. H) Signal to background noise as a function of depth and frame rate. Panels I-K are blood samples below chicken breast tissue. Panel I is a frame rate of 0.15 Hz. J) Photoacoustic image of blood sample 2.2 cm deep when frame rate of 0.15 Hz. K). Signal-to-background noise as a function of depth and frame rate for blood sample inside the chicken breast. If the contrast is lower than the detection limit (S/N < 3), then the specimen cannot be detected.

2.3.4 Exogenous Contrast Agent in Photoacoustic Imaging

Exogenous contrast agents can be targeted for specific molecules or cells for preclinical and clinical applications. Photoacoustic contrast agents have significant feasibility to assist in monitoring and diagnosis of diseases [81]. We characterized the detection limit of some common small molecules used in photoacoustic imaging: ICG, MB, and DiR. These are NIR-sensitive, Food and Drug Administration (FDA)-approved contrast agents for both fluorescent and photoacoustic imaging. Various concentrations were scanned, and the detection limits were calculated at three standard deviations above baseline. **Figure 6A, E, I** show MIP images of high concentrations of ICG (640 μM, 320 μM, and 160 μM), MB (6 mM, 3 mM, and 1.5 mM), and DiR (592 μM, 296 μM, and 148 μM). **Figure 6B, F, J** shows the average photoacoustic intensity along all ten ROIs for each tube associated with **Figure 6A, E, I.**

Figure 6C, G, K show MIP images for the detection limit of ICG (36 μM, 18 μM, 9 μM, and DI water), MB (1.5 mM, 0.75 mM, 0.37 mM, and DI water), and DiR (136 μM, 68 μM, 34 μM, and DMSO). **Figure 6D, H, L** show the average photoacoustic intensity along the ROIs. The error bars show the standard deviation between ROIs in each tube. The limit of detection for ICG, MB, and DiR is 9 μM, 0.75 mM, and 68 μM, respectively when 850 nm is used for ICG and DiR and 690 nm is utilized for MB. The power for the LED-based system at 690 nm is almost three-fold lower than that at 850 nm. This might explain the worse detection limit for MB rather than ICG and DiR. This experiment also highlights how LED-based systems are limited by the choice of wavelength. While OPO-based systems use a tunable wavelength, this system can only use two wavelengths. Thus, it can be challenging to carefully match the absorption peak of the contrast agent with the excitation source. Nevertheless, many species absorb strongly at 690 nm or 850 nm and customized LED sets are available for ratiometric imaging

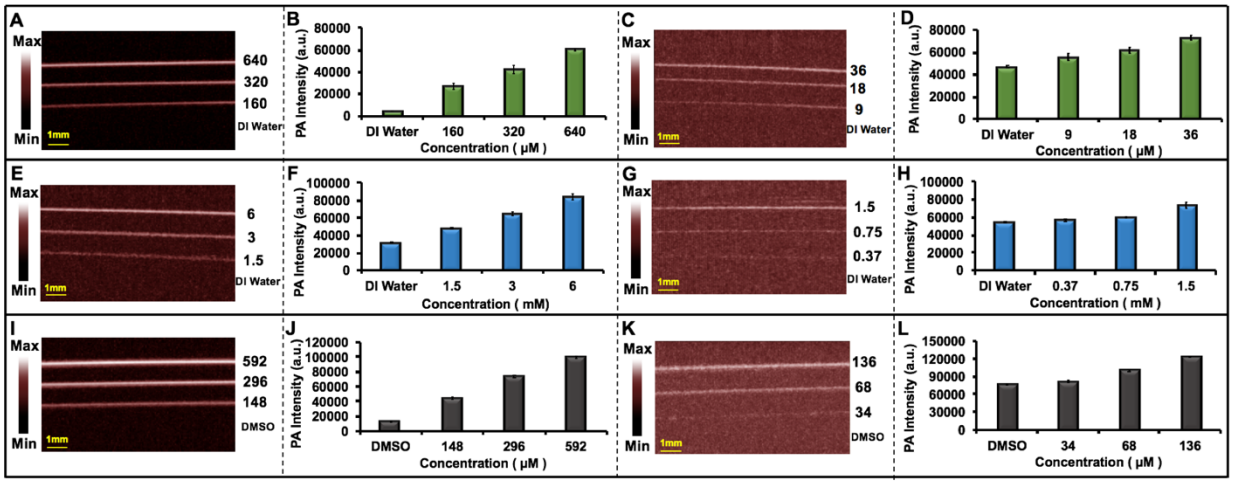

Figure 2. 6 Evaluation of LED-based photoacoustic imaging system for exogenous contrast agents. A) MIP image of ICG solutions (640 μM, 320 μM, 160 μM, and DI water) with high concentration as positive control inside Teflon light wall tubes. B) Statistical analysis of data in A. C) MIP image detection limit experiment for ICG (36 μM, 18 μM, 9 μM, and DI water). D) Statistical analysis of data in C. E) MIP images of MB solutions (6 mM, 3 mM, 1.5 mM, and DI water) with high concentration as positive control inside Teflon light wall tubes. F) Statistical analysis of data in E. G) MIP image detection limit experiment for MB (1.5 mM, 0.75 mM, 0.37 mM, and DI water). H) Statistical analysis of data in G. I) MIP images of DiR solutions (592 μM, 320 μM, 148 μM, and DMSO) with high concentration as positive control inside Teflon light wall tubes. J) Statistical analysis of data in I. K) MIP image detection limit experiment for DiR (136 μM, 68 μM, 34 μM, and DMSO). L) Statistical analysis of data in K. All the error bars demonstrate standard deviation between different ROIs in each tube. Scan size is 10 mm.

2.3.5 *In vivo* Imaging Using PLED-PAI

After measuring and evaluating the important features such as LED beam characterization, spatial and temporal resolution, penetration depth, and capability of detection exogenous contrast agent, we next performed *in vivo* experiments to demonstrate the feasibility of PLED-PAI for clinical applications. We and others [82, 83] have previously used photoacoustic imaging for stem cell imaging. Here, we used labeled cells to understand the *in vivo* performance of this LED-based system. We used DiR which has been demonstrated as an effective contrast agent for cells checking [84 85].

Figure 7A, E, I show photoacoustic images before injection of DiR, DiR @ HMSC, and HMSC, respectively. The needle generates strong photoacoustic signal and overlaying the

photoacoustic data with the ultrasound images offers more comprehensive structural information in addition to functional details from DiR-labeled cells. **Figure 7B, F, J** demonstrate B-mode photoacoustic/ultrasound images before injection. **Figure 7C, D** shows photoacoustic and photoacoustic/ultrasound images of injected DiR in the mice, respectively. These figures show strong photoacoustic signal in the presence of DiR. **Figure 7G** shows capability of PLED-PAI to detect cells labeled with contrast agent. DiR was used as contrast agent for labeling the HMSCs. Unlabeled HMSCs were also injected as control (**Figure 7K, L)**, but there was no increase in photoacoustic signal. Here we demonstrated the feasibility of PLED-PAI for *in vivo* studies including photoacoustic cell imaging.

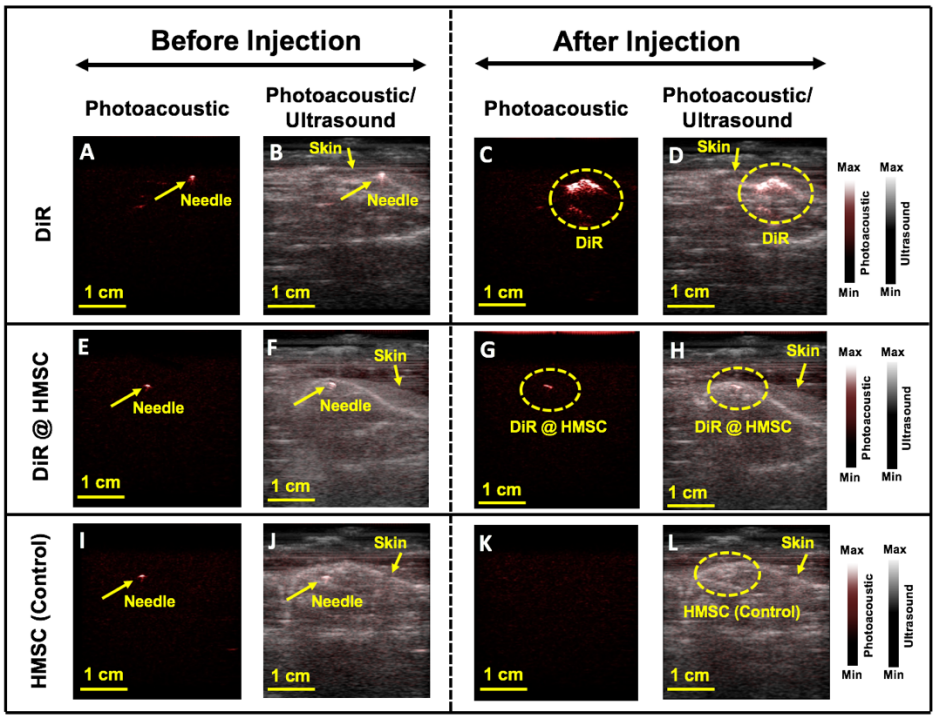

Figure 2. 7 *In vivo* evaluation of PLED-PAI. A) Photoacoustic image when needle is subcutaneously injected on spinal cord area before DiR injection. The needle has strong photoacoustic signal. B) Photoacoustic/ultrasound image of A. C) Photoacoustic image after subcutaneously injection of DiR. D) B-mode photoacoustic/ultrasound image of C. E) Photoacoustic image when needle is subcutaneously placed on the spinal cord area before HMSC labeled with DiR (DiR @ HMSC) injection. F) B-mode photoacoustic/ultrasound image of E. G) Photoacoustic image after injection of HMSC labeled with DiR (DiR @ HMSC) on spinal cord. H) B-mode photoacoustic/ultrasound image of G. I) Photoacoustic image in presence of needle before injection of unlabeled HMSC as control experiment. J) B-mode photoacoustic/ultrasound image of I. K) Photoacoustic image of HMSC as control. This image shows no photoacoustic signal for HMSC. L) B-mode photoacoustic/ultrasound image of K.

To further understand the clinical utility of the PLED-PAI, two more experiments were conducted. First, we studied a fresh enucleated rabbit eye embedded in 1% agar. **Figure 8A, B, C, D** demonstrate a B-mode ultrasound image, B-mode photoacoustic/ultrasound image using 690 nm, 850 nm, and concurrent 690 and 850 nm excitation, respectively. The retinal vessels are shown with a dotted yellow box 2 cm deep. Photoacoustic imaging of the two different wavelengths can facilitate retinal oxygen saturation measurements, but this is beyond the scope of this study. Second, PLED-PAI was utilized to image the superficial blood vessels from human volunteer wrist. **Figure 8E** shows the photoacoustic image of human wrist. Skin and vessels are shown with yellow arrows.

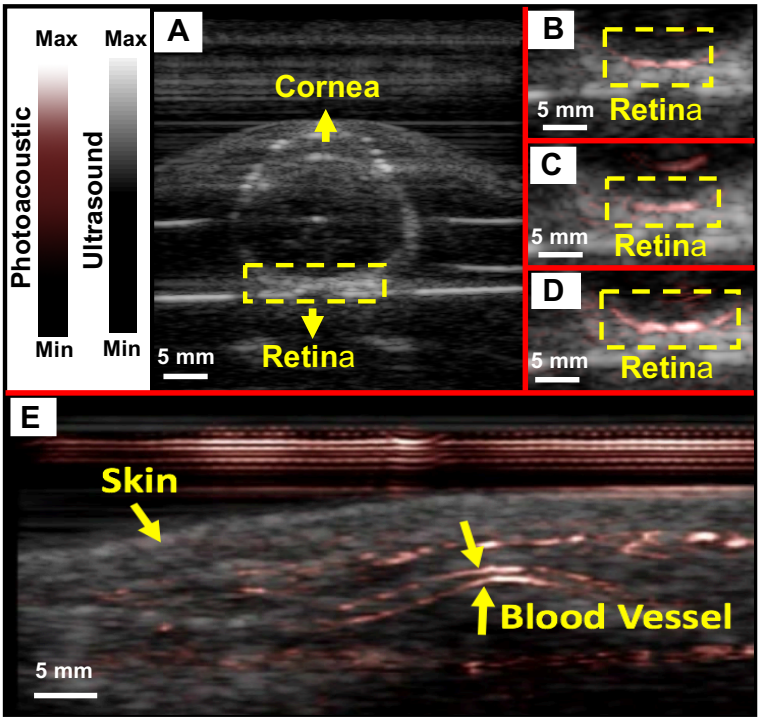

Figure 2. 8 Evaluation of PLED-PAI on rabbit eye. A) B-mode ultrasound image when fresh enucleated rabbit eye was embedded in 1% agar. **B)** B-mode photoacoustic/ultrasound image of rabbit eye using 690 nm. **C)** B-mode Photoacoustic/ultrasound image of rabbit eye using 850 nm**. D)** B-mode photoacoustic/ultrasound image when both 690 and 850 nm are used at the same time**.** Retinal vessels are imaged in depth of 2 cm. **E)** Photoacoustic image of skin and vasculature. Skin and blood vessel are shown using yellow arrows.

2.4 Conclusions

In this paper, we describe a portable LED-based dual modality (ultrasound/photoacoustic) PAI system. We characterized the LED beam profile and showed that a region up to 25 mm could be imaged with a homogenous plane of light. The lateral spatial resolution was 550 – 590 μm, and the axial resolution was 268 μm. Temporal resolution up to 30 Hz could be achieved with penetration depths of up to 2.4 cm for pencil lead. Blood is detectable upon to 2.2 cm through chicken breast tissue with a frame rate of 0.6 Hz. We used the PLED-PAI for three well-known exogenous contrast agents (MB, ICG, and DiR) and labeled cells and showed detection limits suitable for *in vivo* imaging. We also showed the feasibility of PLED-PAI for retinal vessel monitoring.

The use of LEDs as an illumination source introduces both limitations and advantages. First, the LEDs cannot be tuned, which eliminates photoacoustic spectroscopy. Second, the pulse width of the LED was 70 ns, which affects the stress confinement satisfaction and can impact the efficiency of acoustic wave generation. Third, LEDs have low power—this can limit penetration depth at fast frame rates or temporal resolution at low frame rates. However, there are also many advantages to these systems including a significant decrease in cost, smaller footprint, lack of laser calibration and monitoring, and no need for optical goggles or light-tight shields. Thus, LED-based systems are ideal for personalized or wearable photoacoustic equipment, and we imagine that this technology could have broad utility in a number of therapeutic drug monitoring applications.

Chapter 2, in full, is a reprint of the material as it appears in *Photoacoustics* 9 (2018): 10-20. Ali Hariri , Jeanne Lemaster , Junxin Wang , AnanthaKrishnan S. Jeevarathinam , Daniel L. Chao , and Jesse V. Jokerst. The dissertation author was the primary investigator and author of this paper.

Chapter 3 Deep Learning Improves Contrast in Low-Fluence Photoacoustic Imaging

Low fluence illumination sources can facilitate clinical transition of photoacoustic imaging because they are rugged, portable, affordable, and safe. However, these sources also decrease image quality due to their low fluence. Here, we propose a denoising method using a multi-level wavelet-convolutional neural network to map low fluence illumination source images to its corresponding high fluence excitation map. Quantitative and qualitative results show a significant potential to remove the background noise and preserve the structures of target. Substantial improvements up to 2.20, 2.25, and 4.3-fold for PSNR, SSIM, and CNR metrics were observed, respectively. We also observed enhanced contrast (up to 1.76-fold) in an in vivo application using our proposed methods. We suggest that this tool can improve the value of such sources in photoacoustic imaging.

3.1 Introduction

Photoacoustic imaging (PAI) combines the high-contrast of optical imaging and the high spatial resolution of ultrasound [40, 86, 87]. Short optical pulses serve as an excitation source in PAI systems [5] to generate photoacoustic waves via thermoelastic expansion [88, 89]. Wideband ultrasonic transducers detect the propagated waves, and mathematical processing methods (reconstruction algorithms) can transform the detected signals into an image [90-94]. Over the last decade, investigators have demonstrated various applications of PAI in ophthalmology [52, 95, 96], oncology [97-99], dermatology [100-102], cardiology [103-105], etc.

PAI traditionally uses solid-state lasers as an excitation source because of their tunability, coherence, and high pulse energy. However, utilization of these lasers is difficult in clinical applications because they are bulky, expensive, unstable (in terms of power intensity fluctuation), and require frequent maintenance [106]. In contrast, pulse laser diodes (PLD) [39, 56, 57] and light emitting diodes (LED) [107-109] are a stable, affordable, and compact alternative light source. However, the output pulse energy of PLDs and LEDs is low—on the order of μJ/pulse and nJ/pulse versus mJ/pulse with lasers. Thus, the resulting photoacoustic data needs be averaged hundreds of time to cancel the noise and extract meaningful signal [107]. Unfortunately, performing many averages negatively affects the temporal resolution. Investigators have improved the signal-to-noise ratio (SNR) using classical signal processing methods such as empirical mode decomposition (EMD) [110, 111], wavelet-based methods [112, 113], Wiener deconvolution [114], principle component analysis (PCA) [115], and adaptive noise canceler (ANC) [116, 117]. However, these methods all require some prior information about the signal and noise properties, which is a significant limitation. Therefore, new tools to increase the SNR in low fluence PLD and LED PAI are needed.

Deep learning is rapidly expanding within various fields and improving performance in pattern recognition and machine learning applications. These relatively new techniques have vastly outperformed other classical methods in recent years. For example, computer vision has

extensively utilized deep learning algorithms object detection, image classification, and image reconstruction [118-121]. Convolutional neural networks (CNN) are among the most popular deep learning algorithms [122].

In medical imaging, previous studies focused on denoising CT-specific noise patterns. Kang et al. [123] utilized CNNs for wavelet transform coefficients with low-dose CT images. Chen et al. [124] used CNNs to directly map low-dose CT images to their normal-dose counterparts. Other methods altered the original CNN architecture to either preserve details in the image through *residual* blocks [125, 126] or *generator* CNNs to produce the restored image based on encoded features of low-dose images [127-129].

To capture more spatial context, previous approaches used pooling between convolution to reduce feature map resolution. However, pooling extends the receptive field and depth of their CNNs to drastically increase the computational costs in training and deploying such models [130]. Dilation [131] is another alternative to pooling but is limited by sparse sampling in the input layer, which can lead to gridding issues [132].

The concept of denoising in PA images is similar to low-dose CT yet the noise can have very different patterns; hence, the noise requires a different transfer method to be removed. Some of the earlier methods used short-lag spatial coherence [133, 134] or singular value decomposition (SVD) [135] to remove reflection artifacts from PA images. Some recent approaches utilize CNNs to identify point sources per image [136, 137] or use recurrent neural networks (RNN) to leverage temporal information in PA images to remove artifacts [138]. Antholzer et al. [139] adopted U-net architectures to reconstruct photoacoustic tomography (PAT). Anas et al. [140] utilized skip connections in dense convolutional networks to improve the quality of the PA images.

The potential of deep learning to enhance image quality motivates this work with a deep convolutional neural network. The goal is to map the low-fluence light photoacoustic images to corresponding high-fluence photoacoustic data. We demonstrated that deep learning can restore the images in low-fluence photoacoustic configuration with less computational cost than classical

methods. Here, we first describe the proposed deep convolutional neural network and training details. We then demonstrate qualitative and quantitative phantom results. Finally, we show the capability our proposed model to image low concentrations of contrast agents *in vivo*.

3.2 Methods and Materials

3.2.1 Training

The main aim of this study is to train the proposed convolutional network (MWCNN) to transform the low-fluence photoacoustic data into high-fluence images. We defined the high fluence images as the ground truth and then used TiO_2-based optical scatters to reduce the laser fluence (**Figure 1A**). The laser fluence was 17, 0.95, 0.25, 0.065, and 0.016 mJ/pulse at a wavelength of 850 nm with 0, 4, 6, 8, and 10 mg/ml of TiO_2, respectively (**Figure 7**). Importantly, we did not change the imaging setup in either the acoustic or optical path. We simply changed the disks without touching the transducer or the 3D samples. To further confirm that now changes were caused when switching the disks, we selected some landmarks on the first and last frames and compared those landmark among all the filters. There were no significant movements of these landmarks. Network training used a 3D pen print (Gincleey 3D Pen, AM3D Printers Inc.) to prepare a complicated 3-dimensional structure (2 cm x 2 cm x 3 cm) (**Figure 1B**). These structures were placed in an agarose phantom and scanned (30 mm, 270 frames) with all five optical filters on top of them (**Figure 1C**). We used 0 mg/ml which has the highest laser fluence (~17 mJ/pulse) as a ground truth in the proposed network. **Figure 1D** shows that the signal-to-noise ratio will decrease by decreasing the laser fluence (increasing the TiO_2 concentration).

In the training process, 85% of the frames (with fluence values of 17, 0.95, 0.25 mJ/pulse) were randomly selected as training set and the rest as test set. The training algorithm was implemented under the PyTorch platform using two NVIDIA GeForce GTX 1080 Ti GPUs. We used ADAM optimizer for our training algorithm with an initial learning rate of . The training process completed 256 epochs in one day.

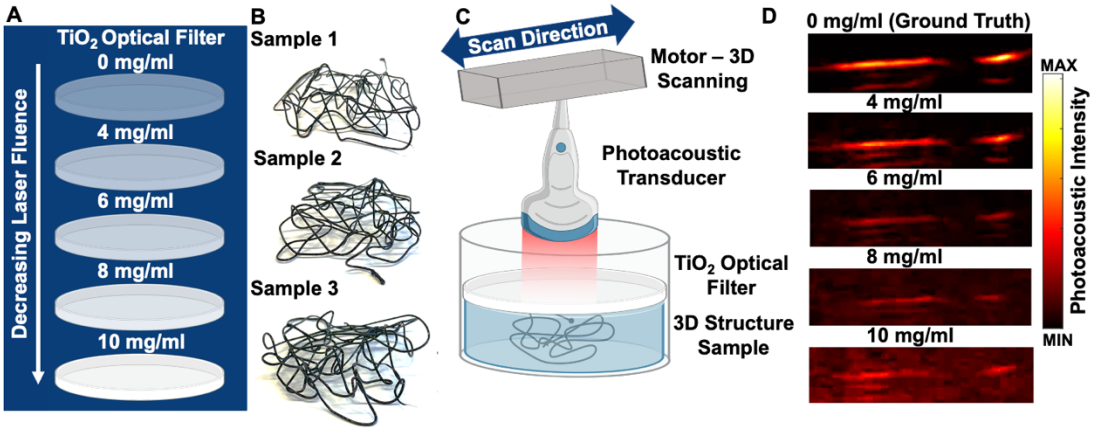

Figure 3. 1 Experimental training setup. A) TiO_2-based optical scattering gels reduce the laser fluence. The laser fluence at wavelength of 850 nm was 17, 0.95, 0.25, 0.065, and 0.016 mJ/pulse after using 0, 4, 6, 8, and 10 mg/ml of TiO_2, respectively. B) Three different complicated 3D structures were made using a 3D pen print to collect training data. C) Imaging setup—the 3D structures are placed in the agarose phantom with a TiO_2-based optical scatter on top. We scanned the entire structure for each sample and acquired 270 frames; 850 nm was the illumination wavelength. D) B-mode photoacoustic images with different optical scatterer concentrations and thus laser fluence values show reduced SNR with increasing TiO_2 concentration (decreased laser fluence). Scale bars represent 1 cm.

3.2.2 Testing

Low fluence laser source. To test the trained model, we printed term “UCSD” on a transparent film in black ink and placed it beneath the agarose hydrogel. The black ink is strongly absorbing and will produce photoacoustic signal. The TiO_2 optical scatters with the same concentrations as in the training section were used to test the model under different laser fluence values. We collected 270 frames, and each frame was individually used as an input in the model.

For a fair evaluation of our trained model, we need a testing test that does not share the same illumination condition as training. Such a test would quantify the extent of model’s operational scope around a set of training data. In that regard, testing was done at 0.065 and 0.016 mJ/pulse fluences to evaluate model scalability in illuminations lower than the training domain (0.95 and 0.25 mJ/pulse). This strategy minimizes the risk of overfitting the model and we evaluate the model based on actual sample features and beyond certain fluency ranges. All output frames were placed next to each other to generate the 3D volumetric data. Importantly, the trained model was totally blind to this new data set. We measured the PSNR and SSIM metrics

on each letter: U, C, S, and D. We performed t-test statistical analysis, and p values < 0.05 were considered to be significantly different.

LED-based light source. We also tested the model with the LED-based photoacoustic imaging system but without any nanoparticle gel scatterers (LED system has inherently low fluence). We again printed “UCSD” and placed it beneath a transparent agarose hydrogel. The LED was operated at 1 K Hz and 2 K Hz for 40 and 80 μJ/pulse on the sample. We used all 180 frames as the input for the model. We placed all frames after each other to create a 3D volumetric image. The ground truth data were collected by operating the LED source at 4 K Hz (160 μJ of fluence). We used 20 rounds of averaging for each frame. We separated each letter 3D map and measured PSNR and SSIM metric on each letter.

We also evaluated the model with an LED-based system and a different configuration. We placed pencil lead (0.5 mm HB, Newell Rubbermaid, Inc., IL, USA) at depths of 2.5, 7.5, 12.5, 17.5, and 22.5 mm in 2% intralipid (20%, emulsion, Sigma-Aldrich Co, MO, USA) mixed with agarose. We used intralipid to mimic biological tissue. We collected a single frame with the LED system at 1 K Hz and 2 K Hz to have 40 and 80 μJ/pulse on the surface of the sample. To measure the CNR for both input (Noisy) and output (MWCNN model) images, and were defined as the average (5 different areas) of the mean photoacoustic intensity on the pencil lead (ROI of 1 X 1 mm^2) and the background area (ROI of 3 X 3mm^2), respectively. Term is the average of all five standard deviations of background intensity.

3.2.3 *In vivo* Performance

We also evaluated our trained model in its ability to enhance the contrast agent detection in vivo. Here, the murine tissue reduces the fluence. We purchased nine nude mice (8-10 weeks) from the University of California San Diego Animal Care and Use Program (ACP). All animal experiments were performed in accordance with NIH guidelines and approved by the Institutional Animal Care and Use Committee (IACUC) at the University of California, San Diego. The mice

were anesthetized with 2.5% isofluorane in oxygen at 1.5 L/min. Methylene blue (MB) (Fisher Science Education Inc., PA, USA) was purchased and dissolved in distilled water. MB concentrations of 0.01, 0.05, 0.1, 1, and 5 mM were injected intramuscularly in a murine model (n=3). The Vevo LAZR (VisualSonic Inc.) system was used for this in vivo experiment. We monitored the injection procedure using both ultrasound and photoacoustic images. The location of injected MB was confirmed using photoacoustic spectral data. We measured the CNR for both input (Noisy) and output (MWCNN model) images. For this calculation, and were defined as tahe verage (5 different areas) of mean values of photoacoustic intensity at the injected area (ROI of 1 X 1 mm^2) and around the injected area (ROI of 3 X 3mm^2), respectively. Term is average of all five standard deviations of background intensity.

3.2.4 Multi-level Wavelet-CNN

We used a multi-level wavelet-CNN (MWCNN) model with low receptive field, low computational cost, and high adaptivity for PA imaging in multi-frequency space [141]. The model is based on a U-Net architecture and consists of a contracting sub-network followed by an expanding subnetwork. The contracting subnetwork uses discrete wavelet transform (DWT) instead of pooling operations. This substitution allows high-resolution restoration of image features through inverse wavelet transform (IWT) within the expanding subnetwork.

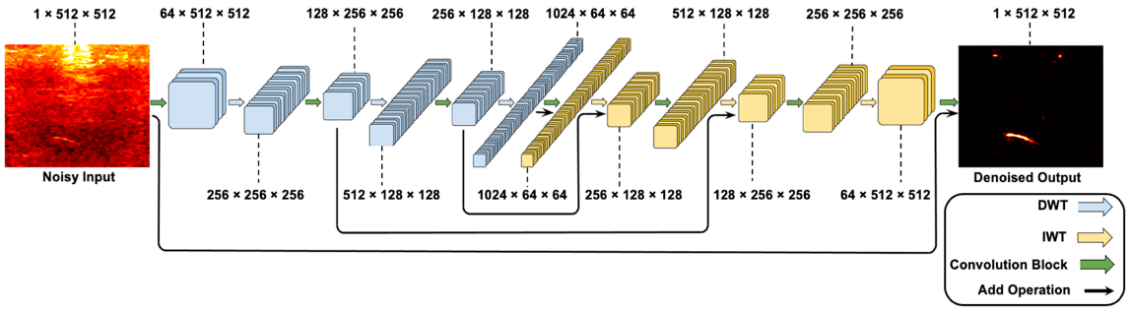

Figure 3. 2 MWCNN model architecture. Contracting subnetwork features are extracted in wavelet space. In expanding the subnetwork, features expand into the image space while preserving high resolution details. This model takes a 512 x 512 noisy image as the input and transfers that to a 512 x 512 denoised output image. Add operations directly feed the contracting feature maps to expanding feature maps to preserve image details and avoid blur effects.

The model takes a 512 x 512 noisy image as the input and transfers that to a 512 x 512 denoised output image (**Figure 2**). The model processes the image in one channel as a heatmap. The input is a 2D cross-sectional framelet from a PA imagery set. The model attempts to reduce the noise in the image while preserving the signal. This model expands the feature dimension of the input from 1 to 1024 channels and then contracts the feature maps back into 1 channel as the output. The convolution blocks may contain multiple convolutional layers. Each convolution layer is followed by a ReLU activation function.

In the contracting subnetwork of the model, the image features go through multiple convolutions with intermittent DWT blocks. Our model uses a Haar wavelet transform based on the following orthogonal filters:

(1)

The DWT blocks transform feature maps into four sub-bands. Due to the biorthogonal property of this operation, the original feature map can be accurately retrieved by an inverse Haar wavelet transform. The IWT blocks are then placed in between convolution blocks of the

expanding subnetwork. For more details on the properties this transform, readers are referred to the original work [141].

Other CNN methods mostly use U-Net based architecture utilizing pooling operating in between convolutions—the average pooling in these systems can cause information loss in the feature maps. The MWCNN architecture benefits from DWT and IWT as a safe down-sampling and up-sampling processes where the feature maps can be transmitted with no information loss throughout the model. The objective of the training process is to optimize the model parameters with the goal of minimizing the MSE loss function:

(2)

The training set is . In this equation, is the low fluence (noisy) input image, is the corresponding high energy ground truth, and is the model output.

In PA imaging, the absolute magnitude of the signal and noise is dependent on multiple factors like light illumination, acoustic detection, and the experimental setup. Training a model based on the relative magnitude of the signal and noise might limit the model to specific types of samples and settings. Here, we focus the training on the shape features of the signal rather than the magnitude because such a model can be more generic and scalable. To minimize the model's reliance on the signal magnitude, we normalize the pixel values of the input between zero and one. In this setting, the model is inclined to distinguish noise from signal based on the *shape* features. The model is trained in a supervised manner to transform low energy inputs into outputs as close as possible to the ground truth frames.

3.2.5 Photoacoustic Imaging System

Two different commercially available pre-clinical photoacoustic imaging systems were used in this study. Both systems can physically translate the transducer to generate three-

dimensional (3D) images. Model training used the Vevo LAZR (VisualSonic Inc.), which utilizes laser excitation integrated into a high frequency linear array transducer (LZ-201, Fc = 15 MHz) with optical fibers integrated to both sides of the transducer[142]. For optical excitation, this system uses a Q-switched Nd:YAG laser (4-6 ns pulse width) with a repetition rate of 20 Hz (frame rate of 6 Hz) followed by an optical parametric oscillator (tunable wavelength 680-970 nm). The laser fluence was 17.06 ± 0.82 mJ using a laser pyroelectric energy sensor (PE50BF-C, Ophir LLC, USA).

To modulate the intensity of the laser, we placed the sample in different concentrations of TiO_2 nanoparticles. These nanoparticles are well-known scatterers that decrease the fluence on the sample (when placed between the source and the sample). We measured the fluence with different concentrations of nanoparticles using same energy sensor mentioned above.

Test data used a scanner lower fluence than the laser (LED excitation; AcousticX; CYBERDYNE Inc.). This system is equipped with a 128-element linear array ultrasound transducer with a central frequency of 10 MHz and a bandwidth of 80.9% fitted with two 690 nm LED arrays. The repetition rate of these LEDs is tunable between 1, 2, 3, and 4 K Hz. The pulse width can be changed from 50 ns to 150 ns with a 5-ns step size. The LED fluence at 1 K Hz and 2 K Hz was 20 and 40 μJ/pulse, respectively.

3.2.6 Image Evaluation Metrics

Peak signal-to-noise ratio (PSNR). We used the PSNR metric to evaluate the model in terms of noise cancelation. The PSNR is described in decibel (dB) and calculated based on square differences between the model output and ground truth images as:

(3)

Where,

(4)

and are the ground truth and model output images, respectively. Term represents the maximum possible value in the given images [138].

Structural Similarity Index Measurement (SSIM). The SSIM evaluates image quality in terms of structural similarity; it is represented on a scale of 1. A higher SSIM shows better structural similarity of an output model image with the ground truth data.

(5)

Here, () and () are the mean (variance) of the ground truth and MWCNN output images, respectively; shows the covariance between these two data. and are used to stabilize the division with a weak denominator [138].

Contrast-to-noise ratio (CNR). CNR determines the image quality and is described in decibel (dB) via the following equation:

(6)

Here, and are mean of object and background noise, respectively; represents standard deviation of background intensity in the image [143].

3.3 Results

3.3.1 Low Fluence Laser Source

Laser fluence decreases when passing through a scattering media such as biological tissue. The photoacoustic signal intensity is proportional to the laser fluence, and thus the quality of acquired images will be affected. We intentionally decreased the laser fluence and improved the acquired images using MWCNN.

Figure 3A illustrates the ground truth 3D image of “UCSD” using the full laser fluence (17 mJ/pulse) from the Vevo LAZR system. **Figure 3B, C** shows the SSIM and PSNR vs laser fluence for both noisy (input) and MWCNN model (output) images. This model improved the SSIM with a factor of 1.45, 1.5, and 1.62 for laser fluence values of 0.95, 0.25, and 0.065 mJ/pulse, respectively. The PSNR was enhanced by 2.25-, 1.84-, and 1.42-fold for laser fluence values of 0.95, 0.25, and 0.065 mJ/pulse, respectively. The trained MWCNN model cannot significantly improve SSIM and PSNR ($p > 0.05$) at 0.016 mJ/pulse. **Figure 3D, E, F,** and **G** shows the noisy (input) 3D image of the UCSD object captured with laser fluence values of 0.95, 0.25, 0.065, and 0.016 mJ/pulse, respectively. The output of MWCNN for laser fluence of 0.95, 0.25, 0.065, 0.016 mJ is represented in **Figure 3H, I, J,** and **K**, respectively.

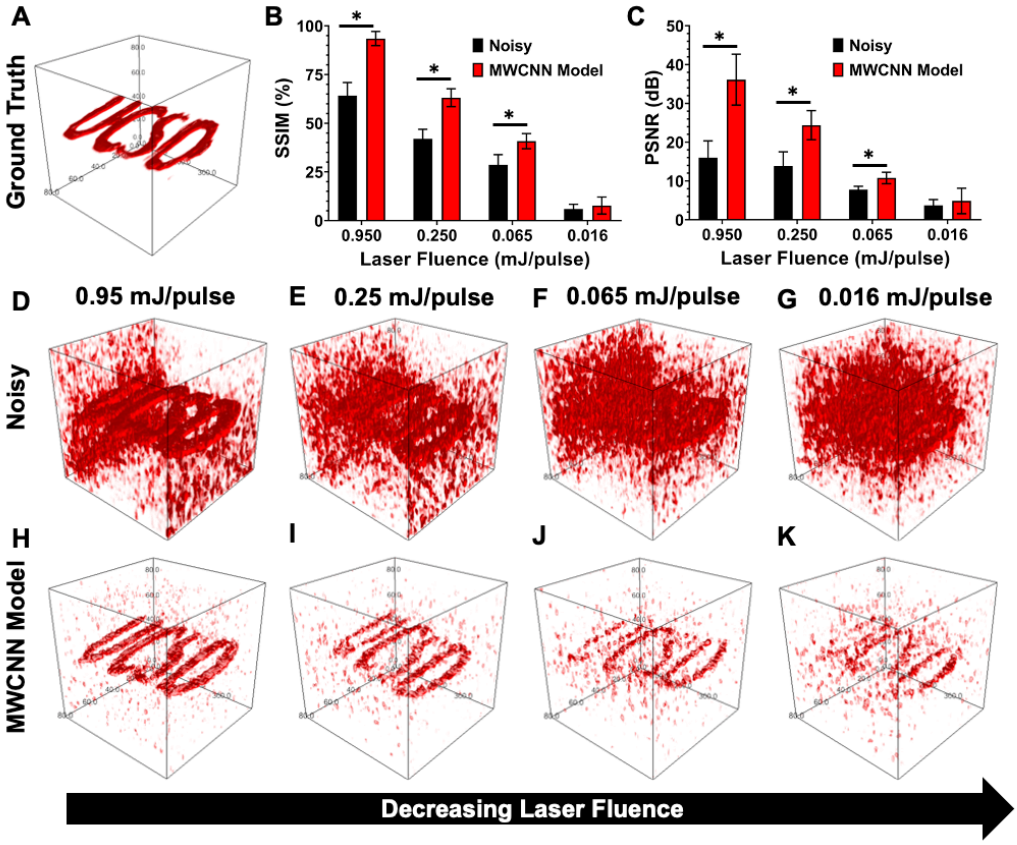

Figure 3. 3 Low fluence laser source evaluation. A) Ground truth 3D image of UCSD sample with full laser fluence of 17 mJ/pulse. We used this image as a reference for measuring image quality metrics. B) SSIM of noisy (input) and MWCNN data vs laser fluence. The results show that the SSIM is significantly improved by 1.45, 1.5, and 1.62 at laser fluence values of 0.95, 0.25, 0.065 mJ/pulse, respectively. The model failed to improve the structural similarity at fluence of 0.016 mJ/pulse. C) PSNR of both noisy and MWCNN data vs laser fluence—the PNSR is significantly improved with a factor of 2.25, 1.84, and 1.42 for 0.95, 0.25, 0.065 mJ/pulse, respectively. However, the MWCNN cannot significantly improve the image quality with a laser fluence of 0.016 mJ/pulse. In both B and C, the error bars represent the standard deviation of SSIM and PSNR among the four letters in "UCSD". * indicates $p < 0.05$. D, E, F, and G) Noisy (input) images with 0.95, 0.25, 0.065, and 0.016 mJ/pulse laser fluence, respectively. H, I, J, and K) MWCNN model (output) images with 0.95, 0.25, 0.065, and 0.016 mJ/pulse laser fluence, respectively.

3.3.2 LED Source

We next examined our MWCNN model with LEDs as a low fluence source. **Figure 4A** shows the ground truth 3D photoacoustic image using the LED-based photoacoustic imaging system. After collecting all the noisy data with 40 and 80 μJ/pulse as LED fluence on the sample, we noted an improvement in SSIM by a factor of 2.2 and 2.5 for 40 and 80 μJ/pulse, respectively

(Figure 4B). **Figure 4C** demonstrates a 2.1- and 1.9-fold increase in PNSR on MWCNN model (output) versus noisy (input) for both 40 and 80 µJ/pulse. **Figure 4D** and **F** shows the noisy 3D photoacoustic image using the LED-based imaging system with fluence values of 80 and 40 µJ µJ/pulse. **Figure 4E** and **G** are MWCNN 3D results with 80 and 40 µJ µJ/pulse, respectively.

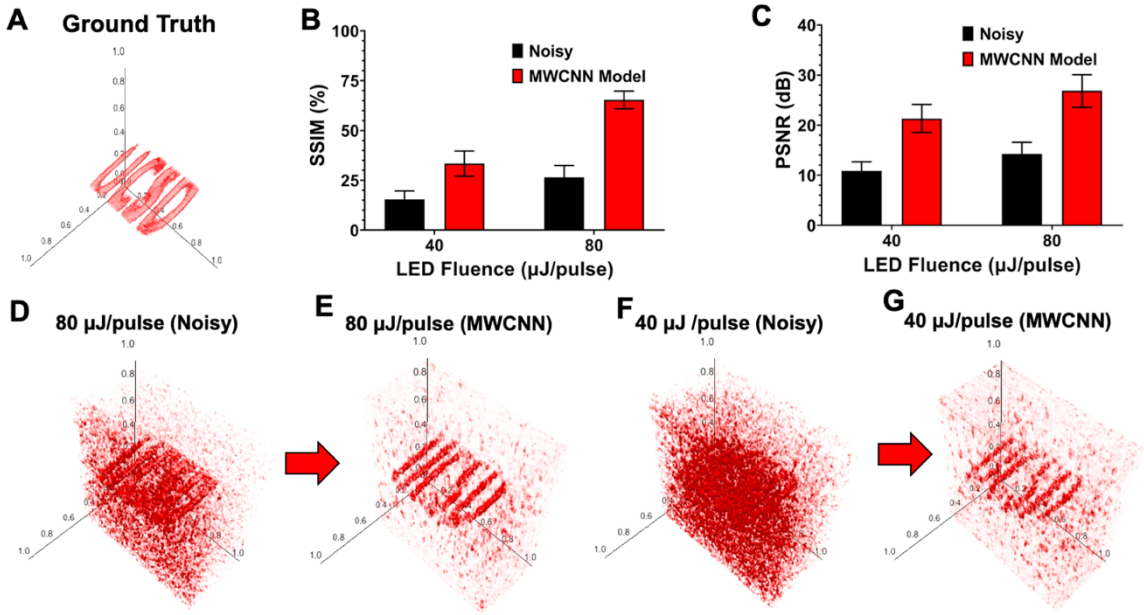

Figure 3. 4 LED light source evaluation. A) Ground truth 3D image of UCSD word using the LED-based photoacoustic imaging system. The ground truth data were collected by operating the LED source at 4 K Hz with a fluence of 160 µJ and 20 rounds of averaging for each frame. B) SSIM results of both noisy (input) and MWCNN model (output) in two different LED fluences of 40 and 80 µJ/pulse. An improvement of 2.2- and 2.5-fold is observed for 40 and 80 µJ/pulse, respectively. C) PSNR of noisy (input) and MWCNN model (output) at 40 and 80 µJ/pulse. MWCNN improved the PNSR by 2.1 and 1.9 for 40 and 80 µJ/pulse, respectively. In both B and C, the error bars represent the standard deviation of SSIM and PSNR among the four letters in “UCSD”. D) The 3D noisy (input) photoacoustic image used 80 µJ/pulse. E) 3D MWCNN mode (output) photoacoustic image using 40 µJ/pulse. F) 3D Noisy (input) photoacoustic image with 40 µJ/pulse. G) 3D MWCNN mode (output) photoacoustic image with 40 µJ/pulse.

We also evaluated the performance of the MWCNN model in depth phantoms using the LED system and scattering media. **Figure 5A** and **B** shows noisy images for LED fluence at 40 and 80 µJ/pulse. We observed a significant CNR improvement both qualitatively (**Figure 5C** and **D**) and quantitatively (**Figure 5E**). We measured an average of 4.3- and 4.1-fold enhancement in MWCNN model versus noisy images at different depths for 40 and 80 µJ/pulse. **Figure 5E** shows

that the MWCNN also enhanced the linearity of CNR vs depth from R^2 =0.84 and 0.85 to R^2 =0.97 and 0.95 for both LED fluence values.

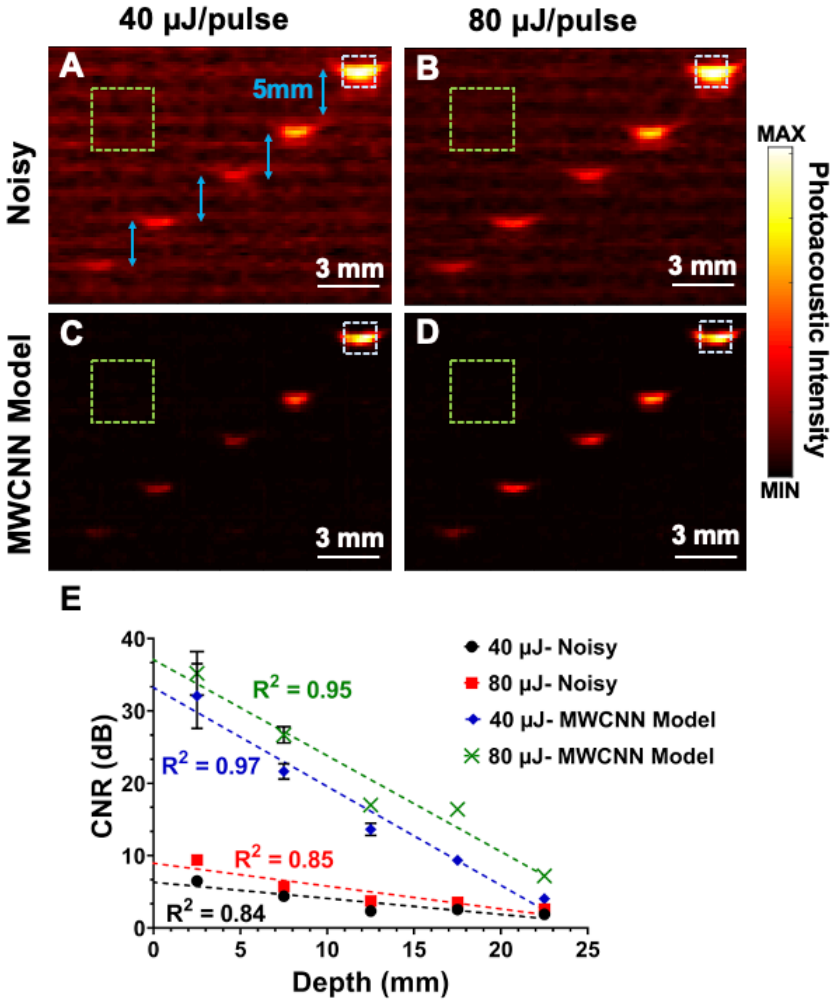

Figure 3. 5 Penetration depth evaluation using an LED. A) B-mode noisy (input) photoacoustic image using LED at a fluence of 40 µJ/pulse. Pencil leads were placed at 2.5, 7.5, 12.5, 17.5, and 22.5 mm in 2% intralipid. B) B-mode noisy (input) photoacoustic images at a fluence of 80 µJ/pulse with similar experimental setup as described in A. C, D) B-mode MWCNN model (output) photoacoustic image for 40 and 80 µJ/pulse. E) CNR versus depth for 40 and 80 µJ/pulse in both noisy and MWCNN model. Dotted green and white rectangles represent the ROI used to measure mean values and standard deviations of background (ROI size:3 x 3 mm^2) and object (ROI size:1 x 1 mm^2). We observed an average of 4.3- and 4.1-fold enhancement in the MWCNN model versus noisy data at different depths for both LED values.

3.3.3 *In vivo* Performance

Image enhancement methods become more valid when validated *in vivo*. The detection of exogenous contrast agents using photoacoustic imaging technique can be a challenge due to

low fluence due to scattering by biological tissue. Here, we injected different concentrations of MB intramuscularly in mice (**Figure 6A**) and analyzed the acquired images using the MWCNN model and compared the CNR with and without the model. **Figure 6B** represents the CNR for both noisy (input) and MWCNN model (output) for all 5 different concentrations. We observed a significant improvement between noisy and model output. There was an improvement of 1.55, 1.76, 1.62, and 1.48 in CNR for 0.05, 0.1, 1.0, and 5.0 mM, respectively. The MWCNN failed to improve the CNR for 0.01 mM. The signal intensity of 0.01 mM MB was so low that the model considered it to be noise.

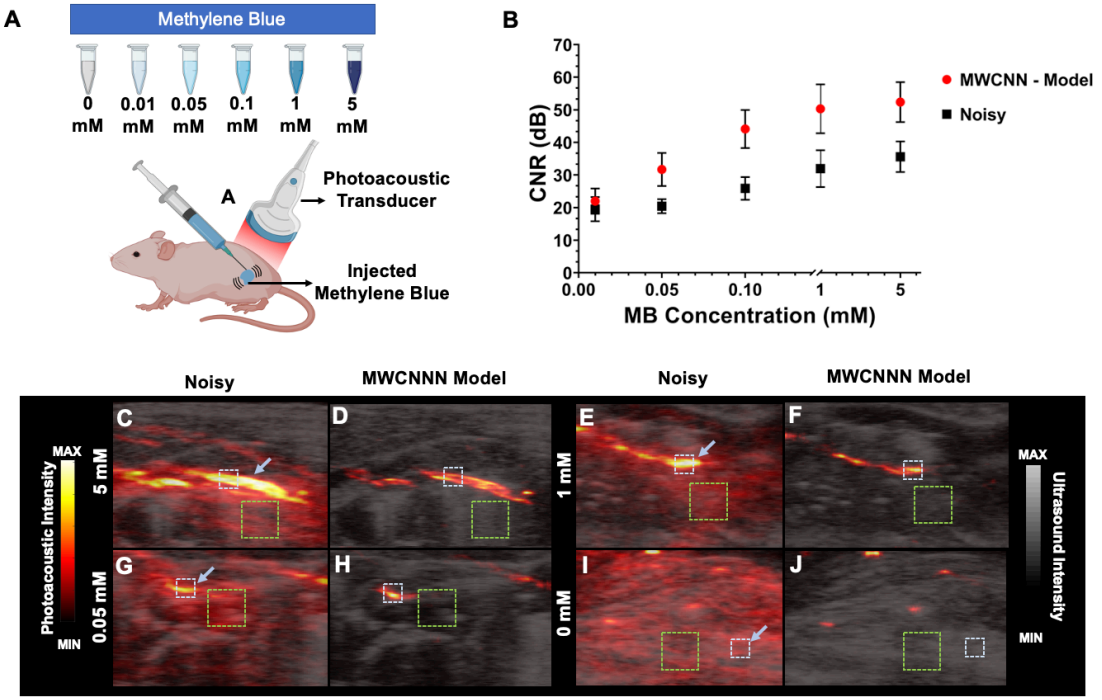

Figure 3. 6 In vivo evaluation of MWCNN model. A) Experimental schematic for in vivo evaluation of MWCNN model. Five different concentrations of MB (0.01, 0.05, 0.1, 1, and 5 mM) were injected intramuscularly. B) CNR versus injected MB concentrations for both noisy and MWCNN model. We noted 1.55-, 1.76-, 1.62-, and 1.48-fold improvement of CNR for 0.05, 0.1, 1.0, and 5.0 mM, respectively. Error bars represent the CNR among three different animals. For CNR calculation, and were defined as the average of five different areas of mean values of photoacoustic intensity at the injected area (ROI of 1 X 1 mm^2) and around the injected area (ROI of 3 X 3mm^2), respectively. Term is the average of all five standard deviations of background intensity. Panels C, E, G, and I) are B-mode noisy photoacoustic images for 5.0, 1.0, 0.05, 0 mM, respectively. These images are overlaid on ultrasound data. D, F, H, and J) B-mode MWCNN photoacoustic images for 5, 1, 0.05, 0 mM, respectively. Dotted green and white rectangles represent the used ROIs for background and object. Blue arrows show the MB injection area.

3.4 Discussion and Conclusions

CNNs have been widely utilized in computer vision, image processing, and medical imaging. However, deep learning has utility beyond image segmentation, object detection, and object tracking. Here, we proposed a deep learning model that can learn to restore PA images at different low fluence configurations and samples. To ensure the scalability of our solution, we built our model based on a limited training process and evaluated it with different illumination sources on other sample types and materials.

We observed quantitative and qualitative enhancement results. The proposed model was completely blind to our test data. We could achieve up to 1.62- and 2.2-fold improvement in SSIM (**Figure 3B** and **4B**) for low fluence laser source and LED, respectively. The model improved the PSNR by a factor of up to 2.25 and 2.1 for low fluence laser and LED, respectively. A higher number of training datasets can lead to improvement factors (SSIM, PSNR) that will be significantly higher. PNSR and SSIM calculations require a ground truth image. However, having this data is not feasible in most cases. To show that our proposed method can enhance other image quality metrics, we used the CNR to evaluate the penetration depth and in vivo data. The ground truth is not required with this metric, and the CNR will be measured using just a single frame. We showed that the MWCNN can improve the contrast as well (**Figure 5E, 6B**). Finally, we showed that this contrast improvement has value in vivo with contrast improved up to 1.76-fold.

Like other deep learning methods, our solution gains most of its computational cost at the training stage. The training cost can scale up as the training set grows. At runtime, the model can process each frame at 0.8 seconds, which is relatively faster than classical methods like BM3D (3.33 seconds). It is also similar to DL methods like low-dose CT CNN (2.05 seconds) [124].

Our training included a small set of frames from a laser source within a specific range of illumination fluencies. Such a small training set can facilitate a model that trains fast for practical solutions. On the other hand, normalizing the training data made the model independent of signal

magnitude in the input. This independence guided the model to generically learn important spatial features of samples in PA images beyond the settings and configurations. Future work may also evaluate any improvements achieved via increasing numbers of training sets.

The tests introduced lower fluencies of illumination from different sources. The observations suggest that the model learned features to distinguish signal from noise regardless of the input image quality. Comparable results between laser and LED based inputs also suggests the utility of our solution among various imaging systems.

The next step of this work will focus on training and testing processes on *in vivo* samples including actual blood vessels and other exogenous contrast agents. We will also expand the model from a 2D framework to 3D data. In that regard, we can train models based on a stack of PA images to potentially improve the consistency of results along the axis and reduce the noise in 3D results as well as cross-sectional images. In such setting, we need to upgrade the structure of samples in our training data to better represent the complex 3D features. Also, increasing the dimensions of the model will inherently increase the amount of training data required to develop the models but may facilitate even more advanced in vivo imaging.

Chapter 3, in full, is a reprint of the material as it appears in *Biomedical Optics Express* 11, no. 6 (2020): 3360-3373.. Ali Hariri, Kamran Alipour, Yash Mantri, Jurgen P. Schulze, and Jesse V. Jokerst. The dissertation author was the primary investigator and author of this paper.

Chapter 4 Molecular imaging of oxidative stress using an LED-based photoacoustic imaging system

LED-based photoacoustic imaging has practical value in that it is affordable and rugged; however, this technology has largely been confined to anatomic imaging with limited applications into functional or molecular imaging. Here, we report molecular imaging reactive oxygen and nitrogen species (RONS) with a near-infrared (NIR) absorbing small molecule (CyBA) and LED-based photoacoustic imaging equipment. CyBA produces increasing photoacoustic signal in response to peroxynitrite ($ONOO^-$) and hydrogen peroxide (H_2O_2) with photoacoustic signal increases of 3.54 and 4.23-fold at 50 μM of RONS at 700 nm, respectively. CyBA is insensitive to OCl^-, $^{\bullet}NO$, NO_2^-, NO_3^-, tBuOOH, O_2^-, $C_4H_9O^{\bullet}$, HNO, and $^{\bullet}OH$, but can detect $ONOO^-$ in whole blood and plasma. CyBA was then used to detect endogenous RONS in macrophage RAW 246.7 cells as well as a rodent model; these results were confirmed with fluorescence microscopy. Importantly, CyB suffers photobleaching under a Nd:YAG laser but the signal decrease is <2% with the low-power LED-based photoacoustic system and the same radiant exposure time. To the best of our knowledge, this is the first report to describe molecular imaging with an LED-based photoacoustic scanner. This study not only reveals the sensitive photoacoustic detection of RONS but also highlights the utility of LED-based photoacoustic imaging.

4.1 Introduction

Reactive oxygen and nitrogen species (RONS) modulate important functions in living systems. Endogenous RONS facilitate signal transduction [144], smooth muscle relaxation, and blood pressure modulation [145]. Dysregulated RONS can lead to diseases such as cancer [146-148], and RONS detection is useful in the diagnosis and treatment of infections and disease. There are various fluorescent contrast agent to detect and quantify RONS [145, 149, 150], but their *in vivo* applications are limited due to the low spatial resolution and limited penetration depth of fluorescence [151].

Photoacoustic imaging (PAI) is an alternative imaging approach and combines optical and ultrasound imaging features [7, 40, 106] and offers better penetration with less scatter than fluorescent imaging. Smart activatable photoacoustic probes can produce photoacoustic signal in the presence of specific molecules or events such as RONS [47, 152]. Pu and workers have described several RONS-sensitive molecules with activatable photoacoustic signal [151, 153-156] including Cheng et al. who reported CyBA for detection of RONS using fluorescence imaging[157].

Regardless of the imaging target, PAI usually uses high energy lasers. Although these lasers offer tunable excitation wavelengths and high power, they are also large and cumbersome and require regular maintenance. In addition, many contrast media are not stable at such high fluences. In one example, the photoacoustic signal of gold nanorods decreased by ~30% after exposure to 120 μs of 9 mJ/cm^2 fluence)[151] due to a change in the nanorod morphology [158]. In another example, Onoe et al. developed a symmetrical NIR cyanine dye for cancer imaging utilizing fluorescence and photoacoustic imaging [159], but this probe degraded under high-energy laser pulses during imaging [160].

Although a more stable probe design is an obvious solution, one exciting alternative is pulse laser diodes (PLDs) [58] or light emitting diodes (LEDs) [60, 61]. The LED fluence is on the order of μJ and 1000-fold lower than high energy lasers [107]. We previously described a commercially available LED-based photoacoustic imaging system and validated it with phantoms and cellular

imaging [107]. Here, we report the use of a near-infrared (NIR) small molecular probe for photoacoustic imaging that is sensitive to various types of RONS[157]. We first evaluated the probe with both a laser and a LED. The absorption and photoacoustic response of this probe were examined with different RONS in different sample matrices such as PBS/DMSO, plasma, and fresh blood. We then used the probe to measure the endogenous RONS produced stimulated macrophages with the LED-based photoacoustic imaging system along with *in vivo* imaging of an inflammation model.

4.2 Methods and Materials

4.2.1 Chemicals

Aqueous PBS stock solution and hydrogen peroxide (H_2O_2) (30 wt%, Cat. #H325) were purchased from Thermo Scientific (Waltham, MA, USA). We purged PBS with N_2 for 1 hour before any dilution and measurement. Peroxynitrite ($ONOO^-$) was purchased from EMD Millipore Co. (Cat. #516620, MA, USA). Superoxide (O_2^-), Hypochlorite (OCl^-), Nitric oxide ($^{\cdot}NO$), Tert-butyl hydrogen peroxide (tBuOOH), Tert-butoxy radical ($C_4H_9O^{\cdot}$), Nitrite (NO_2^-), Nitrate (NO_3^-), and Nitroxyl (HNO) were prepared by direct dilution of potassium superoxide (Cat. #278904), sodium hypochlorite (Cat. #239305),Tert-butyl hydroperoxide (Cat. #416665), Tert-butyl peroxide (Cat. #168521), Sodium nitrite (Cat. #237213), Sodium nitrate (Cat. #221341), and angeli's salt (Cat. #176695). These were purchased from Sigma-Aldrich (Atlanta, GA, USA). Hydroxyl radicals ($^{\cdot}OH$) were generated via the Fenton reaction between H_2O_2 and iron (II) perchlorate hydrate ($Fe(ClO_4)_2$) (Cat. #334081, Sigma-Aldrich, Atlanta, GA, USA). The 2′,7′-dichlorofluorescin diacetate (DCF-DA) (Cat. #D6883), N-acetylcysteine (NAC), Lipopolysaccharides (LPS) from *Escherichia coli,* and Zymosan A from Saccharomyces Cerevisiae were purchased from Sigma-Aldrich (Atlanta, GA, USA). A stock solution of the new synthesized dye was prepared by dissolving in dimethyl sulphoxide (DMSO) (Thermo Scientific, Waltham, MA, USA). Normal pooled human plasma was purchased from

Innovative Research Inc. (Novi, MI, USA). Blood was obtained from healthy donors in 3.2% sodium citrate vacutainers (BD life Science) and informed consent was obtained from all subjects. All methods were performed in accordance with the relevant guidelines and regulations. All experimental protocols were approved by University of California San Diego.

4.2.2 Probe Synthesis and Characterization

Cheng et al first developed and reported the application of CyBA for detection of RONS using fluorescence imaging[157]. The synthesis was adopted from their study [157] and used a mixture of compound CyOH (38 mg, 0.1 mmol) and Cs_2CO_3 (130 mg, 0.40 mmol) in anhydrous CH_2Cl_2 (10 mL) in a round-bottom flask was stirred for 20 min at room temperature. The 4-bromomethylphenylboronic acid pinacol ester (60 mg, 0.20 mmol) was then added and the reaction was further stirred overnight at room temperature under N_2 atmosphere. The reaction mixture was then washed with water (30 mL) and extracted with CH_2Cl_2 (3 × 30 mL). The organic layer was dried with anhydrous Na_2SO_4 and concentrated under reduced vacuum. The pure product CyBA was obtained as a blue solid (45 mg, 75%) after purification by flash column chromatography (CH_2Cl_2/MeOH = 10:1). ^{1}H NMR (300 MHz, CD_3OD): δ = 8.70 (d, *J* = 15.0 Hz, 1H), 7.80 (d, *J* = 8.1 Hz, 2H), 7.68 (d, *J* = 7.2 Hz, 1H), 7.55 (m, 2H), 7.50 (d, *J* = 8.1 Hz, 2H), 7.45 (m, 2H), 7.34 (s, 1H), 7.02 (m, 2H), 6.49 (d, *J* = 15.0 Hz, 1H), 5.29 (s, 2H), 3.85 (s, 3H), 2.76 (t, *J* = 6.0 Hz, 2H), 2.71 (t, *J* = 6.0 Hz, 2H), 1.92 (m, 2H), 1.81 (s, 6H), 1.34 (s, 12H). MS of compound CyBA: calculated for $C_{39}H_{43}BNO_4$, $[M^+]$: 600.39; observed MS: m/z 600.40.

4.2.3 Instrumentation

We used a SpectraMax M5 spectrophotometer for absorbance measurements. An EVOS fluorescence microscope with FITC filter sets (Life Technologies Inc., Ca, USA) was utilized for brightfield and fluorescence microscopy imaging. Photoacoustic images were acquired using an

LED-based photoacoustic imaging system from CYBERDYNE Inc. (formerly Prexion)[107]. The system is equipped with a 128-element linear array ultrasound transducer with a central frequency of 10 MHz and a bandwidth of 80.9% fitted with two 690 nm LED arrays. The repetition rate of these LEDs is tunable between 1, 2, 3, and 4 K Hz. The pulse width can be changed from 50 ns to 150 ns with a 5-ns step size. The transducer can be scanned to generate three-dimensional (3D) data using maximum intensity projection (MIP) algorithm.

4.2.4 Tissue Culture

RAW 246.7 cells (ATCC TIB-71) were cultured using Dulbecco's Modified Eagle's Medium (DMEM, Gibco) supplemented with 10% fetal bovine serum (Sigma) and 1% antibiotic-antimycotic (Thermo Fisher Scientific). Cells were incubated at 37^{o}C and media was replaced every 2-3 days. Cells were cultured until 90% confluence and passaged mechanically through scraping.

4.2.5 Probe Stability

A Nd:YAG laser with an optical parametric oscillator (Vevo 2100 photoacoustic scanner, Visualsonics) and a LED (LED-based scanner, CYBERDYNE Inc.) at 690 nm were used to evaluate the stability of the new probe. Here, 15 µL of a 0.1 mM solution were placed in polyethylene tubing (OD: 1.27 mm, ID: 0.85 mm) inside the chicken breast to scatter the incident light (at depth of 1cm) and imaged with the laser or LED to study the stability of the probe. Laser illumination used a pulse width and frame rate of 5 ns and 6 Hz, respectively. A laser pyroelectric energy sensor (PE50BF-C, Ophir LLC, USA) measured the laser fluence. LED illumination used a LED-based scanner (pulse width: 70 ns, frame rate: 6 Hz) with a photodiode sensor (S120C, Thorlabs Inc., USA) to measure the LED fluence. The effective illumination for both is 16 µs (effective illumination = number of laser or LED pulses x the pulse width).

4.2.6 Absorption Response of CyBA Toward RONS

We first studied the absorption response of the probe toward RONS. We used various concentrations for $ONOO^-$ (12.5, 25, 50, 75, 100, and 200 μM) to evaluate changes in the probe's absorption spectrum (400 nm – 800 nm) in the presence of RONS. Next, we tested the effect of OCl^-, $^{\cdot}NO$, NO_2^-, NO_3^-, tBuOOH, O_2^-, $C_4H_9O^{\cdot}$, HNO, $^{\cdot}OH$, H_2O_2, and $ONOO^-$ by monitoring the change in 700 nm absorption using a 80 μM solution of the probe and 50 μM RONS. Three replicates were used.

4.2.7 Photoacoustic Response of CyBA in the Presence of RONS

CyBA and CyOH (activated form of the probe) were studied at 20, 40, 80, 160, 320, and 640 μM. We also examined the photoacoustic response of CyBA to 50 μM of OCl^-, $^{\cdot}NO$, NO_2^-, NO_3^-, tBuOOH, O_2^-, $C_4H_9O^{\cdot}$, HNO, $^{\cdot}OH$, H_2O_2, and $ONOO^-$. Various concentrations of $ONOO^-$ and H_2O_2 to measure the sensitivity of the probe: 12.5, 25, 37, 50, 75, 100, and 200 μM $ONOO^-$; 31, 62, 125, 250, 2500, 5000 μM, and 50 mM H_2O_2. All samples were placed inside Teflon light wall tubes and scanned with the transducer (the scan size is 10 mm) to generate three-dimensional (3D) data using maximum intensity projection (MIP) algorithm.

4.2.8 Photoacoustic Response of the Probe Towards $ONOO^-$ in Pooled Human Plasma and Blood

We extended the work with $ONOO^-$ to normal pooled human plasma and whole human blood. First, we evaluated the absorption response of 125 μM probe in the presence of 25, 50, 125, 185, 250, 375, and 500 μM of $ONOO^-$ in normal human plasma. Next, we used LED-based photoacoustic system to study the response of the probe towards $ONOO^-$ at 25, 37.5, 50, 75, and 100 μM in normal pooled human plasma and blood. Finally, we calculated a detection limit of $ONOO^-$ in plasma and blood.

4.2.9 *In vitro* Fluorescence Imaging of RONS

RAW 246.7 cells were plated into 6-well plates (50,000 cells/well) and incubated overnight. Cells were washed once with PBS, and 2 mL of media was added; 20 µL of LBS in PBS was added to the respective groups (final concentration: 1 µg/mL), and the plates were incubated for 4 hours. Then, 20 µL of NAC in PBS was added to the respective groups (final concentration: 0.1, 1, or 10 mM) and incubated for 1 hour. Finally, 20 µL of DCF-DA in DMSO was added to all groups (final concentration: 20 µM) and incubated for 20 minutes. Cells were imaged with a fluorescence microscope (EVOS) using a GFP filter.

4.2.10 *In vitro* Photoacoustic Imaging of RONS

RAW 246.7 cells were plated into 6-well plates (1 million cells/well) and incubated overnight. Cells were washed once with PBS and 1 mL of media was added. 10 µL of LPS was added to the respective groups (final conc. 10 µg/mL) and incubated for 4 hours. Then, 10 µL of NAC was added to the respective groups (final concentration: 0.1 or 10 mM) and incubated for 1 hour. Next, 400 µL of CyBA was added to the respective groups (final concentration: 125 µM) and incubated for 30 minutes. Cells were mechanically detached, centrifuged at 1000g for 5 minutes, and the supernatant was removed. All cells were resuspended in 50 µL PBS and imaged at 690 nm using LED scanner. As an additional control, LPS and CyBA were mixed without any cells and imaged.

4.2.11 *In vivo* Photoacoustic Imaging Evaluation of CyBA

All animal experiments were performed in accordance with NIH guidelines and approved by the Institutional Animal Care and Use Committee (IACUC) at the University of California, San Diego. We utilized CyBA for the *in vivo* photoacoustic imaging of RONS. Zymosan was applied to induce the acute edema in a murine model. Zymosan (20 mg/ml) was injected intramuscularly into the right biceps femoris muscle of the upper hind limb (n=3). After 20 minutes incubation,

CyBA (160 μM in saline) was injected at same location. We monitored the photoacoustic intensity (690 nm as a wavelength) of the probe at the injection area in 0, 10, 20, 30, 45, 60, 90 minutes after injection. We also injected only Zymosan and only CyBA at the same location and monitored the photoacoustic intensity as a control.

4.2.12 Statistical Analysis

All photoacoustic data were analyzed with ImageJ (Bethesda, MD, USA)[161]. All raw images were converted to 8-bit images, and then the mean value and standard deviation of the photoacoustic intensity for ten regions of interest (ROI) per tube were calculated. The error bars represent the standard deviation; P values <0.05 were considered to be significantly different.

4.3 Results

CyBA is designed by conjugating a boronic acid-based self-immolative group to CyOH. CyBA is initially in a "caged" state with diminished electron-donating ability of the oxygen atom. Upon treatment with H_2O_2 or $ONOO^-$, CyBA undergoes rapid oxidative cleavage of the borate ester moiety, followed by 1,6-elimination, eventually leading to free CyOH dye ("uncaged" state). The CyOH product has enhanced electron-donating ability from the oxygen atom, which makes its characteristic maximum absorption change in relative to CyBA. Thus, the probe enables photocoustic imaging of RONS (**Figure 1**). We used mass spectrometry to show the decomposition of probe under high concentrations of RONS (peroxynitrite) and evaluation of CyBA/CyOH composition stability under our imaging conditions. Mass spectrometry data confirmed the stability of CyBA under LED illumination and confirmed that the reaction product of CyBA in presence of RONS (peroxynitrite) is indeed CyOH (**Figure S1**).

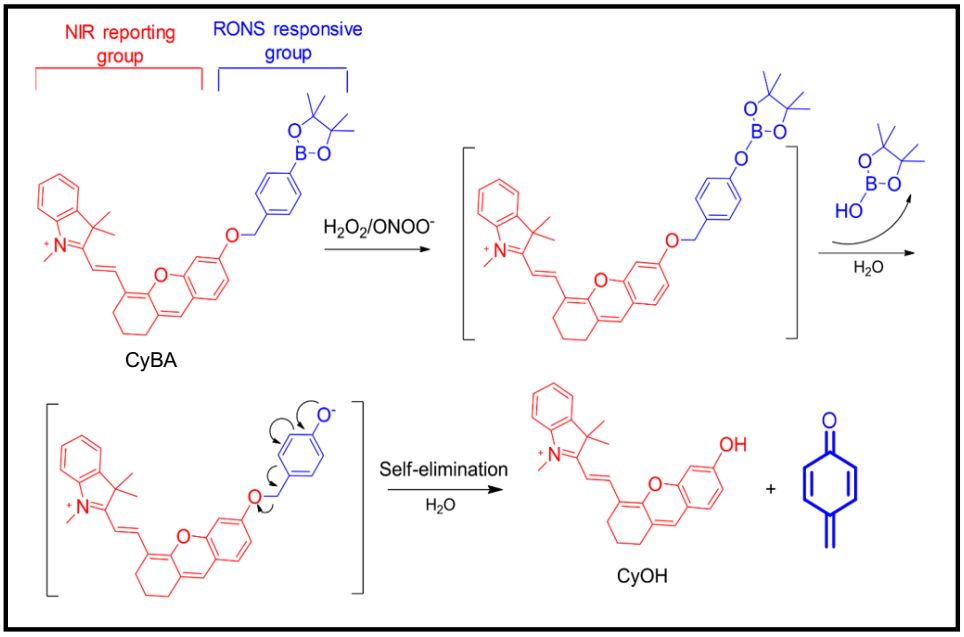

Figure 4. 1 Design and mechanism of the probe (CyBA) for RONS imaging. The RONS species liberates the boronic acid group leading to increased absorbance of the cyanine core leading to increased photoacoustic signal. Adapted from Cheng et al. [157]

4.3.1 Probe Stability

The probe has a broad absorption peak at 700 nm that increases when activated by the RONS, but we used 690 nm excitation because that equipment was available in our lab. **Figure 2A** shows the spectral profile of the LED used in the photoacoustic imaging system. It has a peak at 690 nm (range: 625-725 nm); the intensity at 700 nm is ~65% of the maximum. The laser and LED intensity at 690 nm is 12.65 ± 0.65 mJ/cm^2 and 5.5 µJ/cm^2, respectively, i.e., the laser intensity is ~2000-fold higher than the LED.

Next, we studied the photoacoustic signal of the probe with Nd:YAG laser and LED in the absence of RONS. **Figure 2B** shows that the photoacoustic signal degraded 2.6-fold after 16 µs of effective time laser illumination (laser: 3150 pulses (at 20 Hz) x 5 ns pulse width = 16 µs; LED: 240 pulses (at 4000 Hz) x 70 ns = 16 µs). The LED system shows <2% signal loss. Thus, we used the LED-based photoacoustic imaging system to evaluate the probe in all following experiments.

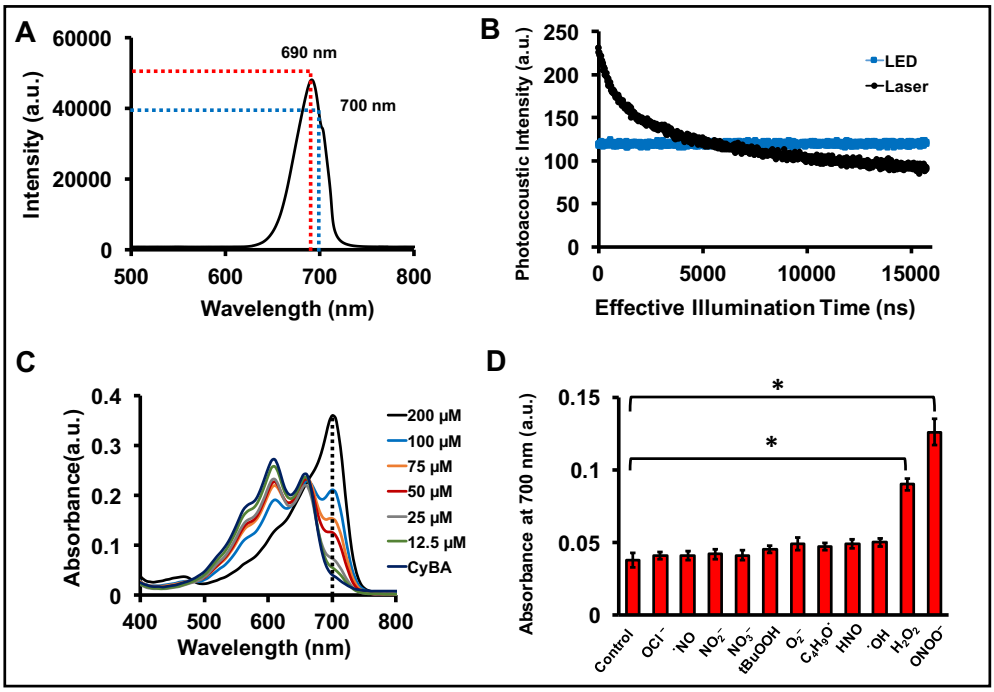

Figure 4. 2 Absorption response of new probe toward RONS. A) Spectral profile of the LED used for photoacoustic imaging. The spectrum has a peak at 690 nm and includes 700 nm. B) Photoacoustic intensity of the probe under laser and LED illumination. The photoacoustic intensity decreases 2.6-fold under laser source but <2% with the LED. Therefore, the probe is stable when used with a LED-based photoacoustic imaging system. C) The absorption spectra of the dye (80 μM) after addition of $ONOO^-$ 12.5, 25, 50, 75, 100, and 200 μM. The dye has two absorption peaks around 660 and 610 nm. However, in the presence of RONS, the 700 nm peak appears and other peaks vanish. D) Absorption of CyBA in the presence of 50 μM OCl^-, $^{\cdot}NO$, NO_2^-, NO_3, tBuOOH, O_2^-, $C_4H_9O^{\cdot}$, HNO, $^{\cdot}OH$, H_2O_2, and $ONOO^-$. The control is PBS, and the error bars represent the standard deviation of three replicate measurements. * indicates p-value < 0.05.

4.3.2 Absorption Response of the Probe Toward RONS

Next, we studied the change in the probe absorption in the presence of RONS. **Figure 2C** shows the absorption spectra of the dye (80 μM) with and without $ONOO^-$. The probe has two absorption peaks at 610 and 660 nm. The probe exhibited a new absorption peak at 700 nm upon addition of 12.5, 25, 50, 75, 100, and 200 μM $ONOO^-$ (the peaks at 610 and 660 nm decreased). Only the 700 nm peak is seen at 200 μM $ONOO^-$. **Figure 2D** shows the absorption response of the probe in the presence of OCl^-, $^{\cdot}NO$, NO_2^-, NO_3^-, tBuOOH, O_2^-, $C_4H_9O^{\cdot}$, HNO, $^{\cdot}OH$, H_2O_2, and $ONOO^-$ at 700 nm using 80 μM dye and 50 μM RONS. The absorption increased 2.38 and 3.31-fold in the presence of $ONOO^-$ and H_2O_2, respectively (p-value < 0.05).

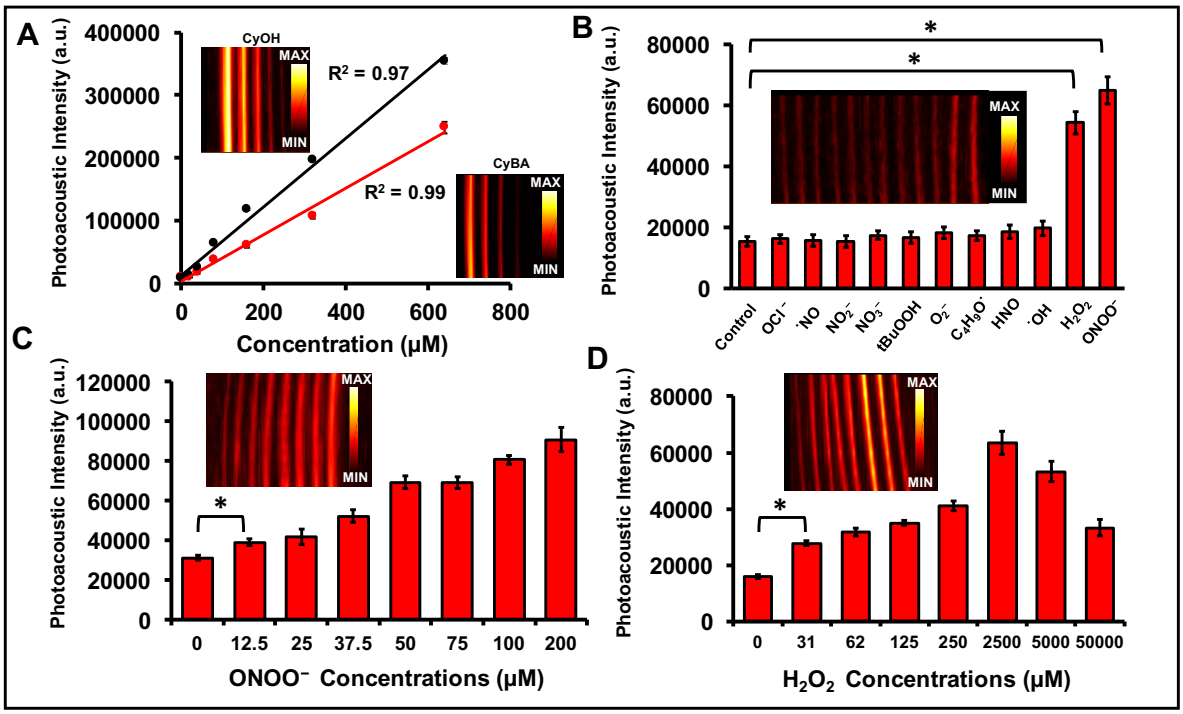

Figure 4. 3 Photoacoustic response of the probe in presence of RONS. A) Photoacoustic intensity as function of different probe concentrations. Linear correlation is observed between photoacoustic intensity and new probe concentration when imaged with the LED system. B) Photoacoustic signal of 80 μM probe in the presence of 50 μM of OCl^-, $^{\cdot}NO$, NO_2^-, NO_3^-, tBuOOH, O_2^-, $C_4H_9O^{\cdot}$, HNO, $^{\cdot}OH$, H_2O_2, and $ONOO^-$. The inset shows the MIP photoacoustic image of all the samples. The control is PBS. Dose response curve of probe to $ONOO^-$ (C) and H_2O_2 (D); insets are the MIP images. Error bars represent multiple ROIs per tube. * indicates p-value < 0.05.

4.3.3 Photoacoustic Response of the Probe in the Presence of RONS

Figure 3A shows the photoacoustic intensity as function of CyBA and CyOH concentration. The insets show the photoacoustic MIP images corresponding to CyBA and CyOH. A linear correlation was observed between the photoacoustic intensity and both CyBA (R^2 = 0.99) and CyOH (0.97) concentrations. We used 80 μM to examine the photoacoustic response to OCl^-, $^{\cdot}NO$, NO_2^-, NO_3^-, tBuOOH, O_2^-, $C_4H_9O^{\cdot}$, HNO, $^{\cdot}OH$, H_2O_2, and $ONOO^-$. This concentration was used because it has relatively low signal in the absence of RONS. **Figure 3B** shows that the probe is insensitive to OCl^-, $^{\cdot}NO$, NO_2^-, NO_3^-, tBuOOH, O_2^-, $C_4H_9O^{\cdot}$, HNO, and $^{\cdot}OH$, but the signal increased 3.54 and 4.23-fold with 50 μM H_2O_2 and $ONOO^-$, respectively. **Figures 3 C, D** detail the signal as a function of $ONOO^-$ and H_2O_2 concentrations. Higher concentrations lead to

more absorption and thus more photoacoustic signal with a detection limit of 12.5 μM $ONOO^-$ (p-value < 0.05). Similarly, the H_2O_2 sensitivity is 31 μM.

4.3.4 Utility of the Probe in Pooled Human Plasma and Blood

Figure 4A shows a linear correlation (R^2 = 0.98) between absorbance at 700 nm and $ONOO^-$ concentrations in pooled human plasma. **Figure 4B** shows the photoacoustic response of the probe in the presence of $ONOO^-$ in pooled human plasma and fresh whole blood. The detection limits of $ONOO^-$ in plasma and blood were 37.5 and 50 μM, respectively (p-value < 0.05). The detection limit is higher in blood because hemoglobin and deoxyhemoglobin increase the background signal.

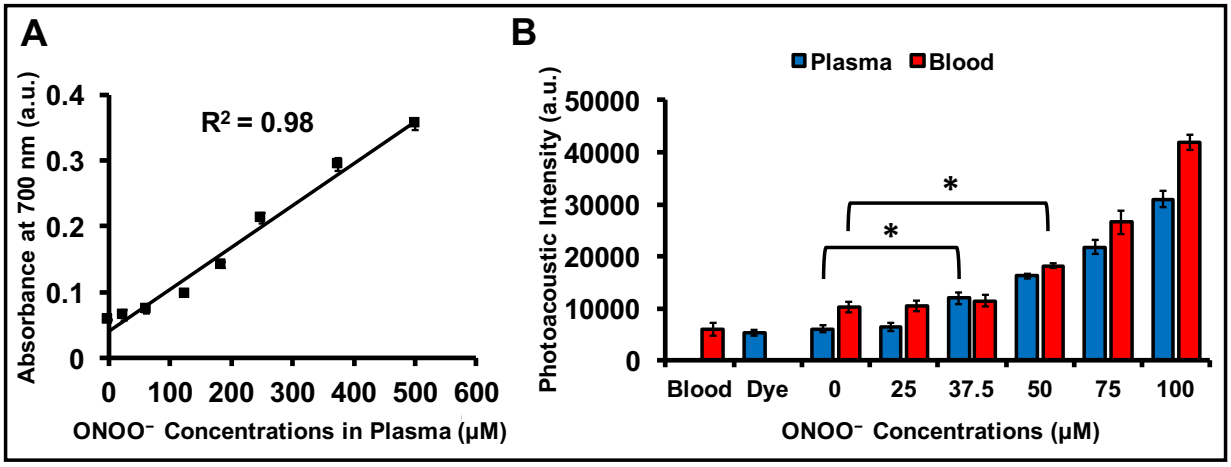

Figure 4. 4 Photoacoustic signal as a function of $ONOO^-$ in normal pooled human plasma and whole blood. A) Linear absorbance response of 125 μM probe in pooled human plasma at 700 nm with various $ONOO^-$ concentrations. B) Photoacoustic response of 125 μM probe in human plasma and fresh human blood to $ONOO^-$ from 0 to 100 μM. The $ONOO^-$ detection limits are 37.5 and 50 μM in plasma and blood, respectively. * indicates p-value < 0.05.

4.3.5 *In vitro* Characterization of Endogenous RONS

We next tested the ability of the probe to measure endogenous RONS produced by murine macrophage RAW 264.7 cells[162-164]. Here, we used DCF-DA as an independent measurement of intracellular RONS [165]. **Figure 5A** shows the brightfield microscopy image of RAW 264.7 cell line.

Figure 5B, C, D, and E represent fluorescence response of RAW cells, RAW cells treated with DCF-DA, RAW cells treated with LPS, RAW cells treated with both LPS and DCF-DA, respectively. The green signals from **Figure 5E** confirm that RONS will be generated by treatment of LPS with RAW 264.7 cells. We used different concentrations of NAC as a free radical scavenger with high membrane permeability [166]. **Figure 5F, G, and H** show decrease of green signal by increasing the concentration of NAC (0.1 mM, 1 mM, and 10 mM). Degradation of fluorescence signal is observed suggesting that the RONS are scavenged by the NAC. **Figure 5I** represents the quantification analysis of fluorescence data in **Figure 5B, C, D, E, F, G, and H**. RAW 264.7 cells treated with LPS and DCF-DA (RONS indicator) have increased fluorescence signal suggesting the generation of endogenous RONS. **Figure 5I** shows that adding NAC at 10 mM scavenged the RONS and decreased fluorescence.

Next, we measured RONS in RAW 264.7 cells with the photoacoustic probe. Here, cells were incubated with LPS as well as the probe (CyBA) with and without NAC (ROS scavenger). **Figure 5J** shows the MIP photoacoustic image for all six samples. RAW cells (control), RAW cells with the probe (+CyBA), RAW cells with LPS (+LPS), RAW cells with LPS, and CyBA (+CyBA+LPS), and RAW cells incubated with LPS/CyBA and various concentrations of NAC (0.1 and 10 mM) were placed in an agar phantom for photoacoustic imaging (**Figure 5J**). There is low signal for RAW cells and RAW cells incubated with LPS but cells incubated with LPS have signal that is ~34-fold higher than the signal from RAW cells only incubated with CyBA; the NAC scavenger with concentrations of 0.1 mM and 10 mM decreased this signal 1.5- and 3.5-fold, respectively. This suggests that NAC scavenges the RONS leading to less photoacoustic signal (**Figure 5K**). These results have been confirmed by fluorescence imaging (**Figure 5I**).

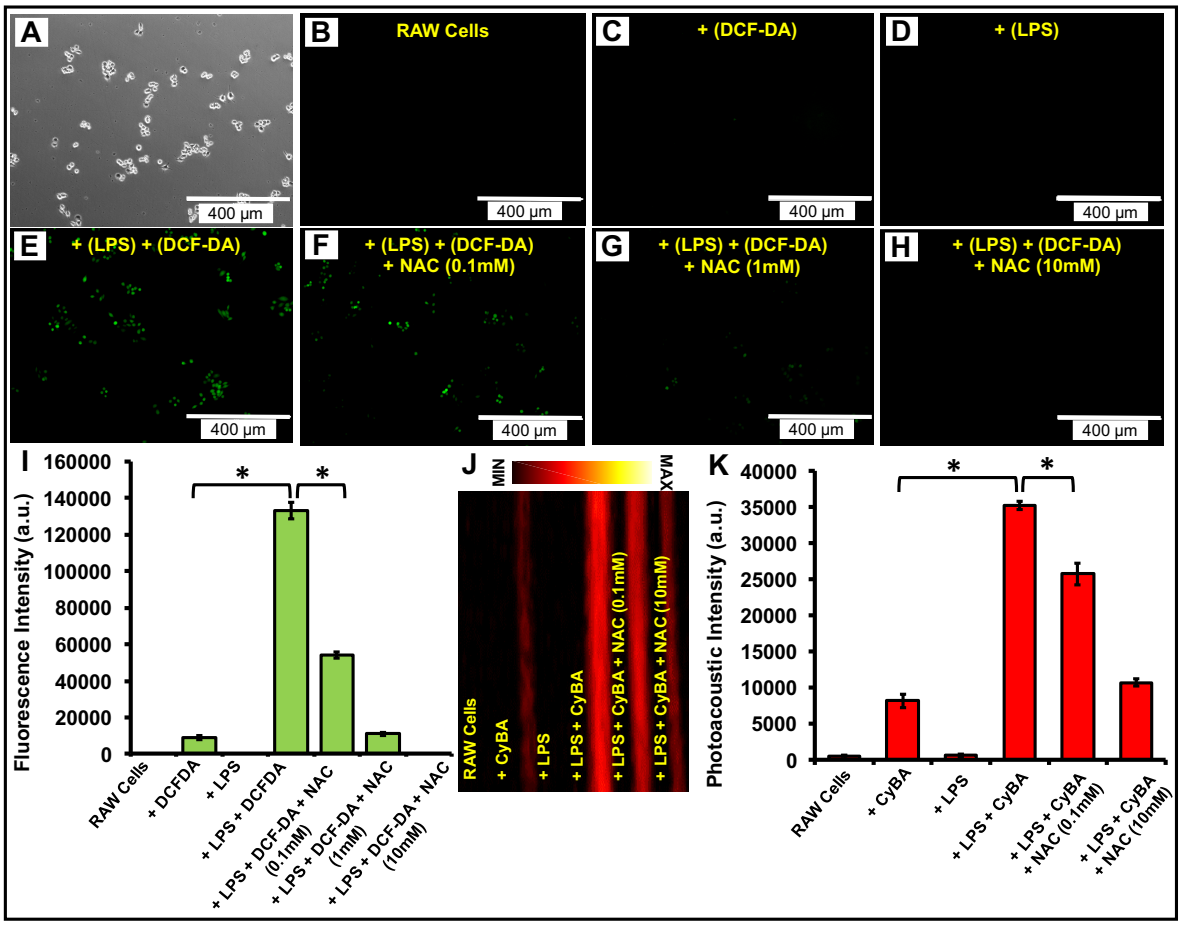

Figure 4. 5 In vitro characterization of endogenous RONS. A) Brightfield microscopy image of RAW 264.7 cells line. B) Fluorescence microscopy image of RAW 264.7 cells. Fluorescence response of C) DCF-DA (20 µM) after incubation with RAW cells, D) LPS (1 µg/mL) after incubation with RAW cells, E) LPS (1 µg/mL) and DCF-DA (20 µM) after incubation with RAW cells. Green signal indicated the presence of RONS in these cells after incubation with LPS. Fluorescence response of LPS and DCF-DA incubated with RAW cells after treating F) 0.1 mM NAC, G) 1 mM NAC, and H) 10 mM NAC. I) Quantitative analysis of fluorescence intensity in all samples in B, C, D, E, F, G, and H. The RONS indicator DCF-DA shows increased fluorescence with LPS stimulation. A NAC RONS scavenger decreases fluorescence. J) The MIP photoacoustic image of RAW cells, RAW cells with the probe (+CyBA) , RAW cells with LPS (+LPS), RAW cells with LPS and CyBA (+CyBA+LPS), and RAW cells incubated with LPS/CyBA and various concentrations of NAC (0.1 and 10 mM). K) Quantitative analysis shows increased photoacoustic signal in the presence of probe and RAW cells incubated with LPS. This suggests RONS generation after monitoring using LED based photoacoustic imaging. * indicates p-value < 0.05.

4.3.6 *In vivo* Photoacoustic Imaging Evaluation of CyBA

We evaluated the ability of CyBA to measure inflammation in mice. **Figures 6A, B, C, D** demonstrate the ultrasound/photoacoustic image from injection location of probe and Zymosan at 0, 10, 20, and 60 minutes, respectively. These figures show the increase of photoacoustic

signal due to tissue diffusion of the probe (CyBA) at edema area (lined yellow circles). Figure 6E represents the quantitative analysis of in vivo photoacoustic imaging evaluation of CyBA. These results revealed that photoacoustic intensity increased gradually and ~3.2-fold increase was observed after 90 minutes of CyBA injection. **Figure 6E** also shows unchanged photoacoustic intensity of only Zymosan and only dye.

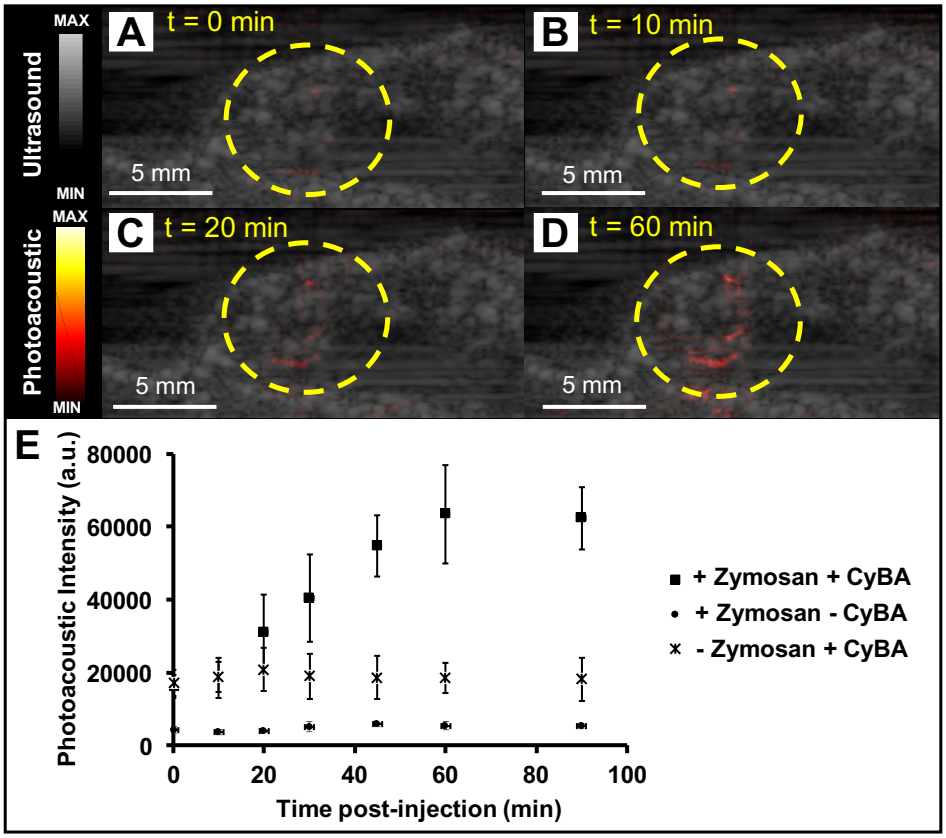

Figure 4. 6 In vivo photoacoustic evaluation of CyBA. A) Ultrasound/photoacoustic image at baseline. Ultrasound/photoacoustic image B) 10, C) 20, and D) 60 minutes after CyBA injection. E) Quantitative analysis of photoacoustic intensity as a function of time post-injection of CyBA. ~3.2-fold increase of photoacoustic intensity after 90 minutes of CyBA injection was observed. Photoacoustic intensity for only Zymosan (+ Zymosan – CyBA) and only CyBA (-Zymosan + CyBA) are unchanged. The error bars represent the standard deviation of measurements among 3 mice.

4.4 Discussion

Detection of H_2O_2 and $ONOO^-$ in biofluids is important to medicine. The concentrations of H_2O_2 in healthy human urine are between 5 to 100 μM and depend on the age and gender of the subject [167]. H_2O_2 concentrations in plasma are as high as 35 μM[168]. Various levels of H_2O_2 (in some cases 100 μM or more) have been measured in the aqueous and vitreous humor[169]. The steady-state biologically concentration of $ONOO^-$ is in the nanomolar to low micromolar level with a basal production rate of 0.1 – 1 μM min^{-1} [170]. In an inflammatory microenvironment, the production rate will increase as high as 50 – 100 μM min^{-1} [170]. We report here a sensitivity of 12.5 and 31 μM for $ONOO^-$ and H_2O_2, respectively, using a LED-based photoacoustic imaging system (**Figure 3C, D**).

LED-based photoacoustic imaging system can monitor RONS *in vitro* and *in vivo* using CyBA. LED-based photoacoustic imaging solves many clinical transition issues for photoacoustic imaging; thus, this technique and probe can be used for clinical monitoring of RONS for keloid diagnosis or in drug toxicity[171].

Other RONS-sensitive photoacoustic probes with a wide range of sensitivities have been reported. Zhang et al. reported a bulky borane-doped nanoprobe with sensitivity of 0.1 μM to detect $ONOO^-$[154]. Xie et al. used a self-assembly approach to measure 150 μM H_2O_2[153]. Kim et al. showed that their gold/silver hybrid nanoparticle could release Ag^+ in presence of RONS such as $ONOO^-$ and H_2O_2 with a sensitivity of 5 and 0.25 mM, respectively[172]. These results show that CyBA probe can measure H_2O_2 under both normal and inflammatory conditions. Although the detection of $ONOO^-$ in steady state is not feasible using our designed probe and LED based system, we could measure $ONOO^-$ under inflammatory conditions *in vivo*.

It is important to mention that most of reported RONS sensors are nanoparticles. One of the advantage of using small molecules sensor is that they can pass the membrane and access to all the cell's compartments with a simple diffusion technique whereas nanoparticle usually will

be trapped in the endosomes[173]. Therefore, this small molecule probe is more appropriate for *in vitro* imaging to monitor endogenous RONS in cells (**Figure 5**).

The change in absorption spectrum or photoacoustic signal of the probe is a function of oxidation of boronate group to phenolic functionality [174]. The oxidation of the boronate group is quantitative and fast. Hence, imaging short-lived species such as RONS with chemodosimeters containing boronate-based probes is feasible in biological environments [175, 176]. The hydroxyl functional group that results from oxidation governs the spectroscopic properties of these boronate-functionalized cyanine dyes [177, 178]. The same chemical transformation is possible through direct oxidation in the presence of peroxynitrite [179]. The oxidation of boronate esters by peroxynitrite is a million times faster than hydrogen peroxide [180]. Thus, it is possible to detect peroxynitrite in real time inside the cells and to image peroxynitrite in animals [181]. This oxidation is then manifested via a bathochromic shift in absorption and increased photoacoustic signal to measure reactive oxygen species (**Figures 2, 3**).

This probe was validated in buffer, plasma, and whole blood (**Figure 4**), and $ONOO^-$ in blood and plasma have been linked to cardiovascular diseases[182]. In the vascular compartment, the formation of $ONOO^-$ is based on the reaction of nitric oxide ($^{\bullet}NO$) with superoxide radical (O_2^{-})[182]. The $ONOO^-$ oxidizes plasmatic components in the intravascular spaces[183] . In addition, up to 40% of intravascularly-generated $ONOO^-$ will diffuse and react into the red blood cells (RBC) before plasma[183, 184]. Therefore, overproduction of either $^{\bullet}NO$ or O_2^{-} can cause intravascular formation of $ONOO^-$.

4.5 Conclusions

We measured RONS species in clinical samples with LED-based photoacoustic imaging. The LED-based photoacoustic imaging offers a significant reduction in the size and cost of optical components. While one limitation of LEDs is their 1000-fold lower power (leading to a need for higher repetition rates), this lower power is actually an advantage here. The higher power from

Nd:YAG lasers photobleaches the dye, but the LED does not. Indeed, this work is the first report of LED-based photoacoustic molecular imaging. Future work will expand this work with LED-based photoacoustic to include higher frequency transducers and a larger portfolio of molecular imaging contrast agents.

Chapter 4, in full, is a reprint of the material as it appears in *Scientific* 9, no. 1 (2019): 1-10. Ali Hariri, Eric Zhao, Ananthakrishna Soundaram Jeevarathinam, Jeanne Lemaster, Jianjian Zhang, and Jesse V. Jokerst. The dissertation author was the primary investigator and author of this paper.

Chapter 5 Non-invasive Staging of Pressure Ulcers Using Photoacoustic Imaging

Ulcers including pressure ulcers and diabetic foot ulcers damage the skin and underlying tissue in people with compromised blood circulation. They are classified into four stages of severity and span from mild reddening of the skin to tissue damage and muscle/bone infections. Here, we used photoacoustic imaging as a non-invasive method for detecting early tissue damage that cannot be visually observed while also staging the disease using quantitative image analysis. We used a mouse model of pressure ulcers by implanting sub-dermal magnets in the dorsal flank and periodically applying an external magnet to the healed implant site. The magnet-induced pressure was applied in cycles, and the extent of ulceration was dictated by the number of cycles. We used both laser- and LED-based photoacoustic imaging tools with 690 nm excitation to evaluate the change in photoacoustic signal and depth of injury. Using laser-based photoacoustic imaging system, we found a 4.4-fold increase in the photoacoustic intensity in stage I versus baseline (no pressure). We also evaluated the depth of injury using photoacoustics. We measured a photoacoustic ulcer depth of 0.38 ± 0.09 mm, 0.74 ± 0.11 mm, 1.63 ± 0.4 mm, and 2.7 ± 0.31 mm (n=4) for stages I, II, III, and IV, respectively. The photoacoustic depth differences between each stage were significant ($p < 0.05$). We also used an LED-based photoacoustic imaging system to detect early stage (stage I) pressure ulcers and observed a 2.5-fold increase in photoacoustic signal. Importantly, we confirmed the capacity of this technique to detect dysregulated skin even before stage I ulcers have erupted. We also observed significant changes in photoacoustic intensity during healing suggesting that this approach can monitor therapy. These findings were confirmed with histology. These results suggest that this photoacoustic-based approach might have clinical value for monitoring skin diseases including pressure ulcers.

5.1 Introduction

Chronic wounds including diabetic ulcers and decubitus ulcers are a pervasive and expensive health care challenge, but tools to diagnose these wounds before they have erupted or evaluate deep tissue response to therapy have remained elusive [185, 186]. Chronic wounds cost the United States medical infrastructure $25B annually with a single diabetic ulcer costing nearly $50,000[187]. These numbers are projected to grow as the population ages. A variety of treatments have been proposed including advanced wound dressings, skin substitutes, hyperbaric oxygen therapy, and growth factor-based therapies[188]; however these have limited capacity for complete healing especially in advanced wounds. Several studies have shown that the *prevention* of wounds offers significant costs savings versus wound treatment[189, 190].

The Healthcare Research and Quality Agency recently estimated that pressure ulcers exert an annual burden of $9.1 – $11.6 billion on the United States' healthcare system [191]. Pressure ulcers consist of necrosis and ulceration[192, 193]. The location of ulceration is where tissues are compressed between bony prominences and hard surfaces. While pressure is the main cause, they are also affected by friction, shearing forces, and moisture[194]. Common risk factors include age > 65, impaired circulation/tissue perfusion, immobilization, undernutrition, decreased sensation, and incontinence[195, 196].

Pressure ulcers are defined by both the depth of ulceration and types of tissue affected [197]. In stage I, the epidermis appears reddened and is characterized by non-blanchable erythema under light pressure. stage II is defined by ruptured skin and a loss of the epidermis and dermis, i.e. the formation of a visual ulcer. stage III involves full skin loss—the lesion extends to subcutaneous tissue. Whole skin loss, muscle necrosis, and damage to tendons and joints occur in stage IV [197-200]. Ulcer necrosis is attributed to the loss of blood flow under sustained pressure [201, 202].

Visual inspection is the standard-of-care for triaging pressure ulcers [201]. In some cases, pressure-sensitive devices are used to alert medical staff when a certain pressure threshold is

exceeded. However, this threshold value is patient-dependent and varies with physiological metrics such as body mass index. The hematron sensor can measure the thermal conductivity of skin, which is correlated to blood flow [203]. However, this sensor cannot monitor the progressive tissue damage that characterizes ulcer development [204]. One of the most well-known methods for pathology detection and tissue characterization is ultrasound elastography [205]. This method extends the typical information supplied by ultrasound—a real time, affordable, and non-invasive modality. Ultrasound elastography is considered an intrinsic factor evaluation to estimate the stiffness of tissue by measuring strain making it applicable to detection of pressure ulcers [206]. This method is limited by superficial tissue assessment, artifacts from compression, and examiner dependency [207]. Nixon et al. utilized laser Doppler imaging to validate the clinical grading of erythema in 37 pressure ulcer patients and showed that this method could monitor a range of blood flow values for normal skin and areas of erythema [197]. However, the laser Doppler imaging method suffers from low penetration depth and therefore monitoring the injury on underlying tissues is impossible. Recently, Swisher et al. used flexible electrode arrays to measure the impedance correlated with tissue health and wound types in a rat model [204]. However, this device is not able to measure the effect of ulcers on subcutaneous fat tissue and muscle.

None of the above methods can monitor the sub-dermal extent of pressure damage in real-time. If damage to sub-dermal tissue could be identified before it is visible by eye, then ulcer-associated morbidity and costs could be prevented before they incur. Therefore, improved methods for detecting the extent of ulceration beneath the skin are of significant interest.

Photoacoustic imaging is a non-invasive and high-resolution technique that combines the contrast of optical imaging and the resolution of ultrasound technique[7, 40, 106]. This hybrid imaging modality offers higher penetration depth with less scatter than optical imaging [79]. In photoacoustic imaging, the tissue is illuminated by a nanosecond laser pulse. The wavelength is selected based on the maximum absorption coefficient of the target tissue. The photons absorbed by the tissue lead to a spatially-confined temperature increases in turn leading to rapid volume expansion and

photoacoustic pressure waves. The generated photoacoustic signals are detected by wideband ultrasound transducers[40, 93]. Photoacoustic signals are received and stored after each laser pulse. Photoacoustic images are produced using various reconstruction algorithms such as delay-and-sum (DAS)[208] or Fourier transform analysis (FTA)[75]. Photoacoustic data overlaid on ultrasound images can report functional information as well as structural details[209].

We hypothesized that the dysregulated vasculature associated with pressure ulcers could be imaged to study their development and predict eruption. Here, for the first time, we introduce the use of photoacoustic imaging to detect early-stage pressure ulcers and monitor their development across different stages using an established murine model [200]. We also utilized this imaging technique to monitor the healing and therapy associated with pressure ulcer treatment.

5.2 Materials and Methods

5.2.1 Animal Model and Validation

Twenty five nude mice (8-10 weeks, 25-35 g) were purchased from the University of California San Diego Animal Care and Use Program (ACP). They were kept in separate cages under a 12-hour light-dark cycle and sterile environment at constant temperature and humidity. All animal experiments were performed in accordance with NIH guidelines and approved by the Institutional Animal Care and Use Committee (IACUC) at the University of California, San Diego.

For the surgical implantation of the internal magnet (diameter of 7 mm and thickness of 1 mm, K&J Magnetic, Inc.), mice were anesthetized with 1-2% isoflurane and placed on a heating bed. The magnet was sterilized via autoclave. The skin was disinfected with povidone iodine at the surgical site. After creating a 5-mm incision, we placed the sterile magnet under the greater gluteus muscle [200] and away from the incision. The incision was sealed using topical tissue adhesive (Abbott Laboratories, IL, USA). We waited ten days for healing to ensure that the surgical wound did not interfere with the pressure induction site.

A sterile external magnet (identical to the internal magnet) was then placed on the skin surface above the implant site at regular intervals. The external magnet was applied in cycles. Each cycle consisted of 2 hours of magnet-induced pressure followed by 1 hour of release. Wassermann et al. showed in their model that 4, 6, 8, and 10 cycles were needed to create stage I, II, III, and IV ulcers, respectively, and we followed this protocol [200]. Imaging was performed either between cycles or between stages. Three mice were sacrificed at baseline conditions and after each stage for histology. The skin and underlying tissue were fixed in buffered 10% formaldehyde solution. Histological analysis (H&E staining) was performed to stage the ulcer as an independent method.

5.2.2 Photoacoustic Imaging

We used both laser and LED-based photoacoustic imaging systems to perform all *in vivo* procedures. The Vevo LAZR (VisualSonic Inc.) is a laser integrated high frequency ultrasound system that utilizes a linear array transducer (LZ-550, Fc = 40 MHz) with optical fibers integrated to both sides of the transducer. For optical excitation, this system uses a Q-switched Nd:YAG laser (4-6 ns pulse width) with a repetition rate of 20 Hz (frame rate of 6 Hz) followed by an optical parametric oscillator (tunable wavelength 680-970 nm). The laser intensity on the surface of the skin was measured at 12.65 ± 0.65 mJ/cm^2 using a laser pyroelectric energy sensor (PE50BF-C, Ophir LLC, USA).

We also used a LED-based photoacoustic imaging system (CYBERDYNE Inc.) [107]. The system is equipped with a 128-element linear array ultrasound transducer with a central frequency of 10 MHz and a bandwidth of 80.9% fitted with two 690 nm LED arrays. The repetition rate of these LEDs is tunable between 1, 2, 3, and 4 K Hz. The pulse width can be changed from 50 ns to 150 ns with a 5-ns step size. The LED intensity at 4 K Hz on the surface of skin was measured at 5.5 μJ/cm^2 using a photodiode sensor (S120C, Thorlabs Inc., USA). In both systems, the

transducer can be scanned to generate three-dimensional (3D) images using a maximum intensity projection (MIP) algorithm.

5.2.3 Quantitative and Statistical Analysis

We collected B-mode photoacoustic/ultrasound images from five different positions above the target site in each animal before initiating the pressure ulcer model (baseline conditions) and after each stage. Each B-mode image contains 256 A-line scans (an A-line scan is simply a single line of collected data). We used 690 nm as the excitation wavelength for all scans. We analyzed our data using two different categories: photoacoustic intensity and photoacoustic depth. The intensity was quantified by first converting all photoacoustic data to 8-bit images; the mean values and standard deviations of the accumulative photoacoustic pixel intensities from 3 mm x 3 mm regions of interest (ROI; each ROI contained 50 A-line scans) were measured using ImageJ (Bethesda, MD, USA).

To quantitate the extent of disease, photoacoustic depth was calculated via 10 A-line intensity profiles from each ROI (every fifth A-line) on all photoacoustic images in all four animals. For the photoacoustic images, we measured the average and standard deviation of ulcer depths from ten different A-lines. The error bars in each figure represent the standard deviation from 4 different animals, and P values lower than 0.05 were considered significantly different.

5.3 Results

Pressure ulcers and diabetic foot ulcers are known to dysregulate the vasculature of tissue, but this dysregulation is often difficult to detect until the lesion has advanced to stage II or III where it has erupted through the skin. Thus, we hypothesized that photoacoustic imaging could be used to detect early stage lesions because it quantitates tissue absorption including from hemoglobin and deoxyhemoglobin. This early-stage detection of pressure ulcers could then be

used to direct treatment and prevent the ulcer from progressing further and disrupting the epithelial barrier—these ruptured lesions are what cause the long-term complications.

We used a rodent model of human pressure ulcers to validate this imaging modality. There are several animal models of pressure ulcers [210-212] including swine and rats [213-215]. They usually apply pressure on the skin against the underlying bone; however, the use of anesthesia during this long procedure is the main limitation of this method [191]. This model is limited to stage I ulcers due to the superficial position of the steel plate under the skin. Wassermann et al. introduced a chronic pressure model to induce all four stages by implanting a magnet under both the skin and deeper tissue layers, including muscle (**Figure. 1**). Their model was verified with histology [200].

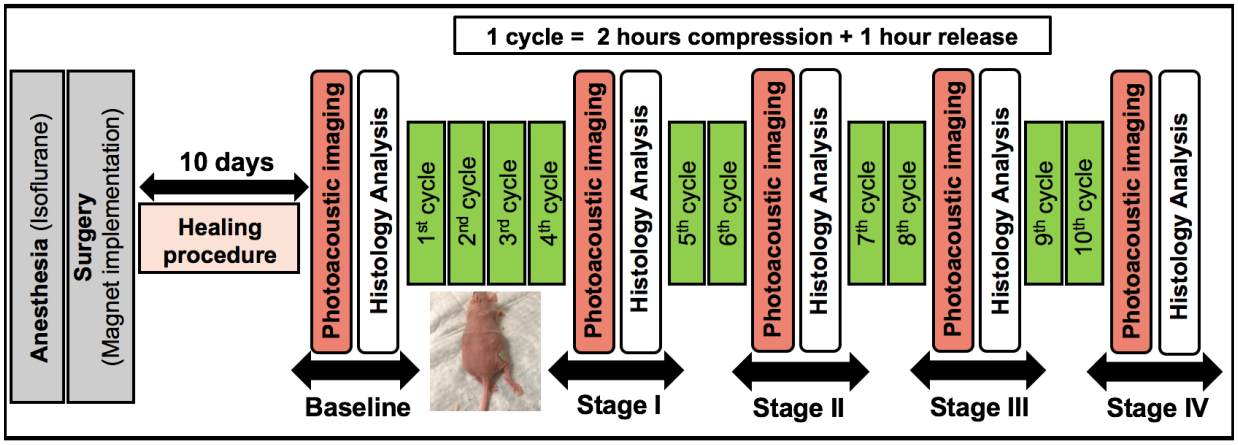

Figure 5. 1 Experimental procedures. All animals were anesthetized with 1-2% isoflurane and placed on a heating bed. The animals were allowed to heal for 10 days after implanting the internal magnet to ensure that the incision did not interfere with the pressure induction site. To create stage I, II, III, and IV pressure ulcers, 4, 6, 8, and 10 cycles were applied, respectively [200]. Each cycle included 2 hours of pressure followed by 1 hour of release. Photoacoustic/ultrasound images were acquired at baseline and at each stage with a 40 MHz transducer. Histology analysis (H&E staining) was used to confirm ulcer stage.

Our first goal was to confirm that the model was created correctly. **Figures 2A(i), A(ii), A(iii)**, and **A(iv)** are photographs of the ulcer sites in mice at stages I, II, III, and IV, respectively. These photographs show the effect of ulcers on the skin but not the underlying tissues. These same animals were then studied with ultrasound/photoacoustic imaging to evaluate the wound depth. **Figure 2B** represents the average histogram of five B-mode baseline fields-of-view for four

animals. All average pixel intensities are lower than 20, and thus we used this number as the threshold for detecting the presence of ulcers using photoacoustic imaging. The inset in **Figure 2B** is a baseline photoacoustic/ultrasound image. **Figures 2C, E, G,** and **I** show the photoacoustic/ultrasound image with progression through stages I, II, III, and IV respectively. **Figures 2D, F, H,** and **J** are representative photoacoustic A-line profiles (yellow dotted line), which correspond to **Figures 2C, E, G,** and **I,** respectively. Note that the full analysis used 10 line profiles per image. We considered pixels with an 8-bit photoacoustic intensity > 20 to represent ulceration of the underlying tissues.

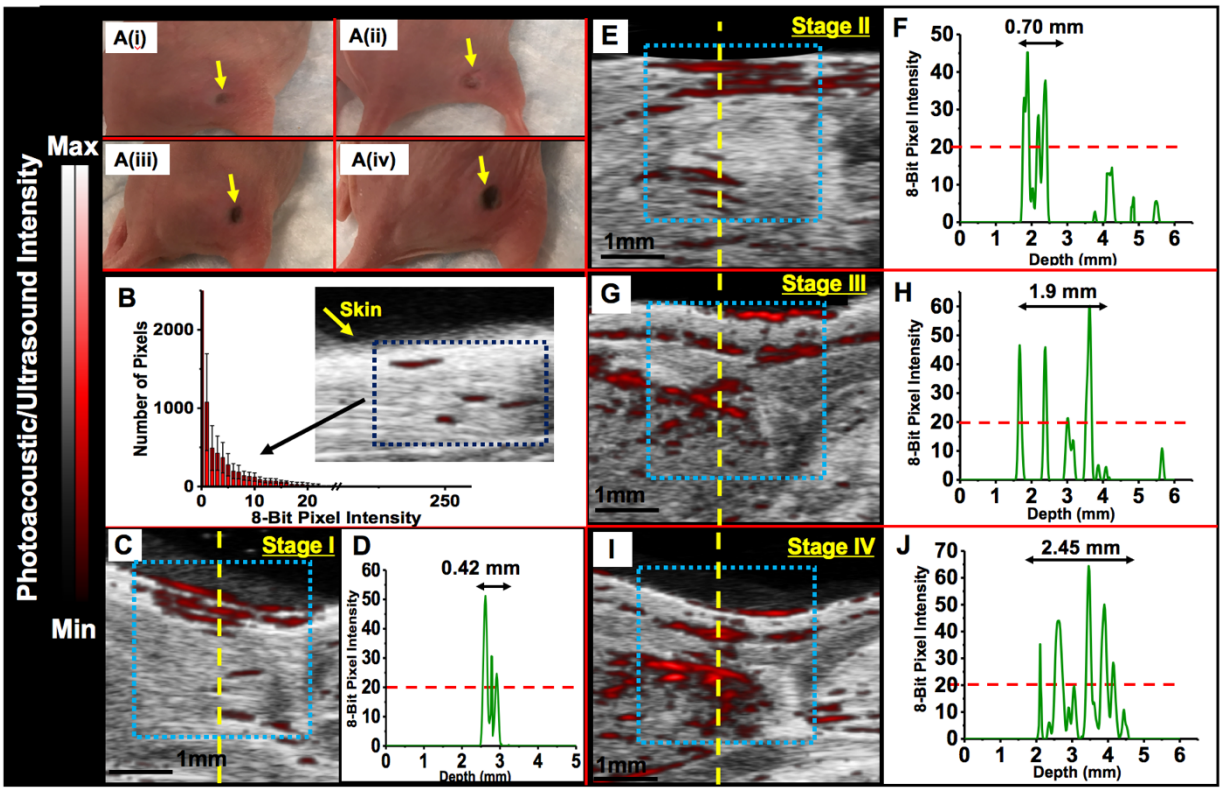

Figure 5. 2 Evaluation of the photoacoustic response to various stages of pressure ulcers. (A(i), A(ii), A(iii), A(iv)) Photographs of stage I, II, III, and IV ulcers. B) Average histogram of baseline photoacoustic pixel intensities. At baseline, all pixel intensities are lower than 20. The inset shows the photoacoustic/ultrasound image at baseline. C) Ultrasound/photoacoustic image at stage I. D) Photoacoustic A-line profile for the dotted yellow line in panel C. We defined photoacoustic pixels with intensities higher than 20 as dysregulated tissue. This was repeated for stage II (E, F), stage III (G, H), and stage IV (I, J). The yellow dotted line shows the A-line profile that was used to quantify the depth of pressure ulcer at different stages. The blue dotted rectangles show the ROIs.

Figure 3A shows that significant changes in photoacoustic intensity were seen between baseline (no pressure ulcer) and all four stages ($p < 0.05$). We found a 4.4-fold increase in photoacoustic intensity at stage I in comparison to the baseline. We saw no any significant changes between stages I-IV in photoacoustic intensity. **Figure 3B** quantifies the photoacoustic depth effect of the pressure ulcer on the skin and underlying tissues. We measured photoacoustic ulcer depths of 0.38 ± 0.09 mm, 0.74 ± 0.11 mm, 1.63 ± 0.4 mm, and 2.7 ± 0.11 mm for stages I, II, III, and IV, respectively. There were significant differences between each stage ($p < 0.05$). We also monitored the animal 30, 60, and 90 minutes after stage I to simulate healing/therapy. **Figure 3C** demonstrates photoacoustic/ultrasound images at 0, 30, 60, and 90 minutes healing after stage I. **Figure 3D** quantifies the photoacoustic intensity effect of healing procedure. We observed significant decrease in photoacoustic intensity after 60 minutes ($p < 0.05$).

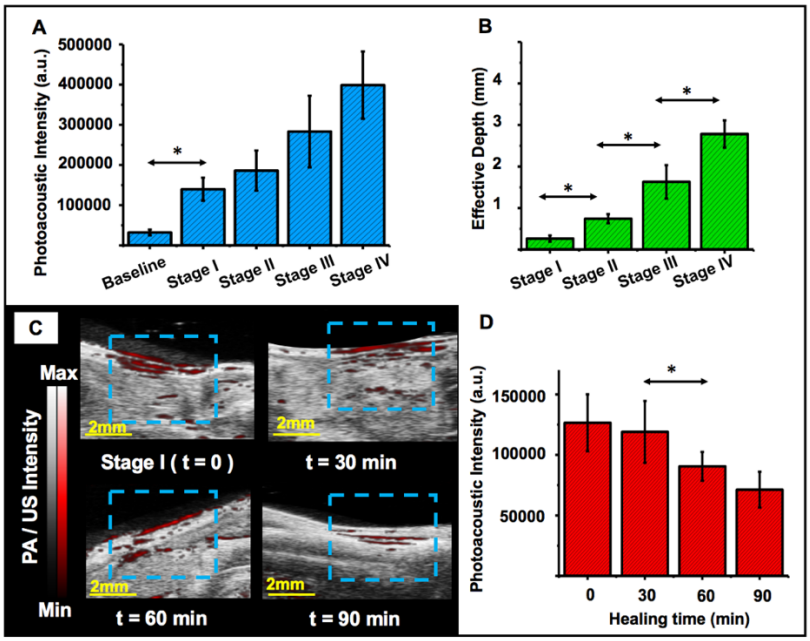

Figure 5. 3 Quantitative and statistical analysis of photoacoustic data at each pressure ulcer stage and during healing. A) Photoacoustic intensity as a function of ulcer stage. There was a significant difference in the photoacoustic intensity at baseline versus stages I, II, III, IV. B) Quantitative analysis for the depth effect at different ulcer stages. Photoacoustic ulcer penetration is significantly different between stages. C) Ultrasound/photoacoustic image at 0, 30, 60, and 90 minutes after stage I to simulate healing/therapy. The blue dotted rectangles show the ROIs. D) Photoacoustic intensity as function of healing time. There was significant change in the photoacoustic intensity after 60 minutes of healing. Error bars represent the standard deviations among 4 (A and B) and 3 (D) different animals. * indicates $p < 0.05$.

These initial data were collected with a laser-based scanner; however, these systems are bulky, delicate, and expensive. More recently, LED-based photoacoustic imaging system have offered important improvements in size, cost, and stability [96, 107, 216]. Thus, we also evaluated these ulcers with LED-based photoacoustics. **Figure 4** shows baseline (top) and stage I ulcers (bottom) via ultrasound, photoacoustic, and overlay ultrasound/photoacoustic using LED excitation. The insets in **Figure 4B** and **C** are photographs of mice without and with pressure ulcers, respectively. We observed a 2.5-fold increase in the photoacoustic signal using the LED-based photoacoustic imaging system at stage I.

These preclinical results suggest that LED-based photoacoustics imaging system (**Figure 4**) has value for monitoring and staging these ulcers. Photoacoustic imaging is able to measure the status of underlying tissues without performing any invasive measurements such as histology (**Figure 1**, **4,** and **5**).

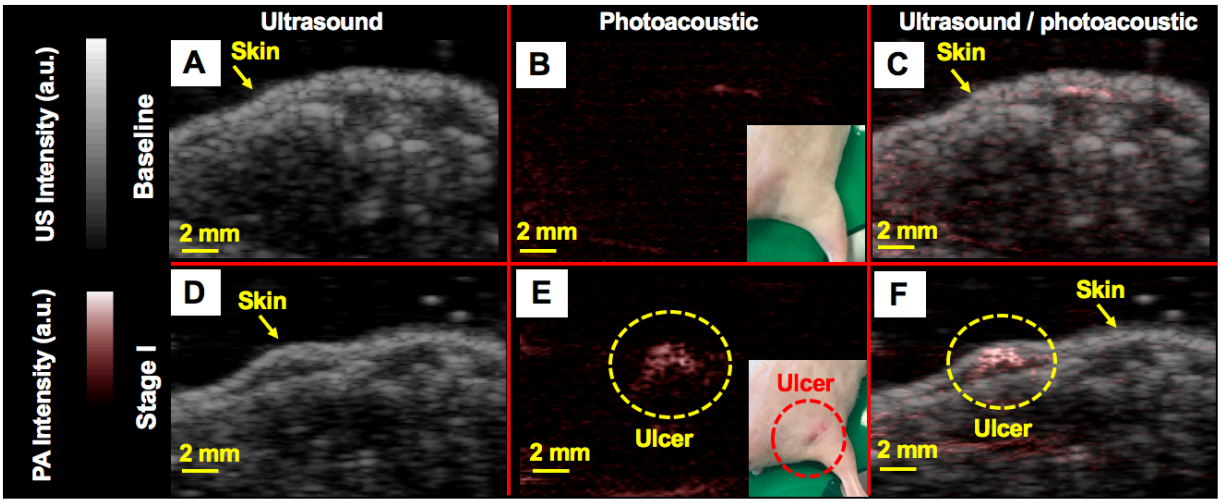

Figure 5. 4 LED-based photoacoustic evaluation of pressure ulcers at stage I. A) B-mode ultrasound image at baseline conditions when no pressure has been applied. B) B-mode photoacoustic image at baseline at the same position as panel A. Minor photoacoustic signal is observed from the epidermis. The photographic inset shows the mouse in absence of ulcer. C) B-mode photoacoustic/ultrasound overlay at baseline conditions. D) B-mode ultrasound image at stage I. E) B-mode photoacoustic image at stage I at the same position as panel D. We observed a 2.5-fold increase in photoacoustic intensity compared to baseline. The photographic inset shows the stage I ulcer. F) B-mode photoacoustic/ultrasound overlay at stage I. The image depth is 1 cm and the scale bars are 2 mm.

Our final goal was to monitor pre-stage I ulcers. Thus, we imaged after each of the cycles between baseline and stage I (**Figure 5A**). There was no difference in photoacoustic intensity among the baseline, first, and second cycles. However, there was a significant increase in photoacoustic intensity between baseline/first cycle/second cycle and third /fourth cycle (p-value < 0.05) (**Figure 5B**). Therefore, photoacoustics can detect ulcers prior to the typical stage I classification. This imaging technique is sensitive enough to detect the mild physiological changes (Third and fourth cycles) that are not visible to the naked eye (**Figure 5B**).

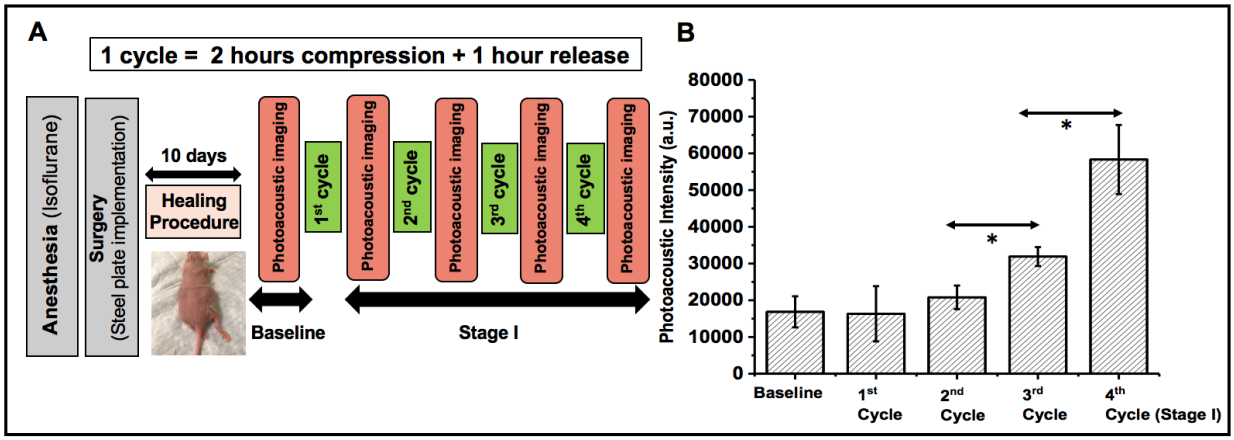

Figure 5. 5 Pressure ulcer detection pre-stage I. A) The experimental procedure. Imaging was done with laser-based photoacoustic system before starting and after each cycle. B) Photoacoustic data at each cycle. We observed a significant difference ($p < 0.05$) in photoacoustic intensity between second versus third cycle and third versus fourth cycle within stage I pressure ulcers. The insets show the photograph images of ulcer on animal body after each cycle.

Finally, we validated the model with histology. **Figures 6A** and **B** are histological images of the skin and underlying tissue, respectively, for the baseline condition (no pressure ulcer). **Figure 6C** shows histology image of the skin at stage I. The red arrow shows the superficial and epidermal skin loss in stage I. **Figure 6D** demonstrates the histology of muscle at stage I—this is normal at stage I. **Figure 6E, F** show histological images of skin and muscle, respectively, at stage II. The structure of dermis and epidermis are now disrupted with mild necrosis on underlying tissues. Stage III leads to full-thickness skin (**Figure 6G**) loss (red arrows) and necrotic areas in

subcutaneous tissue layers (yellow arrows; **Figure 6H**). By stage IV, all skin was removed (red arrow; **Figure 6I**) with large necrotic regions of muscle (yellow arrow, **Figure 6J**). This confirmed that we the imaging data reflects dysregulated biology via the four-stage pressure ulcer from the Wassermann model [200].

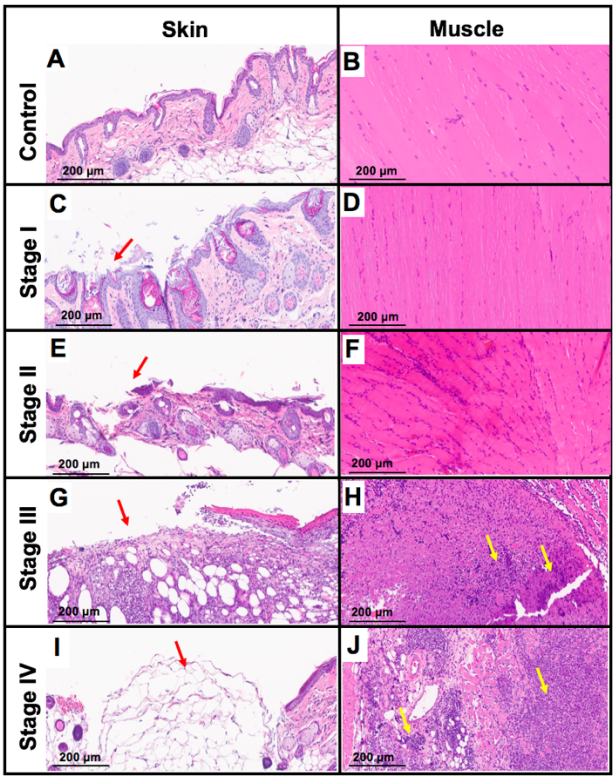

Figure 5. 6 Histological evaluation of pressure ulcer induction model. A) Histology of skin samples for control animals. Typical structure of epidermis and dermis are shown here. B) Histology of muscle sample for control animals. C) Histology of skin sample for the animals with stage I ulcers. The superficial and epidermal skin loss in stage I is shown using a red arrow. D) Histology of muscle sample for the animals with stage I ulcers. No sign of ulcer was found on muscle tissue in stage I of the pressure ulcer. E) Histological images from skin at stage II. The red arrow shows the disruption in the structure of dermis and epidermis. F) Histological image from the muscle. Light necrosis on muscle histology image is observed. G) Histology image of skin in stage III of pressure ulcer. Full loss of epidermis and dermis are the consequences of this stage of ulcer on the skin. H) Muscle histology at stage III of the pressure ulcer. The yellow arrow shows the increased of necrosis on underlying tissues. I) Histological image of skin in stage IV of ulcer. Full skin was removed as the red arrow represents. J) Histology of muscle sample for stage IV animals. Large necrotic regions of the muscle are shown using yellow arrows.

5.4 Discussion

Pressure ulcers are debilitating and can significantly impair quality of life[185]. They are associated with loss of pain sensation and disordered circulation [217, 218]. The gold standard to preventing pressure ulcers include regular patient turning/repositioning[219]. However, there are relatively few tools for molecular-level insight into when to reposition and who to reposition. This work describes a non-invasive, high resolution imaging technique that utilizes photoacoustic signal to detect pressure-induced tissue damage in a nude mouse model *in vivo* and may have utility in predicting the timing of repositioning.

We utilized both the intensity of photoacoustic signal as well as the depth of the photoacoustic signal to characterize ulceration (**Figures 2**, **3**). We and others have shown that the photoacoustic signal changes can report the presence of inflammation and erythema[220, 221]. The photoacoustic depth penetration can distinguish the degree of injury analogous to conventional staging of pressure ulcers. Surprisingly, the signal intensity had less utility in differentiating ulcer stage; however, we can quantify the level of injury by calculating the position of high-intensity (bit depth >20 (8-bit images)).

We used both laser and LED-based equipment. While the laser-based system has more power and higher resolution, LED-based equipment offers significant cost advantages that might aid in clinical translation[107, 216]. The results of LED-based photoacoustic imaging (**Figure 4**) could easily discriminate between different stages. More importantly, this equipment had sufficient sensitivity to detect the mild physiological changes associated with pre-Stage 1 lesions that are not visible to the naked eye (**Figure 5B**)**.** The value of imaging is that it offers a 3D map of the underlying tissue without invasive measurements such as histology (**Figure 1**, **4,** and **5**).

Several imaging techniques have been used for monitoring the pressure ulcers: laser Doppler imaging[197], fluorescence imaging[222], ultrasound imaging[223], magnetic resonance imaging[224], and hyperspectral imaging[225]. They all have their own specific limitations. Laser Doppler, fluorescence, hyperspectral imaging are optical techniques and suffer from low

penetration depth. Thus, these approaches cannot monitor the progress of injury and healing in underlying tissues and muscles[197, 222, 225]. Aoi et al., used conventional ultrasound to monitor the pressure ulcers longitudinally. They concluded that imaging of the discontinuous fascia and heterogeneous hypoechoic area could predict future progression of pressure ulcers[223]. However, this technique lacks contrast and cannot monitor the dysregulated vasculature associated with pressure ulcers. Magnetic resonance imaging has been used to evaluate pressure ulcer in making clinical decisions[226], but is costly and time-consuming. Photoacoustic imaging provides high spatial and temporal resolution as well as sufficient penetration depth for monitoring ulcers. It is also well-suited for multimodal imaging via several other techniques. We used photoacoustic in combination with ultrasound to add contrast to the data.

Photoacoustic approach does have some limitations. First, it is difficult to image through bones, and bones can cause reflections[227]. Second, the amplitude of the photoacoustic signal from deep tissues might not represent the severity of ulcer (**Figure 3A**). This is because photoacoustic signal is directly related to the intensity of incident light on tissue: Deep tissues receive less light due to optical absorption and scattering [228, 229]. This could potentially be solved with image-processing tools than compensate for this reduced fluence [230-232]. Fortunately, we can also circumvent this by quantitating photoacoustic signal *depth* (**Figure 3B**), which does correspond to stage. Third, questions always exist about how well murine models recapitulate human disease; however, the model used here was confirmed histologically to present a phenotype consistent with human ulcers. We also used spectral photoacoustic imaging to measure the oxygen saturation among the different ulcer stages (data not shown). Somewhat surprisingly, there was no trend across stages perhaps because of spectral changes in the epidermis due to scabbing and scarring. This shifting baseline might affect the accuracy of oxygen saturation measurements *in vivo*.

5.5 Conclusion

There is a clinical need for a noninvasive technique that can detect early tissue damage that would otherwise go unnoticed. For the first time, we introduce photoacoustic imaging as a non-invasive tool that can be utilized to detect pressure ulcers before stage I. Here, we used a published protocol to produce pressure ulcers in nude mice. We observed significant changes in photoacoustic intensity even before stage I of pressure ulcer. We also showed that the stage of ulceration can be determined by quantifying the depth of photoacoustic signal from the injury. We also observed that photoacoustic imaging can monitor ulcer healing suggesting potential clinical value in monitoring therapeutic response.

Chapter 5, in full, is a reprint of the material as it appears in *Wound Repair and Regeneration*, 27, no. 5 (2019): 488-496. Ali Hariri, Fang Chen, Colman Moore, Jesse V. Jokerst. The dissertation author was the primary investigator and author of this paper.

Chapter 6 Polyacrylamide Hydrogel Phantoms for Performance Evaluation of Multispectral Photoacoustic Imaging Systems

As photoacoustic imaging (PAI) begins to mature and undergo clinical translation, there is a need for well-validated, standardized performance test methods to support device development, quality control, and regulatory evaluation. Despite recent progress, current PAI phantoms may not adequately replicate tissue light and sound transport over the full range of optical wavelengths and acoustic frequencies employed by reported PAI devices. Here we introduce polyacrylamide (PAA) hydrogel as a candidate material for fabricating stable phantoms with well-characterized optical and acoustic properties that are biologically relevant over a broad range of system design parameters. We evaluated suitability of PAA phantoms for conducting image quality assessment of three PAI systems with substantially different operating parameters including two commercial systems and a custom system. Imaging results indicated that appropriately tuned PAA phantoms are useful tools for assessing and comparing PAI system image quality. These phantoms may also facilitate future standardization of performance test methodology.

6.1 Introduction

Photoacoustic imaging (PAI) is a rapidly emerging technique for mapping light absorption by hemoglobin and deoxyhemoglobin to produce images of vascular morphology and blood oxygen saturation [233]. PAI has shown great potential to provide new functional and molecular imaging biomarkers for many clinical applications including breast cancer detection, oximetry, and surgical guidance, as well as for preclinical research [234-239]. Different imaging applications often require substantially different system designs, which has resulted in a wide variety of system designs described in the literature or currently being sold for preclinical research applications. However, it is unclear how best to objectively and quantitatively evaluate a particular device design and assess its suitability for a given application. There is an outstanding need for well-validated and standardized performance test methods that are suitable for evaluating performance of many types of PAI devices.

Tissue-simulating phantoms play a critical role in medical imaging system development and image quality assessment and often form the foundation of consensus test methods established for mature medical imaging modalities such as ultrasound [240, 241]. Such test methods enable device design optimization, calibration, constancy testing, quality management systems, regulatory decision-making, and accreditation programs. One key challenge for PAI is the need for tissue mimicking materials (TMMs) that simultaneously possess optical properties and acoustic properties that are tunable over a biologically relevant range. An ideal phantom would also accurately mimic tissue over a broad range of optical wavelengths and acoustic frequencies. Unfortunately, many materials described in the literature are characterized over a narrower acoustic frequency range (~1-10 MHz) while PAI systems are available over a broader range (~1-40 MHz). Notably, current IEC standards for ultrasound phantom test methods limit their scope to devices operating over 1-15 MHz. Phantoms described in the literature are also often tailored to a specific instrument and may not be suitable for a wide range of different PAI device designs or configurations, which may hamper device intercomparison and result in duplication of effort

among researchers and device developers. The availability of phantoms based on well-characterized TMMs suitable for many device designs would provide investigators, instrument manufacturers, and regulatory agencies with well-validated tools to assess device performance.

Performance evaluation of PAI devices has been conducted using many materials including ex vivo tissue [242-244]; lipid emulsions such as Intralipid[245]; hydrogels such as gelatin [246], agar/agarose [247-252], and polyvinyl alcohol (PVA) [253]; polyvinyl chloride-plastisol (PVCP) [254, 255]; paraffin gel wax [256, 257]; and styrene-ethylene/butylene-styrene copolymers [258]. Ex vivo tissue is generally undesirable for standardized image quality test methods due to its variable properties and morphology, heterogeneity, poor reproducibility, and short shelf life. Intralipid is commonly used in optical phantoms but possesses lower acoustic attenuation than tissue [259]. Hydrogel-based TMMs offer easy preparation and fabrication, tunable composition, and good dopant miscibility but typically suffer from poor shelf life and low mechanical strength. PVA cryogels with adjustable stiffness and turbidity can be formed through repeated freeze-thaw cycling. However, the optical and acoustic properties cannot be tuned independently, and slow dye migration from solid inclusions has been reported [260]. Elastomers such as polyurethane or polydimethylsiloxane (PDMS) have been used for ultrasound imaging phantoms, but some of these materials may not accurately mimic the acoustic properties of soft tissues [258, 261]. Recently, promising non-aqueous materials have been specifically developed as photoacoustic TMMs such as gel wax [257] and polyvinyl chloride plastisol (PVCP) [262-264]. These materials have been shown to possess relatively high mechanical strength and optical tunability, and acoustic tunability has been demonstrated in PVCP for breast-mimicking formulations. However, the acoustic properties of these TMMs at higher frequencies (e.g., > 15 MHz) have not been reported and may be more highly attenuating than some soft tissues other than breast. These materials also typically require high preparation temperatures, potentially limiting compatible dopant options.

Polyacrylamide (PAA) is a hydrogel that has been used previously for ultrasound phantom TMMs, including in Zerdine® (CIRS, Inc., Norfolk, VA), a commercially available TMM [265]. PAA

offers simple preparation, short curing times, low viscosity (thus good dopant miscibility), reduced bacterial infiltration [266], and longer shelf life. PAA may also provide greater mechanical strength and robustness than agar/gelatin hydrogels due to the use of cross-linking polymerization instead of a thermal gelation process. A high degree of optical and acoustic tunability is expected [267-270]. While the acrylamide polymerization reaction is exothermic, PAA has lower preparation temperatures than PVCP and gel-wax phantoms. Like other hydrogels, PAA is still subject to desiccation and should be sealed to maximize product lifetime. While concerns have been raised regarding toxicity of potential residual acrylamide monomer [267], this risk is mitigated through proper safety procedures during production and appropriate design of sealed phantom housings. PAA blocks have been used in photoacoustic contrast agent studies, but the phantom optical and acoustic properties were not adjusted to provide biologically relevant background [271, 272]. To the best of our knowledge, PAA has not been used to build image quality phantoms suitable for PAI.

Our overall goal is to develop stable, well-characterized, tunable, and biologically relevant phantoms with broad tunability for a wide array of PAI devices. To this end, our study objectives were to develop and characterize PAA as a new photoacoustic TMM, construct PAA image quality test phantoms, and demonstrate utility through image quality testing of three different PAI systems.

6.2 Methods and Materials

Given the wide variety of PAI applications, TMMs for PAI should offer highly tunable optical and acoustic properties in order to adequately mimic different specific tissues or to represent generic tissue-like conditions. Most photoacoustic TMM development has focused on producing phantoms with biologically relevant optical absorption coefficient (, optical reduced scattering coefficient (, speed of sound (, and acoustic attenuation coefficient () [263]. In this study, we aimed to produce a TMM with broad optical and acoustic tunability and to mimic a generic soft tissue. The target and values at 800 nm were 0.1 cm^{-1} and 10 cm^{-1}, respectively, which are generally similar to soft tissues [273]. The target was 1,540 m/s as taken from ultrasound standards [240, 274];

however, selecting an appropriate target was challenging due to the wide range of transducer frequencies employed by the PAI systems tested in this study. To ensure phantoms were biologically relevant, yet not overly attenuating at higher frequencies (beyond our current characterization equipment's range), we chose a target of 0.2 dB/cm/MHz.

6.2.1 Polyacrylamide Preparation

Polyacrylamide (PAA) hydrogels are formed through crosslinking copolymerization of acrylamide and N,N'-methylene bisacrylamide in aqueous solution [275]. A 40% w/v acrylamide solution containing 19:1 acrylamide:bisacrylamide (AM9024, Thermo Fisher Scientific, Inc., Waltham, MA) was diluted in deionized water, and ammonium persulfate (APS) solution (A7460, Sigma-Aldrich, Inc., St. Louis, MO) was added to initiate the polymerization. The solution was degassed in a steel vacuum chamber for 1 hour and then N,N,N',N'-tetramethylethylenediamine (TEMED, Sigma-Aldrich) was added to accelerate free radical formation from APS. TEMED was used within 10 months of purchase. The PAA solution was then mixed, immediately poured into phantom molds, and cured at room temperature for 1 hr, with solidification occurring within 5 min. Phantoms were manually tumbled during curing to minimize gravitational settling of dopants [276, 277].

6.2.2 TMM Characterization

To evaluate the acoustic property tunability of PAA, acoustic properties were first measured in samples with varying acrylamide concentration of 8-20% w/v. The base PAA hydrogel does not impart significant acoustic scattering, and thus we increased acoustic attenuation and backscattering by doping 12% w/v acrylamide samples with soda lime glass beads at concentrations of 0-10 mg/mL (38-63 μm diameter, Potter Industries LLC, Malvern, PA). This ensures that the phantoms are also suitable for bimodal ultrasound and photoacoustic imaging [278, 279]. PAA acoustic properties were characterized using a broadband through-

transmission substitution technique [280, 281] in a tank containing deionized, degassed water. This technique has been previously validated against time-delay spectrometry measurements [282]. PAA samples were cured in nontreated tissue cell culture flasks (087721J, Thermo Fisher Scientific) as shown in Figure 1A. Flasks were placed in a water bath between a pair of co-axially aligned broadband transducers (A313S-SU, Olympus, Inc., Waltham, MA) with one transducer acting as a transmitter and the other as a detector. Both transducers had 15 MHz center frequencies and 0.63 cm diameters. Transducers were connected to a pulser/receiver (Panametrics 5900PR, Olympus) and received ultrasound signals were digitized at 2.5 GHz using an oscilloscope (MDO3054, Tektronix, Inc., Beaverton, OR). An average of 512 measurements was taken at each of 4-6 locations per sample. Group velocity in the sample, , was calculated as

(1)

where is the speed of sound in water, is the transit time delay between the two measurements, and is the flask thickness. The acoustic attenuation coefficient vs. frequency, in dB, was calculated as

(2)

Where is the power spectrum measured through a PAA-filled flask and is the acoustic power spectrum measured in a water-filled flask. This approach cancels out acoustic transfer characteristics of the flask walls, assuming that differences in acoustic impedances between the gel and water were small enough that differences in transmission coefficients could be neglected. For a gel sample in water, if the differences in and density between gel and water are less than 7% and 20%, respectively (both true in these experiments), then it can be shown the product of intensity transmission coefficients at both interfaces exceeds 95% [283]. Attenuation coefficient

spectra were fitted to the power-law relationship over the range from 6-18 MHz where and n are fitting parameters.

To characterize acoustic backscattering, ultrasound images of PAA samples with varying glass bead concentrations were acquired using FDA's custom PAI system (see Section 2.6). Mean image amplitude was measured over a 12 mm x 15 mm (width by height) region of interest (ROI) and compared against similar measurements in a commercial tissue-mimicking ultrasound phantom (Model 040GSE, CIRS, Inc., VA) [263]. Image acquisition and display settings were fixed for both phantoms.

To produce phantoms with biologically relevant optical properties over a broad range of wavelengths, PAA was doped with India ink (Super black India ink, Speedball Art Products Co., NC) and anatase titanium dioxide (TiO_2, 232033, Sigma-Aldrich). These dopants are commonly used in both optical and PAI phantoms, including hydrogels [284, 285]. These TiO_2 particles have an average diameter of 550 nm in water [263]. Samples comprising 12% w/v PAA were doped with 0.004 – 0.010% v/v India ink or 0.4 – 1.2 mg/mL TiO_2. Samples were prepared in C-shaped molds with 38.4 mm diameter and 2.5 mm thickness, which were glued between a pair of 75 mm x 50 mm x 1 mm glass slides with an assumed refractive index of 1.5 (Figure 1B). Total transmittance and diffuse reflectance of samples were measured over 400-1100 nm using an integrating sphere spectrophotometer (Lambda 1050, PerkinElmer, MA). and were calculated from these data using the inverse adding-doubling (IAD) algorithm [286]. Sphere measurements were calibrated using a Spectralon 99% reflectance standard (Labsphere, Inc., Sutton, NH), and transmittance and reflectance baselines were measured following the IAD manual [287]. Sample thickness was measured using digital calipers with 0.02 mm resolution, subtracting the thickness of the glass slides. The 2.5 mm sample thickness is appropriate for IAD and consistent with previous studies [288, 289]. Because unaccounted light losses can cause IAD to overestimate absorption, values were calibrated against a 12% PAA sample with 2 mg/mL TiO_2 but no ink, which was assumed to have absorption equal to that of water [290]. Sample scattering anisotropy factor and refractive index

were assumed to be 0.9 and 1.34, respectively. Varying anisotropy factor from 0 to 0.9 in a representative PAA dataset varied μ_a (800 nm) and μ_s' (800 nm) by ± 3% and ± 2%, respectively. PAA refractive index at 589 nm has been reported as 1.35 [291], and may be slightly lower in the NIR assuming normal dispersion similar to water [290]. Varying refractive index from 1.33-1.35 led to changes in μ_a (800 nm) and μ_s' (800 nm) of ± 5% and ± 0.2%, respectively.

Ideally, image quality phantoms should offer high mechanical durability and stability of intrinsic properties over time. We prepared optical and acoustic characterization test samples as described above and measured their optical or acoustic properties at 1 day, 8 weeks, and 12 weeks post-fabrication. Optical stability was measured in a set of six 12% w/v PAA samples each containing 0.7 mg/ml TiO_2 and 0.0045% v/v India ink. Acoustic stability was measured in a set of seven 12% w/v PAA samples containing 0-10 mg/ml glass beads to assess dependence of stability on potential glass bead settling. All samples were stored at room temperature and pressure. Samples were weighed at each measurement timepoint to monitor mass loss over time. Average and standard deviation of sample mass, optical properties, and acoustic properties was computed per timepoint, and comparisons between timepoints were made using student's t-test.

6.2.3 Phantom Imaging and Image Analysis

To demonstrate utility of PAA phantoms, we sought to evaluate image quality of three PAI instruments using phantoms formed in 7 cm x 7 cm x 6 cm acrylic molds (Figure 1C). We constructed two image quality phantoms: 1) a "resolution" phantom intended to quantify axial and lateral spatial resolution, and 2) a "penetration" phantom intended to quantify maximum depth of visualization. The resolution phantom contained a column of 50 μm diameter black nylon monofilament sutures (Teleflex Medical OEM, Gurney, IL) at depths of 5-35 mm (Figure 1D). The penetration phantom contained an array of light-wall polytetrafluoroethylene tubes (Component Supply Co., Sparta, TN) at depths of 5-35 mm (Figure 1E). In both phantoms, the first five targets in depth were spaced closer together to ensure a sufficient number of targets in the field of view

for high-frequency PAI systems, while the deeper targets were more sparse to cover low-frequency systems. Tubes were filled with India ink solutions with three different values of 8 cm^{-1}, 4 cm^{-1}, and 2 cm^{-1}. Here, 4 cm^{-1} represents the expected of hemoglobin at 800 nm (an isosbestic point) for a total hemoglobin concentration of 13.9 g/dL, which is within the normal ranges for adult males (13.5 – 17.5 g/dl) and females (12 – 16.0 g/dl) [292]. A value of 2 cm^{-1} thus represents a low-contrast scenario such as anemia (~7 g/dl) while 8 cm^{-1} represents a high-contrast scenario such as using a contrast agent. PAA phantoms were fabricated from a 400 mL batch of solution using a final recipe of 12% w/v acrylamide, 0.08% w/v APS, 0.2% v/v TEMED, 0.7 mg/ml TiO_2, 0.00225% v/v India ink, and 6 mg/ml glass beads. Phantoms took approx. 5 min to solidify and were allowed to cure for 1 hr, with a maximum surface temperature of 46°C as measured by an infrared thermometer.

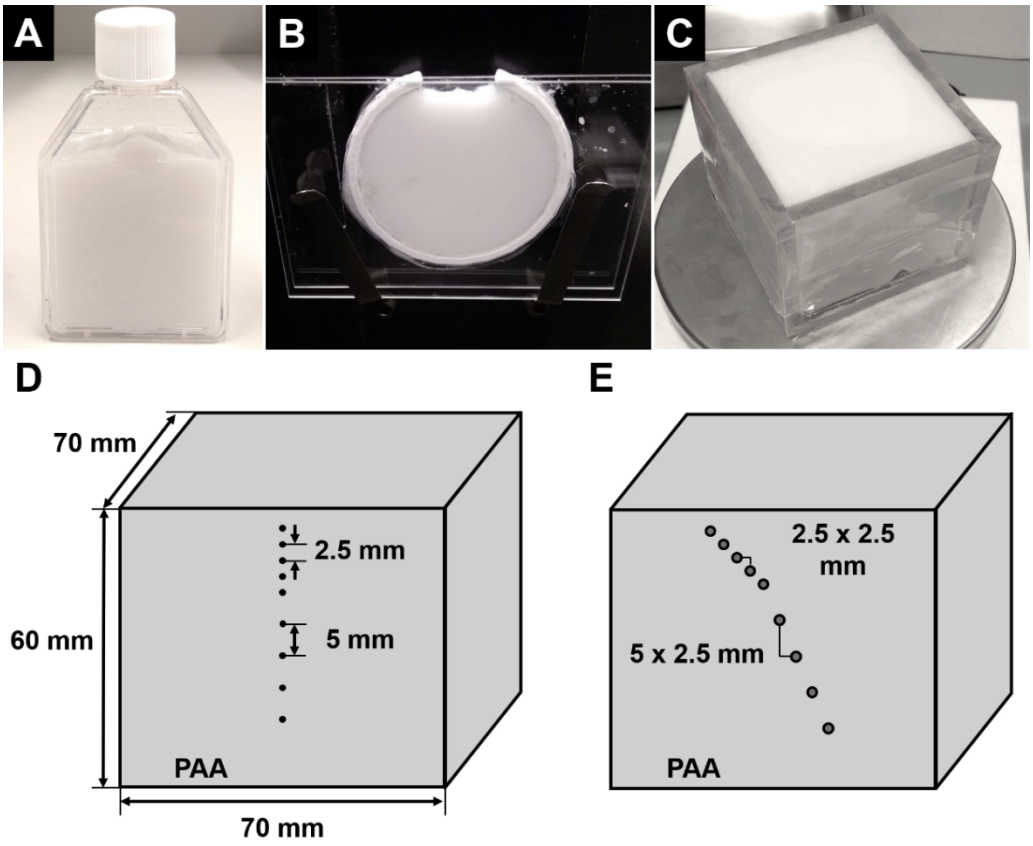

Figure 6. 1 TMM phantoms in different configurations. PAA gels were cured in (A) nontreated tissue cell culture flasks and (B) C-shaped molds glued between a pair of glass slides for acoustic and optical characterization, respectively. Photograph of the penetration phantom (C). Schematics of the resolution phantom containing a column of 50 µm-diameter nylon filaments (D) and penetration phantom containing an array of ink-filled tubes (0.56 mm inner diameter, 0.71 mm outer diameter) (E). Imaging was performed from the top surface in each phantom.

We used these PAA phantoms to conduct a multi-site phantom-based image quality assessment of three different PAI systems including a custom system located at FDA and two commercial systems at UCSD [107, 263, 293]. Figure 2 shows transducer and light delivery geometries for each system. The custom system combines an optical parametric oscillator (OPO) delivering 5 ns pulses at 10 Hz pulse repetition rate, 690-950 nm tunable wavelength, and 8-10 mJ/cm^2 radiant exposure (Phocus Mobile, Opotek Inc., CA) with a 128-channel ultrasound acquisition system (Vantage 128, Verasonics Inc., WA). PAI was performed with a 7 MHz linear array transducer covered in aluminum foil and placed in contact with the imaging surface (L11-4v,

Verasonics) and a 5 mm x 40 mm elliptical optical beam aligned adjacent to the transducer. The foil reduces light absorption at the transducer face, which generates unwanted photoacoustic image clutter. Image reconstruction was performed using a proprietary pixel-oriented delay and sum algorithm from Verasonics [294], and images were pulse energy-compensated using an internal energy meter.

UCSD's available systems included an AcousticX (CYBERDYNE Inc., Japan) and a Vevo LAZR (FUJIFILM VisualSonics, Inc., Ontario, Canada). The AcousticX performs optical excitation using high-density arrays of high-power light-emitting diodes (LEDs) attached to either side of a 10 MHz linear array transducer. LED output has adjustable pulse duration (50-150 ns) and pulse repetition rate (up to 4 kHz). Several swappable LED arrays are available in various wavelengths or pairs of wavelengths; in this study we used 850 nm LED arrays. Image reconstruction was performed using built-in Fourier transform analysis. The Vevo LAZR is an OPO-based system delivering 4-6 ns pulses at 20 Hz repetition rate, 680-970 nm tunable wavelength. Several linear-array transducers are available at different center frequencies (15, 21, 30, and 40 MHz), and each transducer includes an integrated housing containing optical fiber bundles. Preliminary phantom measurements indicated poor target detectability in phantoms using the 21, 30, and 40 MHz probes (data not shown), possibly due to higher acoustic scattering of PAA. Thus, phantom imaging was performed only using the 15 MHz probe (LZ201) in this study.

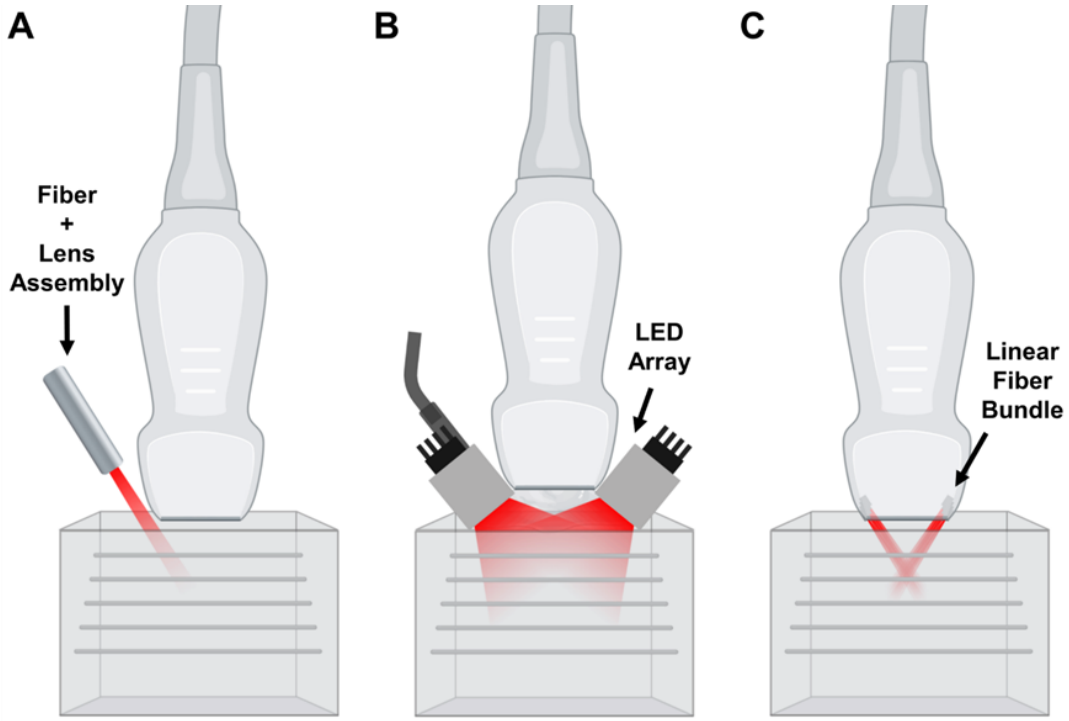

Figure 6. 2 Schematics of transducer and light delivery geometries. (A) custom system, (B) AcousticX, and (C) Vevo LAZR.

While the three PAI systems have different configurations and software settings, we developed a general set of imaging guidelines intended to standardize data collection across systems. Transducers were coupled to the phantom with ultrasound gel and aligned such that target filaments or tubes were normal to the image plane. Energy was set to maximum output, and imaging was performed at 850 nm. Images were acquired at five locations in each phantom following ultrasound test method recommendations [295]. At 850 nm, the radiant exposures for the custom and Vevo systems measured with a 3.5 mm aperture were approximately 8.0 ± 0.4 mJ/cm^2 and 8.6 ± 0.3 mJ/cm^2, respectively. The AcousticX output was set to maximum energy at 4 kHz , which produced a radiant exposure of 28 ± 0.2 μJ/cm^2 measured with a 12 mm aperture (a larger aperture was needed to measure lower pulse energies). For penetration phantom imaging, the tube array was filled sequentially with India ink solutions with = 2, 4, or 8 cm^{-1}. Channels were

rinsed with water between solutions. Reconstruction speed of sound was fixed at 1,540 m/s for all systems.

Imaging phantoms were constructed at FDA, weighed, and then imaged using the custom PAI system. Phantoms were packaged in sealed plastic bags and delivered to UCSD by commercial passenger air transport (i.e., stored in the passenger cabin to avoid possible temperature and pressure differences in the cargo hold). On arrival, phantoms were inspected for damage and weighed to check for desiccation during shipment. Imaging was then performed on the AcousticX and Vevo LAZR systems following the same data acquisition protocol used with the custom system.

Photoacoustic images are typically log compressed to reduce dynamic range of the data and thus improve image visualization by a human reader. However, user-adjustable display settings such as display dynamic range, gain, time-gain compensation, log compression, and thresholding can change image content and thus affect image quality metrics. In this study we evaluated both the preprocessed image data (referred to here as linear amplitude images) and the processed, log-compressed 8-bit images (referred to as displayed images). Following recommendations from ultrasound image quality standards, we selected display settings such that images were not saturated and background was not clipped, and kept display settings fixed during image quality analysis [241, 274].

To quantify spatial resolution, a 2 x 2 mm rectangular region of interest (ROI) was drawn over each imaged filament target in linear amplitude images. Vertical and horizontal amplitude profiles intersecting with the maximum amplitude pixel within the ROI were used to calculate the axial and lateral resolution based on the full width at half maximum (FWHM) or -6 dB width [295]. To evaluate maximum imaging depth, 1 x 1 mm ROIs were drawn over tube targets and equal-sized background ROIs were drawn 2 mm to the right of each target. Image quality metrics including signal-to-noise ratio (SNR), contrast-to-noise ratio (CNR), signal-to-background ratio (SBR), and

contrast ratio (CR, in dB) for each target using either the linear amplitude image, , or the displayed image, . These metrics may be written as:

$$SNR_{linear} = \frac{A_t}{\sigma_{A,b}} \quad CNR_{linear} = \frac{A_t - A_b}{\sigma_{A,b}} \quad SBR_{linear} = \frac{A_t}{A_b} \quad CR_{linear} = 20\log_{10}\left(\frac{A_t}{A_b}\right)$$
$$SNR_{disp} = \frac{D_t}{\sigma_{D,b}} \quad CNR_{disp} = \frac{D_t - D_b}{\sigma_{D,b}} \quad SBR_{disp} = \frac{D_t}{D_b} \quad CR_{disp} = \frac{DR}{255}\left(D_t - D_b\right) \tag{3}$$

Where and are average target ROI values, and are average background ROI values, and are standard deviations of the background ROI values, and is the display dynamic range in dB [143, 254, 274, 296]. Some correlations are evident between these metrics. For example, is expected to be similar to because its definition inverts the linear lookup table that converts log-compressed image data to 0-255 pixel values. Also, given values of any two of , , and , the third metric may be determined via the following relationship:

(4)

This relationship also illustrates how CNR captures both the effects of target contrast through SBR and background variation through SNR. Despite these correlations, our intent was to evaluate and compare results to determine the most appropriate use of these metrics.

6.3 Results

6.3.1 TMM Properties

The acoustic properties of the various PAA formulations are shown in **Error! Reference s ource not found.**. Both and significantly increased with acrylamide concentration. Acoustic attenuation was linear with PAA concentration up to 16% PAA ($R^2 > 0.97$), with 20% PAA samples having higher attenuation than expected from a linear fit. PAA hydrogels with very high acrylamide concentration became significantly stiffer, but these samples were also less homogenous as evidenced by hazy streaks and interfaces. This heterogeneity may be due to uneven heating and

crosslinking during the exothermic polymerization reaction [269, 270]. As expected, increased with glass bead concentration, but did not significantly change (data not shown). Therefore, we could tune by varying acrylamide concentration, then tune by varying glass bead concentration. PAA samples doped with glass beads produced significant acoustic backscattering as seen in the B-mode ultrasound images (**Error! Reference source not found.**). Quantitative analysis of u ltrasound images indicated that PAA with a glass bead concentration of 6 mg/ml produced similar ultrasound image amplitudes as the commercial reference phantom. This concentration was much lower than that used in previous PVCP phantoms [263], which may be due acoustic attenuation in PVCP, greater acoustic mismatch between the particle and medium, or differences in particle aggregation. Based on acoustic characterization experiments, we selected a formulation comprising 12% w/v acrylamide and 6 mg/ml glass beads for further phantom development.

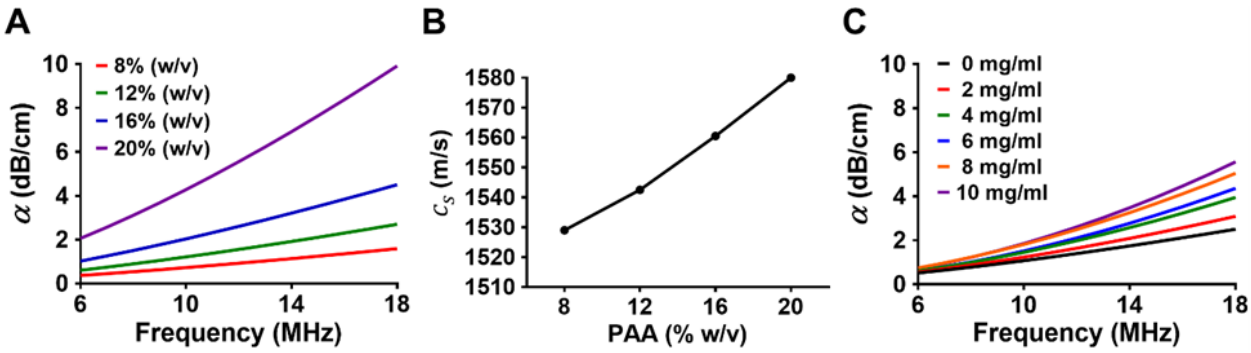

Figure 6. 3 TMM acoustic properties. Effect of PAA concentration on (A) and (B). (C) shows for various glass blead concentrations. Error bars omitted for clarity; typical standard deviations for and were < 1 m/s and < 5%, respectively**.**

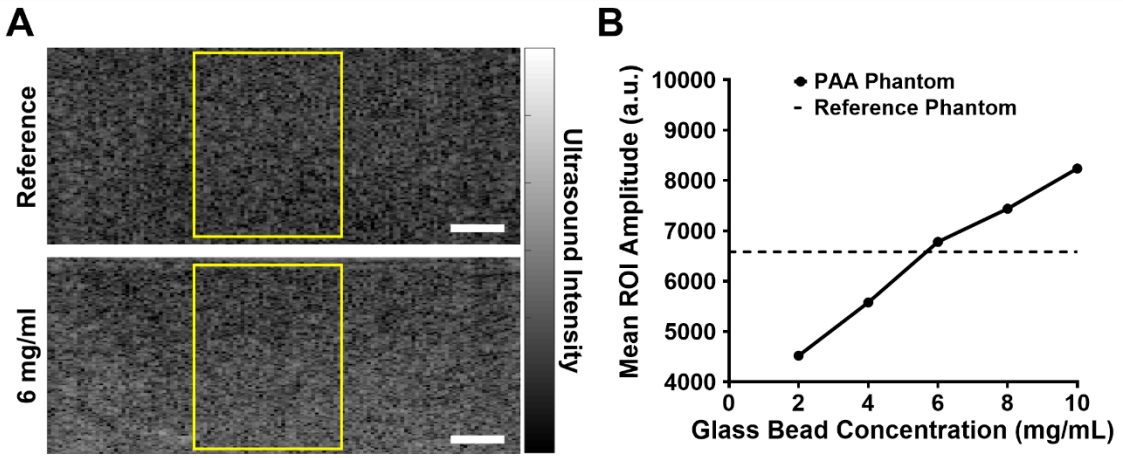

Figure 6. 4 Quantitative analysis of ultrasound images with a glass bead. (A) Ultrasound images of the CIRS reference phantom and PAA sample with 6 mg/ml glass beads. Yellow boxes denote measurement ROIs. Scale bars = 5 mm. (B) Mean ROI amplitude vs. glass bead concentration compared to the reference phantom (dotted line).

The and spectra of PAA hydrogels were readily tuned using India ink and TiO_2 (**Error! Reference source not found.**). A high degree of linearity of optical properties with respect to dopant concentration was observed for both India ink and TiO_2. These curves were used to fine-tune PAA to match targeted property values. As expected, India ink produced relative flat spectra except for the increased absorption due to water absorption above 925 nm. TiO_2 produced spectra showing a monotonic decrease with wavelength.

PAA samples measured over time showed good resistance to desiccation with no statistically significant mass loss after 8 weeks and <1% mass loss over 12 weeks. This may be attributed in part to the samples being stored in airtight containers needed for water bath immersion in acoustic characterization experiments. This housing approach is consistent with commercial hydrogel phantom designs that typically use a thin plastic membrane or “acoustic window” to seal the hydrogel from the environment but allow high ultrasound transmission through the imaging surface. After 12 weeks, there was a small but statistically significant decrease in speed of sound of 4.1 ± 1.2 m/s (0.2 ± 0.07%). Acoustic attenuation was highly stable, with at 10 MHz decreasing by 0.02 ± 0.038 dB/cm (1.4 ± 2.8%) over 12 weeks. These variations are within

acoustic property tolerances recommended in the ultrasound standard IEC 61391-1:2017 (± 10%)[240]. Optical properties showed greater variation, but no significant trends were observed with time. At 12 weeks, was 11 ± 1.6% lower (averaged over 700 – 950 nm), and was 0.2 ± 1.8% lower. This variation may be partly attributed to uncertainty in the integrating sphere measurements and the IAD calculations.

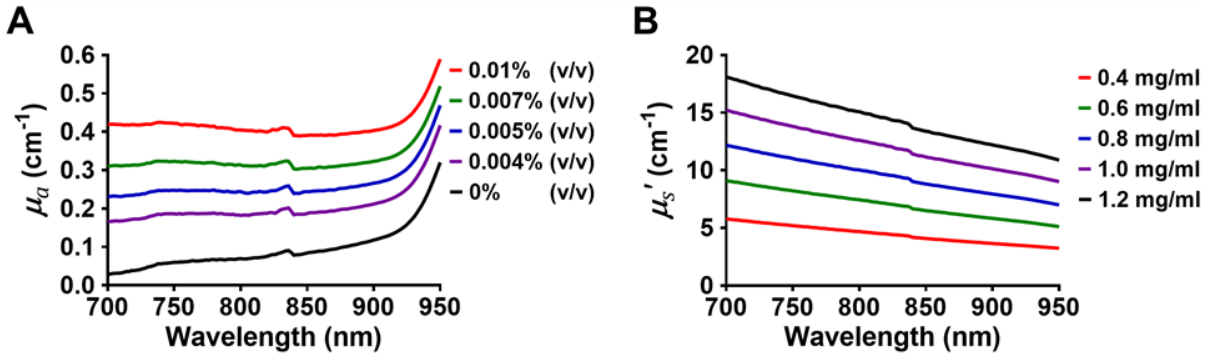

Figure 6. 5 TMM optical properties. PAA (A) and (B) spectra as a function of India ink and TiO_2 concentration, respectively. Discontinuities at 840 nm are due to spectrophotometer switching between visible and near-infrared detectors and slits.

6.3.2 Image Quality

Resolution phantom results with the three PAI systems are shown in **Error! Reference s ource not found.**. Field of view varies between systems due to differences in transducer standoff distance from the phantom surface, as well as acoustic receive data sampling limitations. Axial and lateral FWHM measurements were generally constant with target depth, indicating proper image reconstruction and focusing (Figure 6D and 6E). FWHM values increased and became noisy for deeper targets, which is due to loss of contrast. As shown in Figure 6D, axial resolution improved with increasing transducer center frequency (and thus bandwidth), with depth-averaged values of 0.320 mm (custom system, 7 MHz), 0.245 mm (AcousticX, 10 MHz), and 0.148 mm (Vevo, 15 MHz). This trend is expected because axial resolution is primarily determined by transducer bandwidth [262].

Unexpectedly, the opposite trend was observed for lateral FWHM measurements, with lateral FWHM increasing with transducer center frequency (Figure 6H). Lateral resolution will generally depend on acoustic aperture length and wavelength as well as adequate focusing settings, such as optimal selection of reconstruction speed of sound. Per our imaging protocol, reconstruction speed of sound was locked at 1,540 m/s for consistency, rather than allowing user adjustment during testing. However, the measured lateral FWHM for the Vevo LZ201 transducer of 0.52-0.81 mm was consistent with our previous measurements using a line-pair target (0.59-0.75 mm), indicating good agreement between point spread function and bar chart approaches [107, 293]. The higher acoustic scattering of PAA at high frequencies may have also affected resolution performance. Finally, the 100 μm-thick plastic acoustic window is on the order of the Vevo system's axial resolution and may have caused focusing aberrations. Reflections due to this membrane are also present in the AcousticX and Vevo images because they operate with a standoff distance (unlike the custom system).

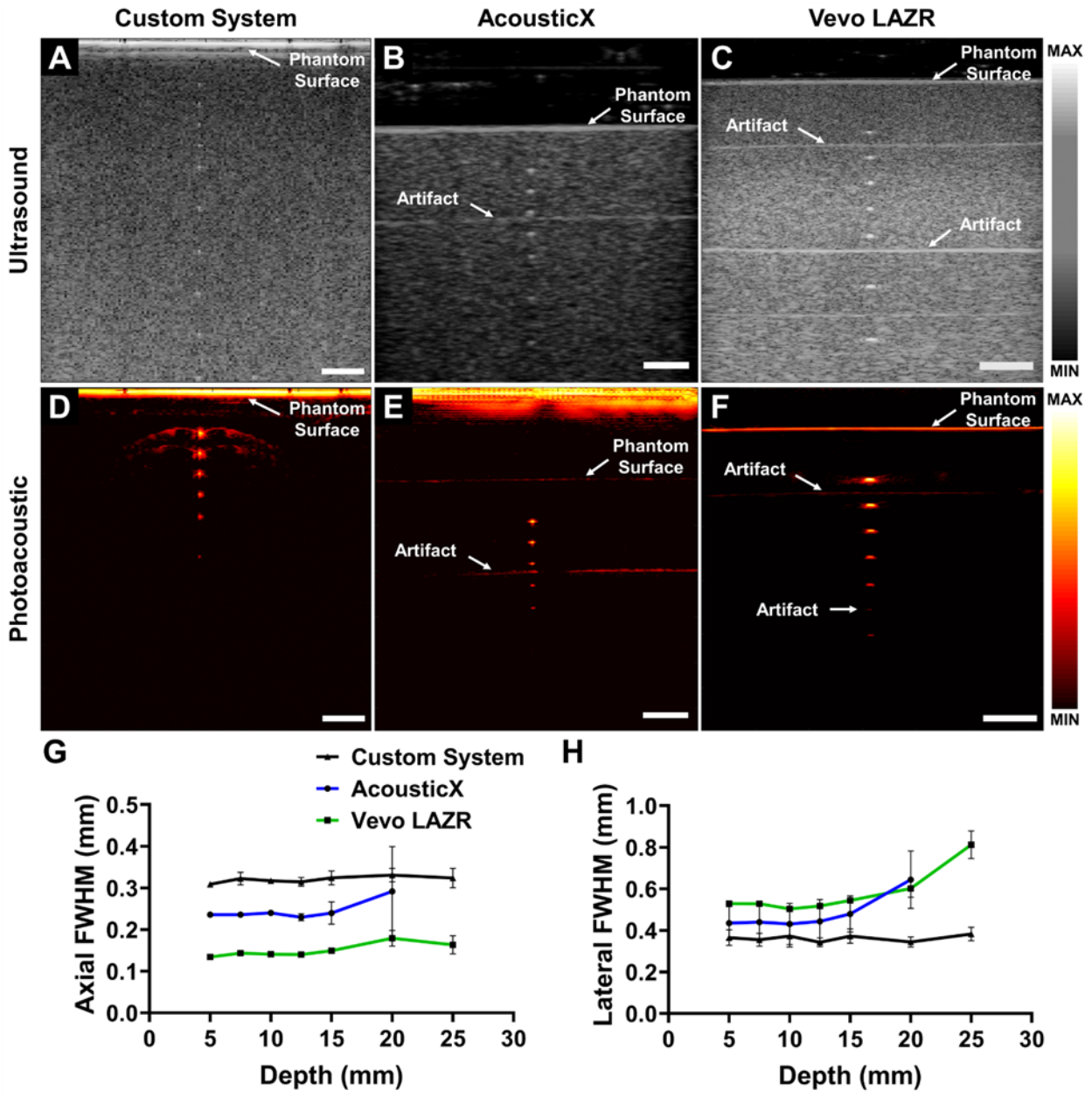

Figure 6. 6 Representative ultrasound and photoacoustic images of the resolution phantom using the custom system (A, D), AcousticX (B, E), and Vevo LAZR (C, F). Measured axial (G) and lateral (H) FWHM vs. depth for each system. Scale bars = 5 mm. Display dynamic range: custom system (US = 80 dB, PAI = 40 dB), AcousticX (US = 70 dB, PAI = 35 dB), Vevo LAZR (US = 70 dB, PAI = 45 dB).

Representative images of the penetration phantom for each PAI system and target absorption level are shown in **Error! Reference source not found.**. These images as shown are o ptimized for image quality analysis, not human readability, which explains the stronger

background and apparent lower image contrast. Generally, clear qualitative differences in imaging depth were observed across systems and target. Several artifacts were present in the images. The custom system produced near-field clutter due to optical absorption at the transducer/phantom interface while the AcousticX and Vevo systems, which operate with the transducer above the phantom surface at some standoff distance, produced horizontal line reflection artifacts. Reflection artifacts were also seen beneath tubes; both artifacts are likely due to photoacoustic signals generated at the transducer surface traveling downward and reflecting off the phantom surface or tubes, which doubles the time of flight and the resulting depth determined by image reconstruction.

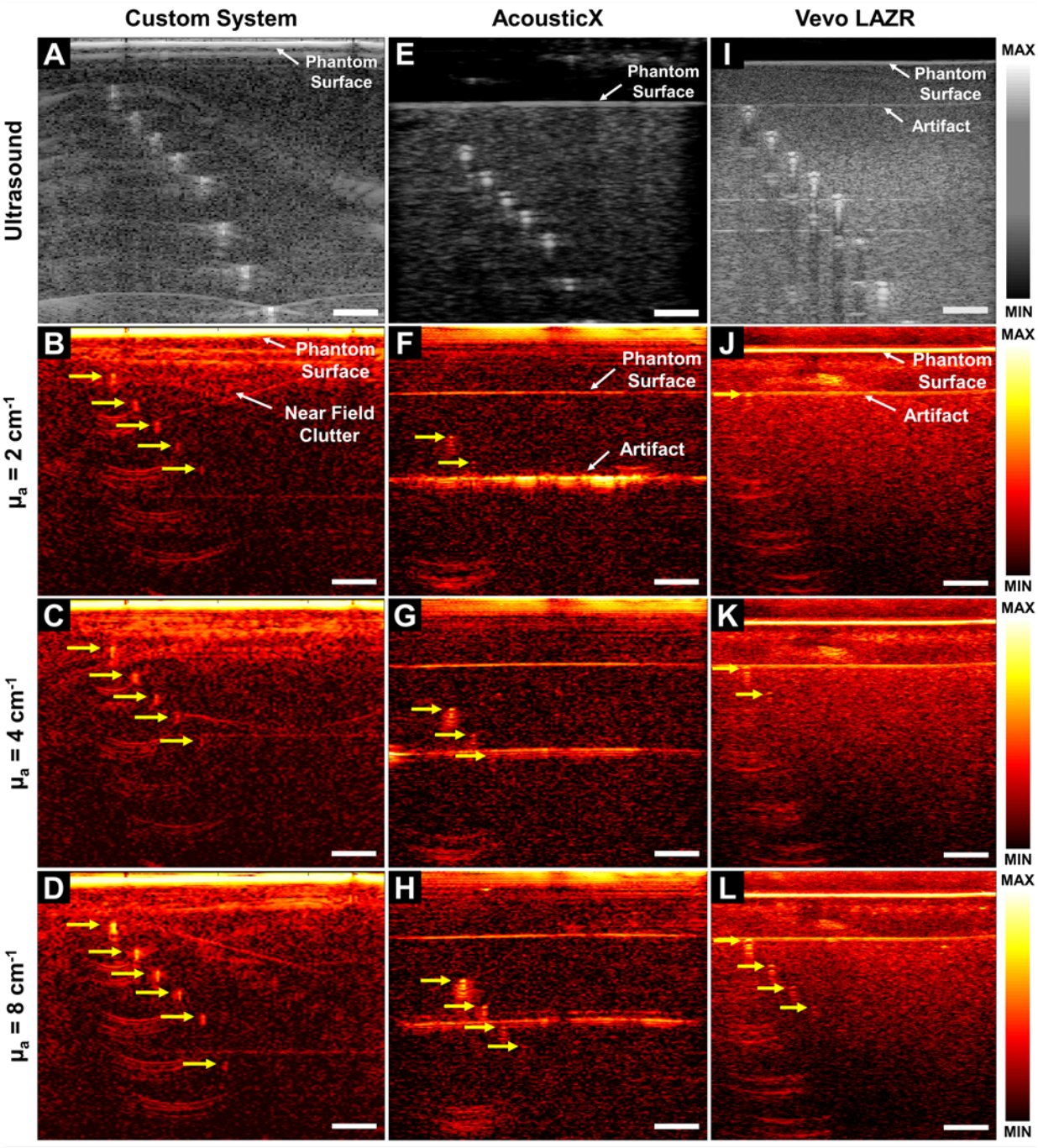

Figure 6. 7 Ultrasound and photoacoustic images of penetration phantom filled with India ink solutions at = 8 cm^{-1}, 4 cm^{-1}, or 2 cm^{-1}, acquired by the custom system (A-D), AcousticX (E-H), and Vevo LAZR (I-L). Yellow arrows denote visible targets. Scale bars = 5 mm. Display dynamic range: custom system (US = 80 dB, PAI = 50 dB), AcousticX (US = 70 dB, PAI = 33 dB), Vevo LAZR (US = 70 dB, PAI = 36 dB).

Image quality metrics computed on linear amplitude images are shown in **Error! R eference source not found.**. was omitted as trends vs. depth were similar to those of CNR but with slightly higher values (per Equation 4). produced a log-linear decrease with depth because, unlike other metrics, it is expressed in dB (and is also the expression of in dB). The custom system had the highest values for all metrics although the curves plateaued for shallow targets as clutter reduced contrast and increased background variation. This pattern may be also be attributed to the in-plane fluence distribution caused by an adjacent beam geometry, which has a somewhat flatter distribution over depths of 0-1 cm, while the other systems may have produced exponential fluence distributions directly beneath the beam [297]. As expected, metrics increased with target , although this increase was not always linear.

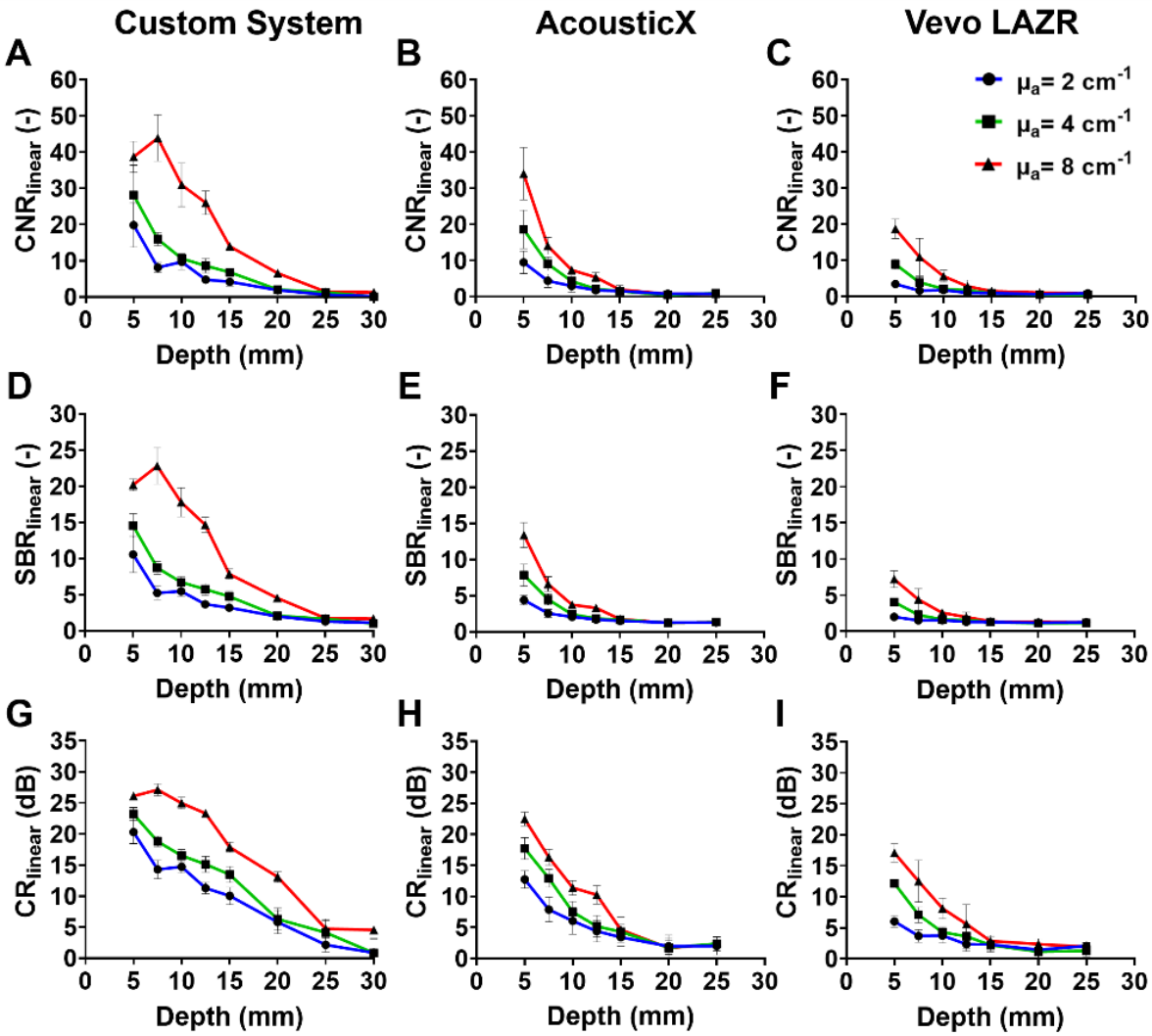

Figure 6. 8 Calculated image quality metrics. (A-C), (D-F), and (G-I) from linear preprocessed images for each system and target . was omitted, as data showed similar trends with slightly higher values than (see Equation 4).

As shown in **Error! Reference source not found.**, choice of display dynamic range s trongly impacted overall image appearance and computed image quality metrics. This is expected based on similar effects in ultrasound image quality assessment, and optimal adjustment of display settings clearly should impact image quality. Qualitative inspection showed target detectability generally increased with decreasing display dynamic range especially for deeper targets. As display dynamic range decreased, and approached zero due to background thresholding, thus causing and to increase (approaching infinity). Following standardized

ultrasound test method recommendations, we attempted to minimize this effect by selecting image display settings in subsequent analyses such that the background was still visible [274, 295]. The sensitivity of and to display settings may suggest correlation with expected human reader performance, and image quality assessment research has generally focused on metrics that consider background variance such as and [298]. was relatively insensitive to changes in display dynamic range, which implies this metric may be less appropriate for predicting human reader performance.

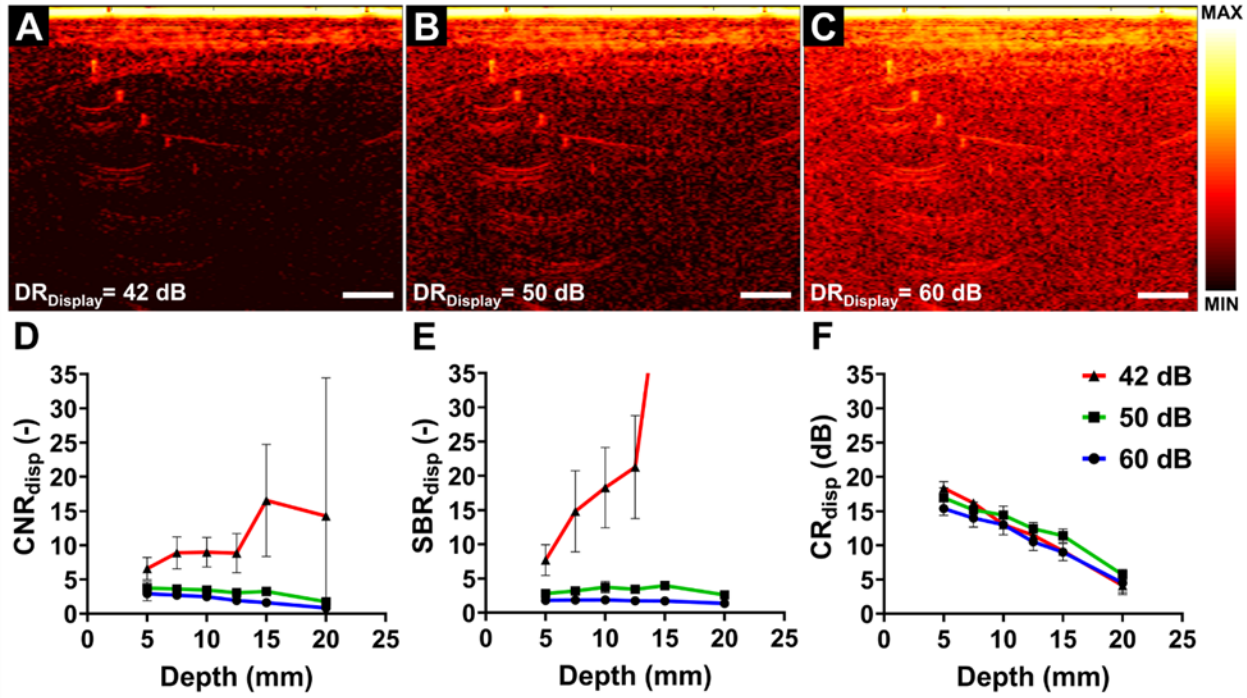

Figure 6. 9 Effect of dynamic ranges on image quality metrics. Custom system images of the penetration phantom with targets at = 4 cm^{-1} using display dynamic ranges of 42 dB (A), 50 dB (B), or 60 dB (C). Scale bars = 5 mm. Effects of display dynamic range on image quality metrics are shown in D-F.Calculated image quality metrics.

Image quality metrics derived from displayed images of the penetration phantom are shown in Figures 10 and 11 (is again omitted per Equation (4)). All metrics were generally lower than those computed from preprocessed images, which is expected as log compression reduces image dynamic range and contrast in order to make the image more readable by a human. and

decreased with depth, although the values began to increase in deep regions where no targets are detectable by inspection (Figure 10). This is due to remaining display thresholding effects as described previously. All metrics approached slightly higher asymptotes with depth than expected (ideally, CNR approaches zero and SBR approaches one). This may be due to the 50%-amplitude target ROI mask selection method, which will generally increase measured target amplitude above background even without a target present. Interestingly, the custom system produced relatively constant and over most detectable targets. This is likely due to higher background amplitude and variation in shallow regions, while the lower amplitude of deeper targets was offset by lower background amplitude and variation in deeper regions.

Of the various image quality metrics computed for displayed images, was found to correlate best with maximum imaging depth (deepest detectable target) as determined by image inspection (**Error! Reference source not found.**) with an interpolated detection threshold of ~4-6 dB. Maximum imaging depth was highest for the custom system, followed by the AcousticX, then Vevo LAZR. These differences in performance are likely due to different optical and acoustic device design parameters. The custom and Vevo systems use high-energy OPOs to achieve much higher radiant exposures than the AcousticX. The AcousticX system produces a much lower radiant exposure over a larger beam area, but averages acquisitions at a higher pulse repetition rate [107]. However, this approach may be limited by the minimum detectable pressure produced by a single optical pulse. Transducer parameters may also significantly contribute to observed differences in performance. A strong inverse correlation was observed between maximum imaging depth and transducer center frequency. This may be due to lower phantom at lower frequencies, as well as target size-dependency of photoacoustic signal amplitude and frequency content. Another possibility is that differences in transducer elevational focusing contribute different out-of-plane signal contributions along the cylindrical targets, which can modify the total signal received. Unfortunately, it was not possible to use transducers with identical parameters across all three systems.

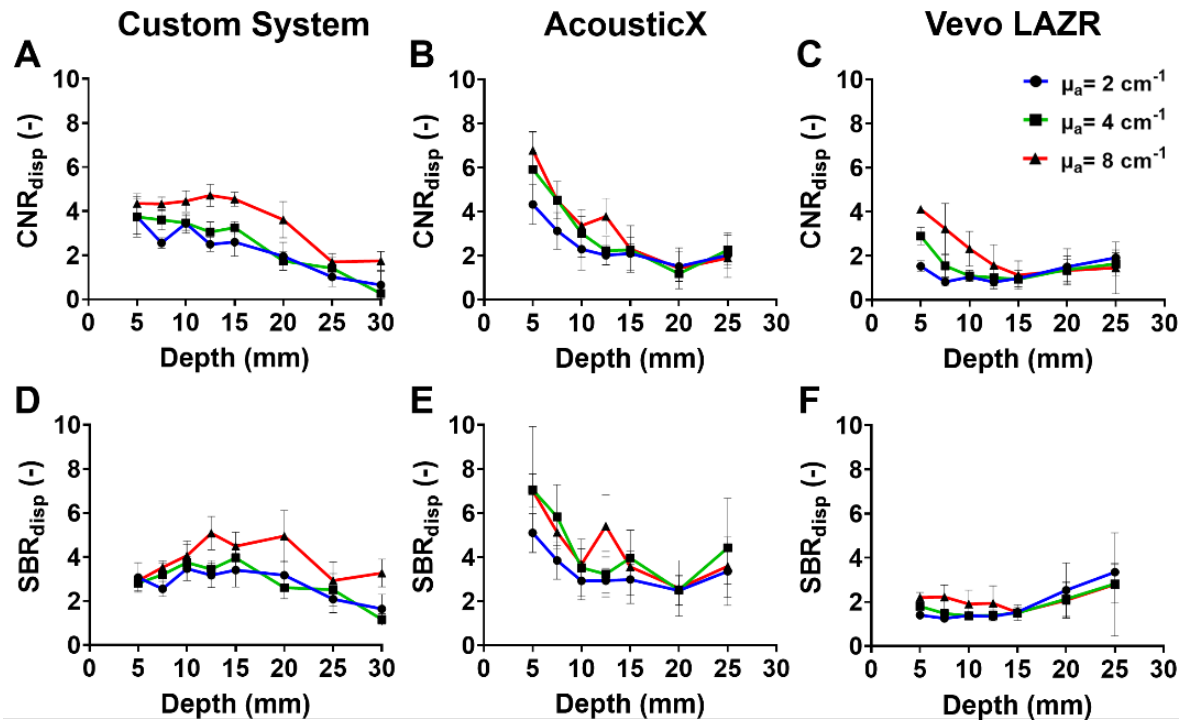

Figure 6. 10 Computed quality metrics for displayed images. (A-C) and (D-F) for the three imaging systems in the penetration phantom at each target absorption level. was omitted, as data showed similar trends with slightly higher values than (see Equation 4).

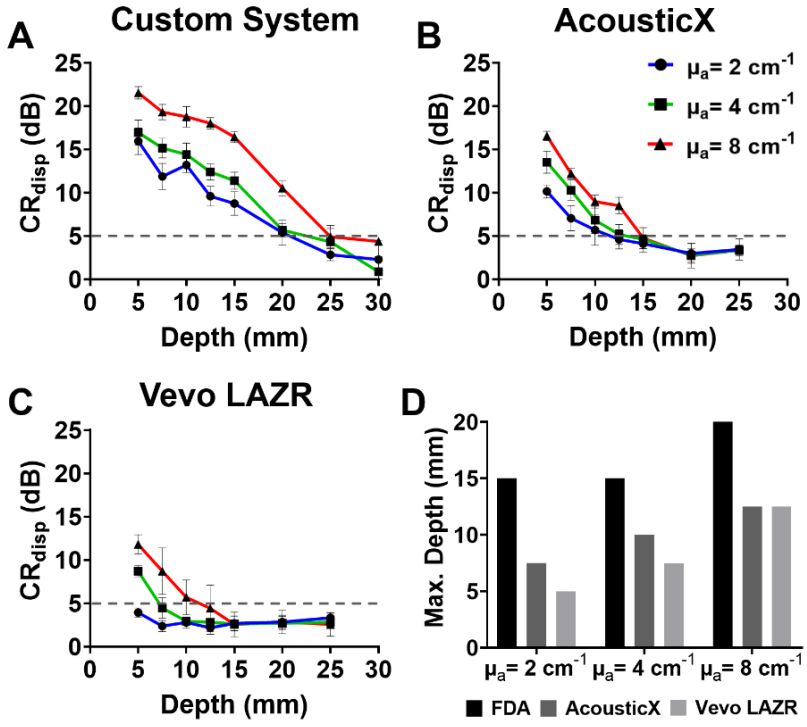

Figure 6. 11 vs. depth and target in the penetration phantom for the custom system (A), AcousticX (B), and Vevo LAZR (C). Max. imaging depth vs. target is shown in (D).

6.4 Discussion

In this study, we developed and characterized a PAA hydrogel-based TMM with stable, widely tunable optical and acoustic properties similar to reported values for soft tissue. We then constructed PAA phantoms suitable for evaluating image quality of PAI systems and that were sufficiently robust for transport. We found that PAA optical and acoustic properties were stable over time and that well-sealed imaging phantoms showed no qualitative signs of desiccation or damage after 6 months of storage at room temperature. This is consistent with the reported service life for Zerdine® hydrogel phantoms of several years [299]. The advantages of PAA hydrogels compared to other available TMMs for PAI include ease of preparation, better mechanical strength/stiffness than common hydrogel-based TMMs, broad dopant compatibility of water, lower preparation temperatures, and lower viscosity during formulation. The disadvantages of PAA include faster dopant settling due to low viscosity, requirements for well-sealed housings to prevent desiccation, reduced gel quality of very high-concentration formulations, and lower mechanical strength than nonaqueous materials such as PVCP and gel wax. Also, while our acoustic characterization data showed low spatial variation (Figure 3), some heterogeneity might still exist in imaging phantoms [253]. These trade-offs should be carefully considered in selecting TMMs for a given phantom design and application.

Our experimental measurements demonstrated utility of these phantoms for evaluating image quality. Phantom testing of three PAI systems indicated a performance trade-off between spatial resolution and target contrast/imaging depth, which is consistent with our previous phantom-based device comparison study [262]. The purpose of this study was not to rank performance of these PAI devices, as each system is intended for different applications and thus has different performance requirements and design specifications. Rather, this study aimed to demonstrate that the developed TMM and phantoms are suitable for evaluating PAI systems with widely differing design parameters. Additionally, our intent was to highlight the benefit of phantom-based test methods for objective, quantitative, and reproducible characterization of device

performance. Phantom-based performance test methods can provide data that illustrates performance trade-offs, elucidates device design consequences, and may help establish performance expectations. Such information can be used to further optimize the design of device hardware or image processing algorithms for a particular application during device development.

Finally, we assessed the suitability of several image quality metrics (SNR, CNR, SBR, and CR) for PAI. We evaluated image quality of both preprocessed linear amplitude images and displayed images, leveraging applicable guidelines from ultrasound standards. Preprocessed image quality is particularly important in PAI as these data preserve linearity of amplitude vs. optical energy deposition and are typically used for quantitative imaging approaches such as oximetry. However, while we could access pre-processed image data for these systems, this may not be true for every user and system. It was thus important to select image quality metrics that yield meaningful insights into performance for images as displayed to a human reader. Test results suggested that CR may correlate best with maximum imaging depth. However, CR may not provide a comprehensive description of image quality under all conditions, for instance in the presence of high, variable background due to clutter or other nearby anatomical features. In such cases, target detectability may be more holistically characterized by noise-based metrics such as CNR, which unlike CR showed sensitivity to changes in image display settings that were qualitatively perceived to modify target detectability. Optimal selection and application of image quality metrics for evaluating photoacoustic images may depend on image content and the intended imaging task or application. Given the current absence of established community consensus on image quality metric selection, it may be most appropriate to evaluate a set of metrics including both CR and CNR. Performance assessment should include analysis of linear images in addition to displayed images.

6.5 Conclusions

In conclusion, the PAA-based phantom we developed in this study is stable, robust, and tunable over a range of tissue-relevant optical and acoustic properties. We demonstrated utility of PAA phantoms for image quality assessment of three linear-array PAI systems. The methods proposed here will support much-needed advancements in PAI device design, optimization, and performance assessment. These methods will aid development of standardized PAI test methods that will ultimately facilitate clinical translation of this technology.

Chapter 6, in full, is a reprint of the material as it appears in *Photoacoustics*, 22, p.100245. Ali Hariri, Jorge Palma Chavez, Keith A. Wear, T. Joshua Pfefer, Jesse V. Jokerst, William C. Vogt. The dissertation author was the primary investigator and author of this paper.

References

1. Hu, S.; Maslov, K.; Wang, L. V., Three-dimensional optical-resolution photoacoustic microscopy. *JoVE (Journal of Visualized Experiments)* **2011,** (51), e2729-e2729.

2. Tavakolian, P.; Kosik, I.; Chamson-Reig, A.; Lawrence, K. S.; Carson, J. J. In *Potential for photoacoustic imaging of the neonatal brain*, SPIE BiOS, International Society for Optics and Photonics: 2013; pp 858147-858147-6.

3. Zhang, H. F.; Puliafito, C. A.; Jiao, S., Photoacoustic ophthalmoscopy for in vivo retinal imaging: current status and prospects. *Ophthalmic Surgery, Lasers and Imaging Retina* **2011,** *42* (4), S106-S115.

4. Upputuri, P. K.; Pramanik, M., Performance characterization of low-cost, high-speed, portable pulsed laser diode photoacoustic tomography (PLD-PAT) system. *Biomedical optics express* **2015,** *6* (10), 4118-4129.

5. Allen, T. J.; Beard, P. C., Pulsed near-infrared laser diode excitation system for biomedical photoacoustic imaging. *Optics letters* **2006,** *31* (23), 3462-3464.

6. Kolkman, R. G.; Steenbergen, W.; van Leeuwen, T. G., In vivo photoacoustic imaging of blood vessels with a pulsed laser diode. *Lasers in medical science* **2006,** *21* (3), 134-139.

7. Wang, L. V.; Hu, S., Photoacoustic tomography: in vivo imaging from organelles to organs. *Science* **2012,** *335* (6075), 1458-1462.

8. Xie, Z.; Roberts, W.; Carson, P.; Liu, X.; Tao, C.; Wang, X., Evaluation of bladder microvasculature with high-resolution photoacoustic imaging. *Optics letters* **2011,** *36* (24), 4815-4817.

9. Jiao, S.; Zhang, H., Optical coherence photoacoustic microscopy. Google Patents: 2012.

10. Bitton, R.; Zemp, R.; Yen, J.; Wang, L. V.; Shung, K. K., A 3-D high-frequency array based 16 channel photoacoustic microscopy system for in vivo micro-vascular imaging. *Medical Imaging, IEEE Transactions on* **2009,** *28* (8), 1190-1197.

11. Oladipupo, S. S.; Hu, S.; Santeford, A. C.; Yao, J.; Kovalski, J. R.; Shohet, R. V.; Maslov, K.; Wang, L. V.; Arbeit, J. M., Conditional HIF-1 induction produces multistage neovascularization with stage-specific sensitivity to VEGFR inhibitors and myeloid cell independence. *Blood* **2011,** *117* (15), 4142-4153.

12. Oladipupo, S.; Hu, S.; Kovalski, J.; Yao, J.; Santeford, A.; Sohn, R. E.; Shohet, R.; Maslov, K.; Wang, L. V.; Arbeit, J. M., VEGF is essential for hypoxia-inducible factor-mediated neovascularization but dispensable for endothelial sprouting. *Proceedings of the National Academy of Sciences* **2011,** *108* (32), 13264-13269.

13. Li, M.-L.; Oh, J.-T.; Xie, X.; Ku, G.; Wang, W.; Li, C.; Lungu, G.; Stoica, G.; Wang, L. V., Simultaneous molecular and hypoxia imaging of brain tumors in vivo using spectroscopic photoacoustic tomography. *Proceedings of the IEEE* **2008,** *96* (3), 481-489.

14. Staley, J.; Grogan, P.; Samadi, A. K.; Cui, H.; Cohen, M. S.; Yang, X., Growth of melanoma brain tumors monitored by photoacoustic microscopy. *Journal of biomedical optics* **2010,** *15* (4), 040510-040510-3.

15. Liao, L.-D.; Li, M.-L.; Lai, H.-Y.; Shih, Y.-Y. I.; Lo, Y.-C.; Tsang, S.; Chao, P. C.-P.; Lin, C.-T.; Jaw, F.-S.; Chen, Y.-Y., Imaging brain hemodynamic changes during rat forepaw electrical stimulation using functional photoacoustic microscopy. *Neuroimage* **2010,** *52* (2), 562-570.

16. Tsytsarev, V.; Hu, S.; Yao, J.; Maslov, K.; Barbour, D. L.; Wang, L. V., Photoacoustic microscopy of microvascular responses to cortical electrical stimulation. *Journal of biomedical optics* **2011,** *16* (7), 076002-076002-6.

17. Hu, S.; Rao, B.; Maslov, K.; Wang, L. V., Label-free photoacoustic ophthalmic angiography. *Optics letters* **2010,** *35* (1), 1-3.

18. Silverman, R. H.; Kong, F.; Chen, Y.; Lloyd, H. O.; Kim, H. H.; Cannata, J. M.; Shung, K. K.; Coleman, D. J., High-resolution photoacoustic imaging of ocular tissues. *Ultrasound in medicine & biology* **2010,** *36* (5), 733-742.

19. Zhang, H. F.; Maslov, K.; Li, M.-L.; Stoica, G.; Wang, L. V., In vivo volumetric imaging of subcutaneous microvasculature by photoacoustic microscopy. *Optics Express* **2006,** *14* (20), 9317-9323.

20. Favazza, C.; Maslov, K.; Cornelius, L.; Wang, L. V. In *In vivo functional human imaging using photoacoustic microscopy: response to ischemic and thermal stimuli*, BiOS, International Society for Optics and Photonics: 2010; pp 75640Z-75640Z-6.

21. Favazza, C. P.; Cornelius, L. A.; Wang, L. V., In vivo functional photoacoustic microscopy of cutaneous microvasculature in human skin. *Journal of biomedical optics* **2011,** *16* (2), 026004-026004-5.

22. Song, L.; Maslov, K.; Shung, K. K.; Wang, L. V., Ultrasound-array-based real-time photoacoustic microscopy of human pulsatile dynamics in vivo. *Journal of biomedical optics* **2010,** *15* (2), 021303-021303-4.

23. Yang, J.-M.; Chen, R.; Favazza, C.; Yao, J.; Zhou, Q.; Shung, K. K.; Wang, L. V. In *A 2.5-mm outer diameter photoacoustic endoscopic mini-probe based on a highly sensitive PMN-PT ultrasonic transducer*, SPIE BiOS, International Society for Optics and Photonics: 2012; pp 82233M-82233M-6.

24. Yang, J.-M.; Favazza, C.; Chen, R.; Yao, J.; Cai, X.; Maslov, K.; Zhou, Q.; Shung, K. K.; Wang, L. V. In *Toward dual-wavelength functional photoacoustic endoscopy: laser and peripheral optical systems development*, SPIE BiOS, International Society for Optics and Photonics: 2012; pp 822316-822316-7.

25. Rowland, K. J.; Yao, J.; Wang, L.; Erwin, C. R.; Maslov, K. I.; Wang, L. V.; Warner, B. W., Immediate alterations in intestinal oxygen saturation and blood flow after massive small bowel resection as measured by photoacoustic microscopy. *Journal of pediatric surgery* **2012,** *47* (6), 1143-1149.

26. Taruttis, A.; Herzog, E.; Razansky, D.; Ntziachristos, V., Real-time imaging of cardiovascular dynamics and circulating gold nanorods with multispectral optoacoustic tomography. *Optics Express* **2010,** *18* (19), 19592-19602.

27. Zemp, R.; Song, L.; Bitton, R.; Shung, K.; Wang, L., Realtime photoacoustic microscopy of murine cardiovascular dynamics. *Optics express* **2008,** *16* (22), 18551-18556.

28. Park, S.; Lee, C.; Kim, J.; Kim, C., Acoustic resolution photoacoustic microscopy. *Biomedical Engineering Letters* **2014,** *4* (3), 213-222.

29. Hu, S.; Maslov, K.; Wang, L. V., Second-generation optical-resolution photoacoustic microscopy with improved sensitivity and speed. *Optics letters* **2011,** *36* (7), 1134-1136.

30. Zhang, C.; Maslov, K.; Wang, L. V., Subwavelength-resolution label-free photoacoustic microscopy of optical absorption in vivo. *Optics letters* **2010,** *35* (19), 3195-3197.

31. Yuan, Y.; Yang, S.; Xing, D., Optical-resolution photoacoustic microscopy based on two-dimensional scanning galvanometer. *Applied Physics Letters* **2012,** *100* (2), 023702.

32. Song, W.; Zheng, W.; Liu, R.; Lin, R.; Huang, H.; Gong, X.; Yang, S.; Zhang, R.; Song, L., Reflection-mode in vivo photoacoustic microscopy with subwavelength lateral resolution. *Biomedical optics express* **2014,** *5* (12), 4235-4241.

33. Chen, J.; Lin, R.; Wang, H.; Meng, J.; Zheng, H.; Song, L., Blind-deconvolution optical-resolution photoacoustic microscopy in vivo. *Optics express* **2013,** *21* (6), 7316-7327.

34. Zhang, C.; Maslov, K.; Hu, S.; Chen, R.; Zhou, Q.; Shung, K. K.; Wang, L. V., Reflection-mode submicron-resolution in vivo photoacoustic microscopy. *Journal of biomedical optics* **2012,** *17* (2), 0205011-0205014.

35. Song, K. H.; Wang, L. V., Deep reflection-mode photoacoustic imaging of biological tissue. *Journal of biomedical optics* **2007,** *12* (6), 060503-060503-3.

36. Kolkman, R. G.; Steenbergen, W.; van Leeuwen, T. G., Reflection mode photoacoustic measurement of speed of sound. *Optics express* **2007,** *15* (6), 3291-3300.

37. Zeng, L.; Liu, G.; Yang, D.; Ji, X., 3D-visual laser-diode-based photoacoustic imaging. *Optics express* **2012,** *20* (2), 1237-1246.

38. LeBoulluec, P.; Liu, H.; Yuan, B., A cost-efficient frequency-domain photoacoustic imaging system. *American journal of physics* **2013,** *81* (9), 712-717.

39. Wang, T.; Nandy, S.; Salehi, H. S.; Kumavor, P. D.; Zhu, Q., A low-cost photoacoustic microscopy system with a laser diode excitation. *Biomedical optics express* **2014,** *5* (9), 3053-3058.

40. Xu, M.; Wang, L. V., Photoacoustic imaging in biomedicine. *Review of scientific instruments* **2006,** *77* (4), 041101.

41. Wang, L. V., Multiscale photoacoustic microscopy and computed tomography. *Nature photonics* **2009,** *3* (9), 503-509.

42. Karpiouk, A. B.; Wang, B.; Emelianov, S. Y., Development of a catheter for combined intravascular ultrasound and photoacoustic imaging. *Review of Scientific Instruments* **2010,** *81* (1), 014901.

43. Kolkman, R. G.; Brands, P. J.; Steenbergen, W.; van Leeuwen, T. G., Real-time in vivo photoacoustic and ultrasound imaging. *Journal of biomedical optics* **2008,** *13* (5), 050510-050510-3.

44. Neuschmelting, V.; Burton, N. C.; Lockau, H.; Urich, A.; Harmsen, S.; Ntziachristos, V.; Kircher, M. F., Performance of a Multispectral Optoacoustic Tomography (MSOT) System equipped with 2D vs. 3D handheld probes for potential clinical translation. *Photoacoustics* **2016,** *4* (1), 1-10.

45. Jeon, M.; Song, W.; Huynh, E.; Kim, J.; Kim, J.; Helfield, B. L.; Leung, B. Y.; Goertz, D. E.; Zheng, G.; Oh, J., Methylene blue microbubbles as a model dual-modality contrast agent for ultrasound and activatable photoacoustic imaging. *Journal of biomedical optics* **2014,** *19* (1), 016005-016005.

46. Pu, K.; Shuhendler, A. J.; Jokerst, J. V.; Mei, J.; Gambhir, S. S.; Bao, Z.; Rao, J., Semiconducting polymer nanoparticles as photoacoustic molecular imaging probes in living mice. *Nature nanotechnology* **2014,** *9* (3), 233-239.

47. Weber, J.; Beard, P. C.; Bohndiek, S. E., Contrast agents for molecular photoacoustic imaging. *Nature Methods* **2016,** *13* (8), 639-650.

48. Yin, C.; Zhen, X.; Fan, Q.; Huang, W.; Pu, K., Degradable Semiconducting Oligomer Amphiphile for Ratiometric Photoacoustic Imaging of Hypochlorite. *ACS nano* **2017**.

49. Huynh, E.; Lovell, J. F.; Helfield, B. L.; Jeon, M.; Kim, C.; Goertz, D. E.; Wilson, B. C.; Zheng, G., Porphyrin shell microbubbles with intrinsic ultrasound and photoacoustic properties. *Journal of the American Chemical Society* **2012,** *134* (40), 16464-16467.

50. Valluru, K. S.; Wilson, K. E.; Willmann, J. K., Photoacoustic Imaging in oncology: translational preclinical and early clinical experience. *Radiology* **2016,** *280* (2), 332-349.

51. Song, W.; Wei, Q.; Liu, W.; Liu, T.; Yi, J.; Sheibani, N.; Fawzi, A. A.; Linsenmeier, R. A.; Jiao, S.; Zhang, H. F., A combined method to quantify the retinal metabolic rate of oxygen using photoacoustic ophthalmoscopy and optical coherence tomography. *Scientific reports* **2014,** *4*, 6525.

52. de La Zerda, A.; Paulus, Y. M.; Teed, R.; Bodapati, S.; Dollberg, Y.; Khuri-Yakub, B. T.; Blumenkranz, M. S.; Moshfeghi, D. M.; Gambhir, S. S., Photoacoustic ocular imaging. *Optics letters* **2010,** *35* (3), 270-272.

53. Nasiriavanaki, M.; Xia, J.; Wan, H.; Bauer, A. Q.; Culver, J. P.; Wang, L. V., High-resolution photoacoustic tomography of resting-state functional connectivity in the mouse brain. *Proceedings of the National Academy of Sciences* **2014,** *111* (1), 21-26.

54. Sampathkumar, A.; Silverman, R. H. In *Non-contact photoacoustic characterization of retinal vasculature for brain-injury assessment*, Ultrasonics Symposium (IUS), 2014 IEEE International, IEEE: 2014; pp 843-845.

55. Pang, G. A.; Bay, E.; DEÁN-BEN, X.; Razansky, D., Three-Dimensional Optoacoustic Monitoring of Lesion Formation in Real Time During Radiofrequency Catheter Ablation. *Journal of cardiovascular electrophysiology* **2015,** *26* (3), 339-345.

56. Zeng, L.; Liu, G.; Yang, D.; Ji, X., Portable optical-resolution photoacoustic microscopy with a pulsed laser diode excitation. *Applied physics letters* **2013,** *102* (5), 053704.

57. Upputuri, P. K.; Pramanik, M., Pulsed laser diode based optoacoustic imaging of biological tissues. *Biomedical Physics & Engineering Express* **2015,** *1* (4), 045010.

58. Daoudi, K.; Van Den Berg, P.; Rabot, O.; Kohl, A.; Tisserand, S.; Brands, P.; Steenbergen, W., Handheld probe integrating laser diode and ultrasound transducer array for ultrasound/photoacoustic dual modality imaging. *Optics express* **2014,** *22* (21), 26365-26374.

59. Hansen, R. S. In *Using high-power light emitting diodes for photoacoustic imaging*, SPIE Medical Imaging, International Society for Optics and Photonics: 2011; pp 79680A-79680A-6.

60. Allen, T. J.; Beard, P. C., High power visible light emitting diodes as pulsed excitation sources for biomedical photoacoustics. *Biomedical optics express* **2016,** *7* (4), 1260-1270.

61. Adachi, Y.; Hoshimiya, T., Photoacoustic imaging with multiple-wavelength light-emitting diodes. *Japanese Journal of Applied Physics* **2013,** *52* (7S), 07HB06.

62. Puri, N., Comparative study of diode laser versus neodymium-yttrium aluminum: garnet laser versus intense pulsed light for the treatment of hirsutism. *Journal of cutaneous and aesthetic surgery* **2015,** *8* (2), 97.

63. Zhang, Y.; Jeon, M.; Rich, L. J.; Hong, H.; Geng, J.; Zhang, Y.; Shi, S.; Barnhart, T. E.; Alexandridis, P.; Huizinga, J. D., Non-invasive multimodal functional imaging of the intestine with frozen micellar naphthalocyanines. *Nature nanotechnology* **2014,** *9* (8), 631-638.

64. Kircher, M. F.; De La Zerda, A.; Jokerst, J. V.; Zavaleta, C. L.; Kempen, P. J.; Mittra, E.; Pitter, K.; Huang, R.; Campos, C.; Habte, F., A brain tumor molecular imaging strategy using a new triple-modality MRI-photoacoustic-Raman nanoparticle. *Nature medicine* **2012,** *18* (5), 829-834.

65. Wang, J.; Chen, F.; Arconada-Alvarez, S. J.; Hartanto, J.; Yap, L.-P.; Park, R.; Wang, F.; Vorobyova, I.; Dagliyan, G.; Conti, P. S., A Nanoscale Tool for Photoacoustic-based Measurements of Clotting Time and Therapeutic Drug Monitoring of Heparin. *Nano Letters* **2016,** *16* (10), 6265-6271.

66. Cash, K. J.; Li, C.; Xia, J.; Wang, L. V.; Clark, H. A., Optical drug monitoring: photoacoustic imaging of nanosensors to monitor therapeutic lithium in vivo. *ACS nano* **2015,** *9* (2), 1692.

67. Hai, P.; Zhou, Y.; Zhang, R.; Ma, J.; Li, Y.; Shao, J.-Y.; Wang, L. V., Label-free high-throughput detection and quantification of circulating melanoma tumor cell clusters by linear-array-based photoacoustic tomography. *Journal of biomedical optics* **2017,** *22* (4), 041004-041004.

68. Viator, J. A.; Gupta, S.; Goldschmidt, B. S.; Bhattacharyya, K.; Kannan, R.; Shukla, R.; Dale, P. S.; Boote, E.; Katti, K., Gold nanoparticle mediated detection of prostate cancer cells

using photoacoustic flowmetry with optical reflectance. *Journal of biomedical nanotechnology* **2010,** *6* (2), 187-191.

69. O'Brien, C. M.; Rood, K.; Sengupta, S.; Gupta, S. K.; DeSouza, T.; Cook, A.; Viator, J. A., Detection and isolation of circulating melanoma cells using photoacoustic flowmetry. *Journal of visualized experiments: JoVE* **2011,** (57).

70. Mienkina, M. P.; Eder, A.; Schmitz, G.; Friedrich, C.-S.; Gerhardt, N. C.; Hofmann, M. R. In *Simulation study of photoacoustic coded excitation using Golay codes*, Ultrasonics Symposium, 2008. IUS 2008. IEEE, IEEE: 2008; pp 1242-1245.

71. Sun, M.; Feng, N.; Shen, Y.; Shen, X.; Li, J., Photoacoustic signals denoising based on empirical mode decomposition and energy-window method. *Advances in Adaptive Data Analysis* **2012,** *4* (01n02), 1250004.

72. Bell, M. A. L.; Guo, X.; Kang, H. J.; Boctor, E. In *Improved contrast in laser-diode-based photoacoustic images with short-lag spatial coherence beamforming*, Ultrasonics Symposium (IUS), 2014 IEEE International, IEEE: 2014; pp 37-40.

73. Ermilov, S. A.; Khamapirad, T.; Conjusteau, A.; Leonard, M. H.; Lacewell, R.; Mehta, K.; Miller, T.; Oraevsky, A. A., Laser optoacoustic imaging system for detection of breast cancer. *Journal of biomedical optics* **2009,** *14* (2), 024007-024007-14.

74. Synnevag, J.; Austeng, A.; Holm, S., Adaptive beamforming applied to medical ultrasound imaging. *IEEE Transactions on Ultrasonics Ferroelectrics and Frequency Control* **2007,** *54* (8), 1606.

75. Köstli, K. P.; Beard, P. C., Two-dimensional photoacoustic imaging by use of Fourier-transform image reconstruction and a detector with an anisotropic response. *Applied optics* **2003,** *42* (10), 1899-1908.

76. Rasband, W., ImageJ. US National Institutes of Health, Bethesda, MD. 1997.

77. Wang, L. V.; Wu, H.-i., *Biomedical optics: principles and imaging*. John Wiley & Sons: 2012.

78. Niederhauser, J. J.; Jaeger, M.; Lemor, R.; Weber, P.; Frenz, M., Combined ultrasound and optoacoustic system for real-time high-contrast vascular imaging in vivo. *IEEE transactions on medical imaging* **2005,** *24* (4), 436-440.

79. Kim, C.; Erpelding, T. N.; Jankovic, L.; Pashley, M. D.; Wang, L. V., Deeply penetrating in vivo photoacoustic imaging using a clinical ultrasound array system. *Biomedical optics express* **2010,** *1* (1), 278-284.

80. Zhou, Y.; Wang, D.; Zhang, Y.; Chitgupi, U.; Geng, J.; Wang, Y.; Zhang, Y.; Cook, T. R.; Xia, J.; Lovell, J. F., A phosphorus phthalocyanine formulation with intense absorbance at 1000 nm for deep optical imaging. *Theranostics* **2016,** *6* (5), 688.

81. Luke, G. P.; Yeager, D.; Emelianov, S. Y., Biomedical applications of photoacoustic imaging with exogenous contrast agents. *Annals of biomedical engineering* **2012,** *40* (2), 422-437.

82. Jokerst, J. V.; Thangaraj, M.; Kempen, P. J.; Sinclair, R.; Gambhir, S. S., Photoacoustic imaging of mesenchymal stem cells in living mice via silica-coated gold nanorods. *ACS nano* **2012,** *6* (7), 5920-5930.

83. Nam, S. Y.; Ricles, L. M.; Suggs, L. J.; Emelianov, S. Y., In vivo ultrasound and photoacoustic monitoring of mesenchymal stem cells labeled with gold nanotracers. *PLoS One* **2012,** *7* (5), e37267.

84. Zhang, B.; Sun, X.; Mei, H.; Wang, Y.; Liao, Z.; Chen, J.; Zhang, Q.; Hu, Y.; Pang, Z.; Jiang, X., LDLR-mediated peptide-22-conjugated nanoparticles for dual-targeting therapy of brain glioma. *Biomaterials* **2013,** *34* (36), 9171-9182.

85. Huang, J.; Zhang, H.; Yu, Y.; Chen, Y.; Wang, D.; Zhang, G.; Zhou, G.; Liu, J.; Sun, Z.; Sun, D., Biodegradable self-assembled nanoparticles of poly (d, l-lactide-co-glycolide)/hyaluronic acid block copolymers for target delivery of docetaxel to breast cancer. *Biomaterials* **2014,** *35* (1), 550-566.

86. Beard, P., Biomedical photoacoustic imaging. *Interface focus* **2011,** *1* (4), 602-631.

87. Mantri, Y.; Davidi, B.; Lemaster, J. E.; Hariri, A.; Jokerst, J. V., Iodide-doped Precious Metal Nanoparticles: Measuring Oxidative Stress in vivo via Photoacoustic Imaging. *Nanoscale* **2020**.

88. Wang, L. V., *Photoacoustic imaging and spectroscopy*. CRC press: 2017.

89. Wilson, K.; Homan, K.; Emelianov, S., Biomedical photoacoustics beyond thermal expansion using triggered nanodroplet vaporization for contrast-enhanced imaging. *Nature communications* **2012,** *3* (1), 1-10.

90. Telenkov, S.; Alwi, R.; Mandelis, A.; Worthington, A., Frequency-domain photoacoustic phased array probe for biomedical imaging applications. *Optics letters* **2011,** *36* (23), 4560-4562.

91. Wang, Y.; Xing, D.; Zeng, Y.; Chen, Q., Photoacoustic imaging with deconvolution algorithm. *Physics in Medicine & Biology* **2004,** *49* (14), 3117.

92. Haltmeier, M.; Scherzer, O.; Zangerl, G., A reconstruction algorithm for photoacoustic imaging based on the nonuniform FFT. *IEEE transactions on medical imaging* **2009,** *28* (11), 1727-1735.

93. Mozaffarzadeh, M.; Hariri, A.; Moore, C.; Jokerst, J. V., The double-stage delay-multiply-and-sum image reconstruction method improves imaging quality in a LED-based photoacoustic array scanner. *Photoacoustics* **2018,** *12*, 22-29.

94. Omidi, P.; Zafar, M.; Mozaffarzadeh, M.; Hariri, A.; Haung, X.; Orooji, M.; Nasiriavanaki, M., A novel dictionary-based image reconstruction for photoacoustic computed tomography. *Applied Sciences* **2018,** *8* (9), 1570.

95. Liu, W.; Zhang, H. F., Photoacoustic imaging of the eye: a mini review. *Photoacoustics* **2016,** *4* (3), 112-123.

96. Hariri, A.; Wang, J.; Kim, Y.; Jhunjhunwala, A.; Chao, D. L.; Jokerst, J. V., In vivo photoacoustic imaging of chorioretinal oxygen gradients. *Journal of biomedical optics* **2018,** *23* (3), 036005.

97. Mallidi, S.; Luke, G. P.; Emelianov, S., Photoacoustic imaging in cancer detection, diagnosis, and treatment guidance. *Trends in biotechnology* **2011,** *29* (5), 213-221.

98. Agarwal, A.; Huang, S.; O'donnell, M.; Day, K.; Day, M.; Kotov, N.; Ashkenazi, S., Targeted gold nanorod contrast agent for prostate cancer detection by photoacoustic imaging. *Journal of applied physics* **2007,** *102* (6), 064701.

99. Mehrmohammadi, M.; Joon Yoon, S.; Yeager, D.; Y Emelianov, S., Photoacoustic imaging for cancer detection and staging. *Current molecular imaging* **2013,** *2* (1), 89-105.

100. Zabihian, B.; Weingast, J.; Liu, M.; Zhang, E.; Beard, P.; Pehamberger, H.; Drexler, W.; Hermann, B., In vivo dual-modality photoacoustic and optical coherence tomography imaging of human dermatological pathologies. *Biomedical optics express* **2015,** *6* (9), 3163-3178.

101. Kim, J.; Kim, Y.; Park, B.; Seo, H. M.; Bang, C.; Park, G.; Park, Y.; Rhie, J.; Lee, J.; Kim, C., Multispectral ex vivo photoacoustic imaging of cutaneous melanoma for better selection of the excision margin. *British Journal of Dermatology* **2018,** *179* (3), 780-782.

102. Hariri, A.; Chen, F.; Moore, C.; Jokerst, J. V., Noninvasive staging of pressure ulcers using photoacoustic imaging. *Wound Repair and Regeneration* **2019,** *27* (5), 488-496.

103. Erpelding, T. N.; Kim, C.; Pramanik, M.; Jankovic, L.; Maslov, K.; Guo, Z.; Margenthaler, J. A.; Pashley, M. D.; Wang, L. V., Sentinel lymph nodes in the rat: noninvasive photoacoustic and US imaging with a clinical US system. *Radiology* **2010,** *256* (1), 102-110.

104. Song, L.; Kim, C.; Maslov, K.; Shung, K. K.; Wang, L. V., High-speed dynamic 3D photoacoustic imaging of sentinel lymph node in a murine model using an ultrasound array. *Medical physics* **2009,** *36* (8), 3724-3729.

105. Song, K. H.; Kim, C.; Maslov, K.; Wang, L. V., Noninvasive in vivo spectroscopic nanorod-contrast photoacoustic mapping of sentinel lymph nodes. *European journal of radiology* **2009,** *70* (2), 227-231.

106. Hariri, A.; Fatima, A.; Mohammadian, N.; Mahmoodkalayeh, S.; Ansari, M. A.; Bely, N.; Avanaki, M. R., Development of low-cost photoacoustic imaging systems using very low-energy pulsed laser diodes. *Journal of biomedical optics* **2017,** *22* (7), 075001.

107. Hariri, A.; Lemaster, J.; Wang, J.; Jeevarathinam, A. S.; Chao, D. L.; Jokerst, J. V., The characterization of an economic and portable LED-based photoacoustic imaging system to facilitate molecular imaging. *Photoacoustics* **2018,** *9*, 10-20.

108. Zhu, Y.; Xu, G.; Yuan, J.; Jo, J.; Gandikota, G.; Demirci, H.; Agano, T.; Sato, N.; Shigeta, Y.; Wang, X., Light emitting diodes based photoacoustic imaging and potential clinical applications. *Scientific reports* **2018,** *8* (1), 1-12.

109. Hansen, R. S. In *Using high-power light emitting diodes for photoacoustic imaging*, Medical Imaging 2011: Ultrasonic Imaging, Tomography, and Therapy, International Society for Optics and Photonics: 2011; p 79680A.

110. Wu, Z.; Huang, N. E., A study of the characteristics of white noise using the empirical mode decomposition method. *Proceedings of the Royal Society of London. Series A: Mathematical, Physical and Engineering Sciences* **2004,** *460* (2046), 1597-1611.

111. Wu, Z.; Huang, N. E., Ensemble empirical mode decomposition: a noise-assisted data analysis method. *Advances in adaptive data analysis* **2009,** *1* (01), 1-41.

112. Messer, S. R.; Agzarian, J.; Abbott, D., Optimal wavelet denoising for phonocardiograms. *Microelectronics journal* **2001,** *32* (12), 931-941.

113. Chang, S. G.; Yu, B.; Vetterli, M., Adaptive wavelet thresholding for image denoising and compression. *IEEE transactions on image processing* **2000,** *9* (9), 1532-1546.

114. Sindelar, C. V.; Grigorieff, N., An adaptation of the Wiener filter suitable for analyzing images of isolated single particles. *Journal of structural biology* **2011,** *176* (1), 60-74.

115. Redler, G.; Epel, B.; Halpern, H. J., Principal component analysis enhances SNR for dynamic electron paramagnetic resonance oxygen imaging of cycling hypoxia in vivo. *Magnetic resonance in medicine* **2014,** *71* (1), 440-450.

116. Yoshida, T.; Miyamoto, R.; Takada, M.; Suzuki, K., Adaptive noise canceller. Google Patents: 1995.

117. Manwar, R.; Hosseinzadeh, M.; Hariri, A.; Kratkiewicz, K.; Noei, S.; Avanaki, N.; Mohammad, R., photoacoustic Signal enhancement: towards utilization of Low energy laser diodes in Real-time photoacoustic imaging. *Sensors* **2018,** *18* (10), 3498.

118. Krizhevsky, A.; Sutskever, I.; Hinton, G. E. In *Imagenet classification with deep convolutional neural networks*, Advances in neural information processing systems, 2012; pp 1097-1105.

119. He, K.; Zhang, X.; Ren, S.; Sun, J. In *Deep residual learning for image recognition*, Proceedings of the IEEE conference on computer vision and pattern recognition, 2016; pp 770-778.

120. Arafati, A.; Hu, P.; Finn, J. P.; Rickers, C.; Cheng, A. L.; Jafarkhani, H.; Kheradvar, A., Artificial intelligence in pediatric and adult congenital cardiac MRI: an unmet clinical need. *Cardiovascular diagnosis and therapy* **2019,** *9* (Suppl 2), S310.

121. Arafati, A. Segmentation and Tracking of Echocardiograms Using Deep Learning Algorithms. UC Irvine, 2019.

122. Long, J.; Shelhamer, E.; Darrell, T. In *Fully convolutional networks for semantic segmentation*, Proceedings of the IEEE conference on computer vision and pattern recognition, 2015; pp 3431-3440.

123. Kang, E.; Min, J.; Ye, J. C., A deep convolutional neural network using directional wavelets for low-dose X-ray CT reconstruction. *Medical physics* **2017,** *44* (10), e360-e375.

124. Chen, H.; Zhang, Y.; Zhang, W.; Liao, P.; Li, K.; Zhou, J.; Wang, G., Low-dose CT via convolutional neural network. *Biomedical optics express* **2017,** *8* (2), 679-694.

125. Yang, W.; Zhang, H.; Yang, J.; Wu, J.; Yin, X.; Chen, Y.; Shu, H.; Luo, L.; Coatrieux, G.; Gui, Z., Improving low-dose CT image using residual convolutional network. *Ieee Access* **2017,** *5*, 24698-24705.

126. Kang, E.; Chang, W.; Yoo, J.; Ye, J. C., Deep convolutional framelet denosing for low-dose CT via wavelet residual network. *IEEE transactions on medical imaging* **2018,** *37* (6), 1358-1369.

127. Yang, Q.; Yan, P.; Zhang, Y.; Yu, H.; Shi, Y.; Mou, X.; Kalra, M. K.; Zhang, Y.; Sun, L.; Wang, G., Low-dose CT image denoising using a generative adversarial network with Wasserstein distance and perceptual loss. *IEEE transactions on medical imaging* **2018,** *37* (6), 1348-1357.

128. Wolterink, J. M.; Leiner, T.; Viergever, M. A.; Išgum, I., Generative adversarial networks for noise reduction in low-dose CT. *IEEE transactions on medical imaging* **2017,** *36* (12), 2536-2545.

129. Yi, X.; Babyn, P., Sharpness-aware low-dose CT denoising using conditional generative adversarial network. *Journal of digital imaging* **2018,** *31* (5), 655-669.

130.Ch en, H.; Zhang, Y.; Kalra, M. K.; Lin, F.; Chen, Y.; Liao, P.; Zhou, J.; Wang, G., Low-dose CT with a residual encoder-decoder convolutional neural network. *IEEE transactions on medical imaging* **2017,** *36* (12), 2524-2535.

131. Yu, F.; Koltun, V., Multi-scale context aggregation by dilated convolutions. *arXiv preprint arXiv:1511.07122* **2015**.

132. Wang, P.; Chen, P.; Yuan, Y.; Liu, D.; Huang, Z.; Hou, X.; Cottrell, G. In *Understanding convolution for semantic segmentation*, 2018 IEEE winter conference on applications of computer vision (WACV), IEEE: 2018; pp 1451-1460.

133. Bell, M. A. L.; Kuo, N.; Song, D. Y.; Boctor, E. M., Short-lag spatial coherence beamforming of photoacoustic images for enhanced visualization of prostate brachytherapy seeds. *Biomedical optics express* **2013,** *4* (10), 1964-1977.

134. Pourebrahimi, B.; Yoon, S.; Dopsa, D.; Kolios, M. C. In *Improving the quality of photoacoustic images using the short-lag spatial coherence imaging technique*, Photons Plus Ultrasound: Imaging and Sensing 2013, International Society for Optics and Photonics: 2013; p 85813Y.

135. Hill, E. R.; Xia, W.; Clarkson, M. J.; Desjardins, A. E., Identification and removal of laser-induced noise in photoacoustic imaging using singular value decomposition. *Biomedical optics express* **2017,** *8* (1), 68-77.

136. Reiter, A.; Bell, M. A. L. In *A machine learning approach to identifying point source locations in photoacoustic data*, Photons Plus Ultrasound: Imaging and Sensing 2017, International Society for Optics and Photonics: 2017; p 100643J.

137. Allman, D.; Reiter, A.; Bell, M. A. L., Photoacoustic source detection and reflection artifact removal enabled by deep learning. *IEEE transactions on medical imaging* **2018,** *37* (6), 1464-1477.

138. Anas, E. M. A.; Zhang, H. K.; Kang, J.; Boctor, E., Enabling fast and high quality LED photoacoustic imaging: a recurrent neural networks based approach. *Biomedical Optics Express* **2018,** *9* (8), 3852-3866.

139. Antholzer, S.; Haltmeier, M.; Schwab, J., Deep learning for photoacoustic tomography from sparse data. *Inverse problems in science and engineering* **2019,** *27* (7), 987-1005.

140. Anas, E. M. A.; Zhang, H. K.; Kang, J.; Boctor, E. M. In *Towards a Fast and Safe LED-Based Photoacoustic Imaging Using Deep Convolutional Neural Network*, International Conference on Medical Image Computing and Computer-Assisted Intervention, Springer: 2018; pp 159-167.

141. Liu, P.; Zhang, H.; Lian, W.; Zuo, W., Multi-level wavelet convolutional neural networks. *IEEE Access* **2019,** *7*, 74973-74985.

142. Bohndiek, S. E.; Bodapati, S.; Van De Sompel, D.; Kothapalli, S.-R.; Gambhir, S. S., Development and application of stable phantoms for the evaluation of photoacoustic imaging instruments. *PloS one* **2013,** *8* (9).

143. Yan, J.; Schaefferkoetter, J.; Conti, M.; Townsend, D., A method to assess image quality for low-dose PET: analysis of SNR, CNR, bias and image noise. *Cancer Imaging* **2016,** *16* (1), 26.

144. Suzuki, Y. J.; Forman, H. J.; Sevanian, A., Oxidants as stimulators of signal transduction. *Free Radical Biology and Medicine* **1997,** *22* (1-2), 269-285.

145. Gomes, A.; Fernandes, E.; Lima, J. L., Fluorescence probes used for detection of reactive oxygen species. *Journal of biochemical and biophysical methods* **2005,** *65* (2-3), 45-80.

146. Nathan, C.; Cunningham-Bussel, A., Beyond oxidative stress: an immunologist's guide to reactive oxygen species. *Nature Reviews Immunology* **2013,** *13* (5), 349.

147. Carden, D. L.; Granger, D. N., Pathophysiology of ischaemia–reperfusion injury. *The Journal of pathology* **2000,** *190* (3), 255-266.

148. Medzhitov, R., Origin and physiological roles of inflammation. *Nature* **2008,** *454* (7203), 428.

149. Soh, N.; Katayama, Y.; Maeda, M., A fluorescent probe for monitoring nitric oxide production using a novel detection concept. *Analyst* **2001,** *126* (5), 564-566.

150. Tanaka, K.; Miura, T.; Umezawa, N.; Urano, Y.; Kikuchi, K.; Higuchi, T.; Nagano, T., Rational design of fluorescein-based fluorescence probes. Mechanism-based design of a maximum fluorescence probe for singlet oxygen. *Journal of the American Chemical Society* **2001,** *123* (11), 2530-2536.

151. Pu, K.; Shuhendler, A. J.; Jokerst, J. V.; Mei, J.; Gambhir, S. S.; Bao, Z.; Rao, J., Semiconducting polymer nanoparticles as photoacoustic molecular imaging probes in living mice. *Nature nanotechnology* **2014,** *9* (3), 233.

152. Jiang, Y.; Pu, K., Advanced photoacoustic imaging applications of near-infrared absorbing organic nanoparticles. *Small* **2017,** *13* (30), 1700710.

153. Xie, C.; Zhen, X.; Lyu, Y.; Pu, K., Nanoparticle regrowth enhances photoacoustic signals of semiconducting macromolecular probe for in vivo imaging. *Advanced Materials* **2017,** *29* (44), 1703693.

154. Zhang, J.; Zhen, X.; Upputuri, P. K.; Pramanik, M.; Chen, P.; Pu, K., Activatable photoacoustic nanoprobes for in vivo ratiometric imaging of peroxynitrite. *Advanced Materials* **2017,** *29* (6), 1604764.

155. Lyu, Y.; Pu, K., Recent advances of activatable molecular probes based on semiconducting polymer nanoparticles in sensing and imaging. *Advanced Science* **2017,** *4* (6), 1600481.

156. Miao, Q.; Pu, K., Emerging designs of activatable photoacoustic probes for molecular imaging. *Bioconjugate chemistry* **2016,** *27* (12), 2808-2823.

157. Pu, K.; Cheng, P.; Zhang, J.; Huang, J.; Miao, Q.; Xu, C., Near-infrared Fluorescence Probes Detect Reactive Oxygen Species for Keloid Diagnosis. *Chemical Science* **2018**.

158. Link, S.; Burda, C.; Nikoobakht, B.; El-Sayed, M. A., Laser-induced shape changes of colloidal gold nanorods using femtosecond and nanosecond laser pulses. *The Journal of Physical Chemistry B* **2000,** *104* (26), 6152-6163.

159. Temma, T.; Onoe, S.; Kanazaki, K.; Ono, M.; Saji, H., Preclinical evaluation of a novel cyanine dye for tumor imaging with< italic< in vivo</italic< photoacoustic imaging. *Journal of biomedical optics* **2014,** *19* (9), 090501.

160. Onoe, S.; Temma, T.; Kanazaki, K.; Ono, M.; Saji, H., Development of photostabilized asymmetrical cyanine dyes for in vivo photoacoustic imaging of tumors. *Journal of biomedical optics* **2015,** *20* (9), 096006.

161. Schneider, C. A.; Rasband, W. S.; Eliceiri, K. W., NIH Image to ImageJ: 25 years of image analysis. *Nature methods* **2012,** *9* (7), 671.

162. Bist, G.; Pun, N. T.; Magar, T. B. T.; Shrestha, A.; Oh, H. J.; Khakurel, A.; Park, P.-H.; Lee, E.-S., Inhibition of LPS-stimulated ROS production by fluorinated and hydroxylated chalcones in RAW 264.7 macrophages with structure-activity relationship study. *Bioorganic & medicinal chemistry letters* **2017,** *27* (5), 1205-1209.

163. Choi, S.-Y.; Hwang, J.-H.; Ko, H.-C.; Park, J.-G.; Kim, S.-J., Nobiletin from citrus fruit peel inhibits the DNA-binding activity of NF-κB and ROS production in LPS-activated RAW 264.7 cells. *Journal of ethnopharmacology* **2007,** *113* (1), 149-155.

164. Lee, T.-Y.; Lee, K.-C.; Chen, S.-Y.; Chang, H.-H., 6-Gingerol inhibits ROS and iNOS through the suppression of PKC-α and NF-κB pathways in lipopolysaccharide-stimulated mouse macrophages. *Biochemical and biophysical research communications* **2009,** *382* (1), 134-139.

165. Eruslanov, E.; Kusmartsev, S., Identification of ROS using oxidized DCFDA and flow-cytometry. In *Advanced protocols in oxidative stress II*, Springer: 2010; pp 57-72.

166. Winterbourn, C. C.; Metodiewa, D., Reactivity of biologically important thiol compounds with superoxide and hydrogen peroxide. *Free Radical Biology and Medicine* **1999,** *27* (3-4), 322-328.

167. Varma, S. D.; Devamanoharan, P., Excretion of hydrogen peroxide in human urine. *Free radical research communications* **1990,** *8* (2), 73-78.

168. Varma, S.; Devamanoharan, P., Hydrogen peroxide in human blood. *Free radical research communications* **1991,** *14* (2), 125-131.

169. Giblin, F. J.; McCready, J. P.; Kodama, T.; Reddy, V. N., A direct correlation between the levels of ascorbic acid and H2O2 in aqueous humor. *Experimental eye research* **1984,** *38* (1), 87-93.

170. Liu, P.; Xu, B.; Quilley, J.; Wong, P. Y.-K., Peroxynitrite attenuates hepatic ischemia-reperfusion injury. *American Journal of Physiology-Cell Physiology* **2000,** *279* (6), C1970-C1977.

171. Shuhendler, A. J.; Pu, K.; Cui, L.; Uetrecht, J. P.; Rao, J., Real-time imaging of oxidative and nitrosative stress in the liver of live animals for drug-toxicity testing. *Nature biotechnology* **2014,** *32* (4), 373.

172. Kim, T.; Zhang, Q.; Li, J.; Zhang, L.; Jokerst, J. V., A Gold/Silver Hybrid Nanoparticle for Treatment and Photoacoustic Imaging of Bacterial Infection. *ACS nano* **2018**.

173. Mosquera, J. s.; García, I.; Liz-Marzán, L. M., Cellular uptake of nanoparticles versus small molecules: A matter of size. *Accounts of chemical research* **2018,** *51* (9), 2305-2313.

174. Chang, M. C.; Pralle, A.; Isacoff, E. Y.; Chang, C. J., A selective, cell-permeable optical probe for hydrogen peroxide in living cells. *Journal of the American Chemical Society* **2004,** *126* (47), 15392-15393.

175. Chan, J.; Dodani, S. C.; Chang, C. J., Reaction-based small-molecule fluorescent probes for chemoselective bioimaging. *Nature chemistry* **2012,** *4* (12), 973.

176. Lin, V. S.; Dickinson, B. C.; Chang, C. J., Boronate-based fluorescent probes: imaging hydrogen peroxide in living systems. In *Methods in enzymology*, Elsevier: 2013; Vol. 526, pp 19-43.

177. Karton-Lifshin, N.; Segal, E.; Omer, L.; Portnoy, M.; Satchi-Fainaro, R.; Shabat, D., A unique paradigm for a Turn-ON near-infrared cyanine-based probe: noninvasive intravital optical imaging of hydrogen peroxide. *Journal of the American Chemical Society* **2011,** *133* (28), 10960-10965.

178. Tang, Y.; Lee, D.; Wang, J.; Li, G.; Yu, J.; Lin, W.; Yoon, J., Development of fluorescent probes based on protection–deprotection of the key functional groups for biological imaging. *Chemical Society Reviews* **2015,** *44* (15), 5003-5015.

179. Sun, X.; Xu, Q.; Kim, G.; Flower, S. E.; Lowe, J. P.; Yoon, J.; Fossey, J. S.; Qian, X.; Bull, S. D.; James, T. D., A water-soluble boronate-based fluorescent probe for the selective detection of peroxynitrite and imaging in living cells. *Chemical Science* **2014,** *5* (9), 3368-3373.

180. Sikora, A.; Zielonka, J.; Lopez, M.; Joseph, J.; Kalyanaraman, B., Direct oxidation of boronates by peroxynitrite: mechanism and implications in fluorescence imaging of peroxynitrite. *Free Radical Biology and Medicine* **2009,** *47* (10), 1401-1407.

181. Zielonka, J.; Sikora, A.; Hardy, M.; Joseph, J.; Dranka, B. P.; Kalyanaraman, B., Boronate probes as diagnostic tools for real time monitoring of peroxynitrite and hydroperoxides. *Chemical research in toxicology* **2012,** *25* (9), 1793-1799.

182. Romero, N.; Denicola, A.; Radi, R., Red blood cells in the metabolism of nitric oxide-derived peroxynitrite. *IUBMB life* **2006,** *58* (10), 572-580.

183. Denicola, A.; Souza, J. M.; Radi, R., Diffusion of peroxynitrite across erythrocyte membranes. *Proceedings of the National Academy of Sciences* **1998,** *95* (7), 3566-3571.

184. Romero, N.; Denicola, A.; Souza, J. M.; Radi, R., Diffusion of peroxynitrite in the presence of carbon dioxide. *Archives of biochemistry and biophysics* **1999,** *368* (1), 23-30.

185. Jiang, L.-P.; Tu, Q.; Wang, Y.; Zhang, E., Ischemia-reperfusion injury-induced histological changes affecting early stage pressure ulcer development in a rat model. *Ostomy/wound management* **2011,** *57* (2), 55-60.

186. Eming, S. A.; Martin, P.; Tomic-Canic, M., Wound repair and regeneration: mechanisms, signaling, and translation. *Science translational medicine* **2014,** *6* (265), 265sr6-265sr6.

187. Han, G.; Ceilley, R., Chronic wound healing: a review of current management and treatments. *Advances in therapy* **2017,** *34* (3), 599-610.

188. Dumville, J. C.; Lipsky, B. A.; Hoey, C.; Cruciani, M.; Fiscon, M.; Xia, J., Topical antimicrobial agents for treating foot ulcers in people with diabetes. *Cochrane Database of Systematic Reviews* **2017,** (6).

189. Padula, W. V.; Mishra, M. K.; Makic, M. B. F.; Sullivan, P. W., Improving the quality of pressure ulcer care with prevention: a cost-effectiveness analysis. *Medical care* **2011**, 385-392.

190. Maione, A. G.; Brudno, Y.; Stojadinovic, O.; Park, L. K.; Smith, A.; Tellechea, A.; Leal, E. C.; Kearney, C. J.; Veves, A.; Tomic-Canic, M., Three-dimensional human tissue models that incorporate diabetic foot ulcer-derived fibroblasts mimic in vivo features of chronic wounds. *Tissue Engineering Part C: Methods* **2015,** *21* (5), 499-508.

191. Ahmed, A.; Goodwin, C.; Sarabia-Estrada, R.; Lay, F.; Ansari, A.; Steenbergen, C.; Pang, C.; Cohen, R.; Born, L.; Matsangos, A., A non-invasive method to produce pressure ulcers of varying severity in a spinal cord-injured rat model. *Spinal cord* **2016,** *54* (12), 1096-1104.

192. Reddy, M.; Gill, S. S.; Rochon, P. A., Preventing pressure ulcers: a systematic review. *Jama* **2006,** *296* (8), 974-984.

193. Brem, H.; Maggi, J.; Nierman, D.; Rolnitzky, L.; Bell, D.; Rennert, R.; Golinko, M.; Yan, A.; Lyder, C.; Vladeck, B., High cost of stage IV pressure ulcers. *The American Journal of Surgery* **2010,** *200* (4), 473-477.

194. Moore, Z. E.; Cowman, S., Repositioning for treating pressure ulcers. *Cochrane Database of Systematic Reviews* **2015,** (1).

195. McInnes, E.; Jammali-Blasi, A.; Bell-Syer, S. E.; Dumville, J. C.; Middleton, V.; Cullum, N., Support surfaces for pressure ulcer prevention. *Cochrane Database of Systematic Reviews* **2015,** (9).

196. Boyko, T. V.; Longaker, M. T.; Yang, G. P., Review of the current management of pressure ulcers. *Advances in wound care* **2018,** *7* (2), 57-67.

197. Nixon, J.; Cranny, G.; Bond, S., Pathology, diagnosis, and classification of pressure ulcers: comparing clinical and imaging techniques. *Wound repair and regeneration* **2005,** *13* (4), 365-372.

198. Whitney, J.; Phillips, L.; Aslam, R.; Barbul, A.; Gottrup, F.; Gould, L.; Robson, M. C.; Rodeheaver, G.; Thomas, D.; Stotts, N., Guidelines for the treatment of pressure ulcers. *Wound Repair and Regeneration* **2006,** *14* (6), 663-679.

199. Black, J.; Baharestani, M. M.; Cuddigan, J.; Dorner, B.; Edsberg, L.; Langemo, D.; Posthauer, M. E.; Ratliff, C.; Taler, G., National Pressure Ulcer Advisory Panel's updated pressure ulcer staging system. *Advances in skin & wound care* **2007,** *20* (5), 269-274.

200. Wassermann, E.; Van Griensven, M.; Gstaltner, K.; Oehlinger, W.; Schrei, K.; Redl, H., A chronic pressure ulcer model in the nude mouse. *Wound Repair and Regeneration* **2009,** *17* (4), 480-484.

201. Ayello, E. A.; Lyder, C. H., A new era of pressure ulcer accountability in acute care. *Advances in skin & wound care* **2008,** *21* (3), 134-140.

202. Wong, V., Skin blood flow response to 2-hour repositioning in long-term care residents: a pilot study. *Journal of Wound Ostomy & Continence Nursing* **2011,** *38* (5), 529-537.

203. Dittmar, A.; Pauchard, T.; Delhomme, G.; Vernet-Maury, E., A thermal conductivity sensor for the measurement of skin blood flow. *Sensors and actuators B: Chemical* **1992,** *7* (1-3), 327-331.

204. Swisher, S. L.; Lin, M. C.; Liao, A.; Leeflang, E. J.; Khan, Y.; Pavinatto, F. J.; Mann, K.; Naujokas, A.; Young, D.; Roy, S., Impedance sensing device enables early detection of pressure ulcers in vivo. *Nature communications* **2015,** *6*, ncomms7575.

205. Sigrist, R. M.; Liau, J.; El Kaffas, A.; Chammas, M. C.; Willmann, J. K., Ultrasound elastography: review of techniques and clinical applications. *Theranostics* **2017,** *7* (5), 1303.

206. Gehin, C.; Brusseau, E.; Meffre, R.; Schmitt, P.; Deprez, J.; Dittmar, A. In *Which techniques to improve the early detection and prevention of pressure ulcers?*, Engineering in Medicine and Biology Society, 2006. EMBS'06. 28th Annual International Conference of the IEEE, IEEE: 2006; pp 6057-6060.

207. Franchi-Abella, S.; Elie, C.; Correas, J.-M., Ultrasound elastography: advantages, limitations and artefacts of the different techniques from a study on a phantom. *Diagnostic and interventional imaging* **2013,** *94* (5), 497-501.

208. Synnevag, J. F.; Austeng, A.; Holm, S., Adaptive beamforming applied to medical ultrasound imaging. *IEEE transactions on ultrasonics, ferroelectrics, and frequency control* **2007,** *54* (8), 1606-1613.

209. Kolkman, R. G.; Brands, P. J.; Steenbergen, W.; van Leeuwen, T. G., Real-time in vivo photoacoustic and ultrasound imaging. *Journal of biomedical optics* **2008,** *13* (5), 050510.

210. Peirce, S. M.; Skalak, T. C.; Rodeheaver, G. T., Ischemia-reperfusion injury in chronic pressure ulcer formation: a skin model in the rat. *Wound repair and regeneration* **2000,** *8* (1), 68-76.

211. Reid, R. R.; Sull, A. C.; Mogford, J. E.; Roy, N.; Mustoe, T. A., A novel murine model of cyclical cutaneous ischemia-reperfusion injury. *Journal of Surgical Research* **2004,** *116* (1), 172-180.

212. Stadler, I.; Zhang, R.-Y.; Oskoui, P.; Whittaker, M. B. S.; Lanzafame, R. J., Development of a simple, noninvasive, clinically relevant model of pressure ulcers in the mouse. *Journal of Investigative Surgery* **2004,** *17* (4), 221-227.

213. Goldstein, B.; Sanders, J., Skin response to repetitive mechanical stress: a new experimental model in pig. *Archives of physical medicine and rehabilitation* **1998,** *79* (3), 265-272.

214. Dinsdale, S. M., Decubitus ulcers in swine: light and electron microscopy study of pathogenesis. *Archives of physical medicine and rehabilitation* **1973,** *54* (2), 51-6 passim.

215. Salcido, R.; Donofrio, J.; Fisher, S. B.; LeGrand, E. K.; Dickey, K.; Carney, J. M.; Schosser, R.; Liang, R., Histopathology of pressure ulcers as a result of sequential computer-controlled pressure sessions in a fuzzy rat model. *Advances in wound care: the journal for prevention and healing* **1994,** *7* (5), 23-4, 26, 28 passim.

216. Zhu, Y.; Xu, G.; Yuan, J.; Jo, J.; Gandikota, G.; Demirci, H.; Agano, T.; Sato, N.; Shigeta, Y.; Wang, X., Light emitting diodes based photoacoustic imaging and potential clinical applications. *Scientific reports* **2018,** *8* (1), 9885.

217. Krouskop, T. A., A synthesis of the factors that contribute to pressure sore formation. *Medical hypotheses* **1983,** *11* (2), 255-267.

218. Lowthian, P., A review of pressure sore pathogenesis. *Nursing times* **1982,** *78* (3), 117.

219. Smith, D. M., Pressure ulcers in the nursing home. *Annals of internal medicine* **1995,** *123* (6), 433-438.

220. Wang, X.; Chamberland, D. L.; Jamadar, D. A., Noninvasive photoacoustic tomography of human peripheral joints toward diagnosis of inflammatory arthritis. *Optics letters* **2007,** *32* (20), 3002-3004.

221. Zhu, Y.; Johnson, L. A.; Huang, Z.; Rubin, J. M.; Yuan, J.; Lei, H.; Ni, J.; Wang, X.; Higgins, P. D.; Xu, G., Identifying intestinal fibrosis and inflammation by spectroscopic photoacoustic imaging: an animal study in vivo. *Biomedical optics express* **2018,** *9* (4), 1590-1600.

222. Kasuya, A.; Sakabe, J.-i.; Tokura, Y., Potential application of in vivo imaging of impaired lymphatic duct to evaluate the severity of pressure ulcer in mouse model. *Scientific reports* **2014,** *4*, 4173.

223. Aoi, N.; Yoshimura, K.; Kadono, T.; Nakagami, G.; Iizuka, S.; Higashino, T.; Araki, J.; Koshima, I.; Sanada, H., Ultrasound assessment of deep tissue injury in pressure ulcers: possible prediction of pressure ulcer progression. *Plastic and reconstructive surgery* **2009,** *124* (2), 540-550.

224. Stekelenburg, A.; Oomens, C.; Strijkers, G.; Nicolay, K.; Bader, D., Compression-induced deep tissue injury examined with magnetic resonance imaging and histology. *Journal of applied physiology* **2006,** *100* (6), 1946-1954.

225. Yudovsky, D.; Nouvong, A.; Pilon, L., Hyperspectral imaging in diabetic foot wound care. SAGE Publications Sage CA: Los Angeles, CA: 2010.

226. Ruan, C. M.; Escobedo, E.; Harrison, S.; Goldstein, B., Magnetic resonance imaging of nonhealing pressure ulcers and myocutaneous flaps. *Archives of physical medicine and rehabilitation* **1998,** *79* (9), 1080-1088.

227. Nguyen, H. N. Y.; Hussain, A.; Steenbergen, W., Reflection artifact identification in photoacoustic imaging using multi-wavelength excitation. *Biomedical optics express* **2018,** *9* (10), 4613-4630.

228. Tilgner, R., Photoacoustic spectroscopy with light scattering samples. *Applied optics* **1981,** *20* (21), 3780-3786.

229. Helander, P.; Lundström, I.; McQueen, D., Light scattering effects in photoacoustic spectroscopy. *Journal of Applied Physics* **1980,** *51* (7), 3841-3847.

230. Bu, S.; Liu, Z.; Shiina, T.; Kondo, K.; Yamakawa, M.; Fukutani, K.; Someda, Y.; Asao, Y., Model-based reconstruction integrated with fluence compensation for photoacoustic tomography. *IEEE Transactions on Biomedical Engineering* **2012,** *59* (5), 1354-1363.

231. Daoudi, K.; Hussain, A.; Hondebrink, E.; Steenbergen, W., Correcting photoacoustic signals for fluence variations using acousto-optic modulation. *Optics express* **2012,** *20* (13), 14117-14129.

232. Zhao, L.; Yang, M.; Jiang, Y.; Li, C., Optical fluence compensation for handheld photoacoustic probe: An in vivo human study case. *Journal of Innovative Optical Health Sciences* **2017,** *10* (04), 1740002.

233. Wang, L. V.; Hu, S., Photoacoustic tomography: in vivo imaging from organelles to organs. *Science* **2012,** *335* (6075), 1458-62.

234. Neuschler, E. I.; Butler, R.; Young, C. A.; Barke, L. D.; Bertrand, M. L.; Bohm-Velez, M.; Destounis, S.; Donlan, P.; Grobmyer, S. R.; Katzen, J.; Kist, K. A.; Lavin, P. T.; Makariou, E. V.; Parris, T. M.; Schilling, K. J.; Tucker, F. L.; Dogan, B. E., A Pivotal Study of Optoacoustic

Imaging to Diagnose Benign and Malignant Breast Masses: A New Evaluation Tool for Radiologists. *Radiology* **2018,** *287* (2), 398-412.

235. Manohar, S.; Dantuma, M., Current and future trends in photoacoustic breast imaging. *Photoacoustics* **2019,** *16*, 100134.

236. Lin, C. Y.; Chen, F.; Hariri, A.; Chen, C. J.; Wilder-Smith, P.; Takesh, T.; Jokerst, J. V., Photoacoustic Imaging for Noninvasive Periodontal Probing Depth Measurements. *J Dent Res* **2018,** *97* (1), 23-30.

237. Jo, J.; Xu, G.; Cao, M.; Marquardt, A.; Francis, S.; Gandikota, G.; Wang, X., A Functional Study of Human Inflammatory Arthritis Using Photoacoustic Imaging. *Sci Rep* **2017,** *7* (1), 15026.

238. Su, J.; Karpiouk, A.; Wang, B.; Emelianov, S., Photoacoustic imaging of clinical metal needles in tissue. *Journal of biomedical optics* **2010,** *15* (2), 021309.

239. Gargiulo, S.; Albanese, S.; Mancini, M., State-of-the-Art Preclinical Photoacoustic Imaging in Oncology: Recent Advances in Cancer Theranostics. *Contrast media & molecular imaging* **2019,** *2019*, 5080267.

240. International Electrotechnical Commission, IEC 61391-1:2017, Ultrasonics – Pulse-echo scanners – Part 1: Techniques for calibrating spatial measurement systems and measurement of system point-spread function response. Geneva, Switzerland, 2017.

241. Goodsitt, M. M.; Carson, P. L.; Witt, S.; Hykes, D. L.; Kofler, J. M., Jr., Real-time B-mode ultrasound quality control test procedures. Report of AAPM Ultrasound Task Group No. 1. *Med Phys* **1998,** *25* (8), 1385-406.

242. Rieffel, J.; Chen, F.; Kim, J.; Chen, G.; Shao, W.; Shao, S.; Chitgupi, U.; Hernandez, R.; Graves, S. A.; Nickles, R. J.; Prasad, P. N.; Kim, C.; Cai, W.; Lovell, J. F., Hexamodal imaging with porphyrin-phospholipid-coated upconversion nanoparticles. *Adv Mater* **2015,** *27* (10), 1785-90.

243. Kothapalli, S. R.; Ma, T. J.; Vaithilingam, S.; Oralkan, O.; Khuri-Yakub, B. T.; Gambhir, S. S., Deep tissue photoacoustic imaging using a miniaturized 2-D capacitive micromachined ultrasonic transducer array. *IEEE transactions on bio-medical engineering* **2012,** *59* (5), 1199-204.

244. Pramanik, M.; Swierczewska, M.; Green, D.; Sitharaman, B.; Wang, L. V., Single-walled carbon nanotubes as a multimodal-thermoacoustic and photoacoustic-contrast agent. *J Biomed Opt* **2009,** *14* (3), 034018.

245. Zhang, E.; Laufer, J.; Beard, P., Backward-mode multiwavelength photoacoustic scanner using a planar Fabry-Perot polymer film ultrasound sensor for high-resolution three-dimensional imaging of biological tissues. *Applied optics* **2008,** *47* (4), 561-77.

246. Cook, J. R.; Bouchard, R. R.; Emelianov, S. Y., Tissue-mimicking phantoms for photoacoustic and ultrasonic imaging. *Biomed Opt Express* **2011,** *2* (11), 3193-206.

247. Chen, Y. S.; Frey, W.; Kim, S.; Kruizinga, P.; Homan, K.; Emelianov, S., Silica-coated gold nanorods as photoacoustic signal nanoamplifiers. *Nano Lett* **2011,** *11* (2), 348-54.

248. Karpiouk, A. B.; Aglyamov, S. R.; Mallidi, S.; Shah, J.; Scott, W. G.; Rubin, J. M.; Emelianov, S. Y., Combined ultrasound and photoacoustic imaging to detect and stage deep vein thrombosis: phantom and ex vivo studies. *Journal of biomedical optics* **2008,** *13* (5), 054061.

249. Ding, L.; Luis Dean-Ben, X.; Lutzweiler, C.; Razansky, D.; Ntziachristos, V., Efficient non-negative constrained model-based inversion in optoacoustic tomography. *Phys Med Biol* **2015,** *60* (17), 6733-50.

250. Avigo, C.; Di Lascio, N.; Armanetti, P.; Kusmic, C.; Cavigli, L.; Ratto, F.; Meucci, S.; Masciullo, C.; Cecchini, M.; Pini, R.; Faita, F.; Menichetti, L., Organosilicon phantom for photoacoustic imaging. *J Biomed Opt* **2015,** *20* (4), 46008.

251. Levi, J.; Kothapalli, S. R.; Bohndiek, S.; Yoon, J. K.; Dragulescu-Andrasi, A.; Nielsen, C.; Tisma, A.; Bodapati, S.; Gowrishankar, G.; Yan, X.; Chan, C.; Starcevic, D.; Gambhir, S. S., Molecular photoacoustic imaging of follicular thyroid carcinoma. *Clin Cancer Res* **2013,** *19* (6), 1494-502.

252. Kim, G.; Huang, S. W.; Day, K. C.; O'Donnell, M.; Agayan, R. R.; Day, M. A.; Kopelman, R.; Ashkenazi, S., Indocyanine-green-embedded PEBBLEs as a contrast agent for photoacoustic imaging. *J Biomed Opt* **2007,** *12* (4), 044020.

253. Xia, W.; Piras, D.; Heijblom, M.; Steenbergen, W.; van Leeuwen, T. G.; Manohar, S., Poly(vinyl alcohol) gels as photoacoustic breast phantoms revisited. *Journal of biomedical optics* **2011,** *16* (7), 075002.

254. Bohndiek, S. E.; Bodapati, S.; Van De Sompel, D.; Kothapalli, S. R.; Gambhir, S. S., Development and application of stable phantoms for the evaluation of photoacoustic imaging instruments. *PLoS One* **2013,** *8* (9), e75533.

255. Spirou, G. M.; Oraevsky, A. A.; Vitkin, I. A.; Whelan, W. M., Optical and acoustic properties at 1064 nm of polyvinyl chloride-plastisol for use as a tissue phantom in biomedical optoacoustics. *Physics in medicine and biology* **2005,** *50* (14), N141-53.

256. Vieira, S. L.; Pavan, T. Z.; Junior, J. E.; Carneiro, A. A., Paraffin-gel tissue-mimicking material for ultrasound-guided needle biopsy phantom. *Ultrasound in medicine & biology* **2013,** *39* (12), 2477-84.

257. Maneas, E.; Xia, W.; Ogunlade, O.; Fonseca, M.; Nikitichev, D. I.; David, A. L.; West, S. J.; Ourselin, S.; Hebden, J. C.; Vercauteren, T.; Desjardins, A. E., Gel wax-based tissue-mimicking phantoms for multispectral photoacoustic imaging. *Biomed Opt Express* **2018,** *9* (3), 1151-1163.

258. Cabrelli, L. C.; Pelissari, P. I.; Deana, A. M.; Carneiro, A. A.; Pavan, T. Z., Stable phantom materials for ultrasound and optical imaging. *Physics in medicine and biology* **2017,** *62* (2), 432-447.

259. Laufer, J.; Zhang, E.; Beard, P., Evaluation of absorbing chromophores used in tissue phantoms for quantitative photoacoustic spectroscopy and imaging. *IEEE journal of selected topics in quantum electronics* **2010,** *16* (3), 600-607.

260. Manohar, S.; Kharine, A.; van Hespen, J. C.; Steenbergen, W.; van Leeuwen, T. G., Photoacoustic mammography laboratory prototype: imaging of breast tissue phantoms. *J Biomed Opt* **2004,** *9* (6), 1172-81.

261. Zell, K.; Sperl, J. I.; Vogel, M. W.; Niessner, R.; Haisch, C., Acoustical properties of selected tissue phantom materials for ultrasound imaging. *Phys Med Biol* **2007,** *52* (20), N475-N484.

262. Vogt, W. C.; Jia, C.; Wear, K. A.; Garra, B. S.; Pfefer, T. J., Phantom-based image quality test methods for photoacoustic imaging systems. *Journal of biomedical optics* **2017,** *22* (9), 1-14.

263. Vogt, W. C.; Jia, C.; Wear, K. A.; Garra, B. S.; Joshua Pfefer, T., Biologically relevant photoacoustic imaging phantoms with tunable optical and acoustic properties. *J Biomed Opt* **2016,** *21* (10), 101405.

264. Jia, C.; Vogt, W. C.; Wear, K. A.; Pfefer, T. J.; Garra, B. S., Two-layer heterogeneous breast phantom for photoacoustic imaging. *Journal of biomedical optics* **2017,** *22* (10), 1-14.

265. Moustafa B. Zerhouni, M. R. Ultrasonic calibration material and method. US Patent No. 5196343, 1990.

266. Klinkosz, T.; Lewa, C. J.; Paczkowski, J., Propagation velocity and attenuation of a shear wave pulse measured by ultrasound detection in agarose and polyacrylamide gels. *Ultrasound Med Biol* **2008,** *34* (2), 265-75.

267. Zell, K.; Sperl, J. I.; Vogel, M. W.; Niessner, R.; Haisch, C., Acoustical properties of selected tissue phantom materials for ultrasound imaging. *Physics in medicine and biology* **2007,** *52* (20), N475-84.

268. Lafon, C.; Zderic, V.; Noble, M. L.; Yuen, J. C.; Kaczkowski, P. J.; Sapozhnikov, O. A.; Chavrier, F.; Crum, L. A.; Vaezy, S., Gel phantom for use in high-intensity focused ultrasound dosimetry. *Ultrasound Med Biol* **2005,** *31* (10), 1383-9.

269. Choi, M. J.; Guntur, S. R.; Lee, K. I.; Paeng, D. G.; Coleman, A., A tissue mimicking polyacrylamide hydrogel phantom for visualizing thermal lesions generated by high intensity focused ultrasound. *Ultrasound Med Biol* **2013,** *39* (3), 439-48.

270. Guntur, S. R.; Choi, M. J., An improved tissue-mimicking polyacrylamide hydrogel phantom for visualizing thermal lesions with high-intensity focused ultrasound. *Ultrasound Med Biol* **2014,** *40* (11), 2680-91.

271. Wilson, K.; Homan, K.; Emelianov, S., Biomedical photoacoustics beyond thermal expansion using triggered nanodroplet vaporization for contrast-enhanced imaging. *Nat Commun* **2012,** *3*, 618.

272. Hannah, A. S.; VanderLaan, D.; Chen, Y. S.; Emelianov, S. Y., Photoacoustic and ultrasound imaging using dual contrast perfluorocarbon nanodroplets triggered by laser pulses at 1064 nm. *Biomedical optics express* **2014,** *5* (9), 3042-52.

273. Sandell, J. L.; Zhu, T. C., A review of in-vivo optical properties of human tissues and its impact on PDT. *J Biophotonics* **2011,** *4* (11-12), 773-87.

274. International Electrotechnical Commission, IEC 61391-2:2010, "Ultrasonics – Pulse-echo scanners – Part 2: Measurement of maximum depth of penetration and local dynamic range. Geneva, Switzerland, 2010.

275. Oppermann, W.; Rose, S.; Rehage, G., The elastic behaviour of hydrogels. *British polymer journal* **1985,** *17* (2), 175-180.

276. Lee, Y. C.; Fullerton, G. D.; Baiu, C.; Lescrenier, M. G.; Goins, B. A., Preclinical multimodality phantom design for quality assurance of tumor size measurement. *BMC Med Phys* **2011,** *11*, 1.

277. Madsen, E. L.; Frank, G. R.; Krouskop, T. A.; Varghese, T.; Kallel, F.; Ophir, J., Tissue-mimicking oil-in-gelatin dispersions for use in heterogeneous elastography phantoms. *Ultrasonic Imaging* **2003,** *25* (1), 17-38.

278. Cook, J. R.; Bouchard, R. R.; Emelianov, S. Y., Tissue-mimicking phantoms for photoacoustic and ultrasonic imaging. *Biomedical optics express* **2011,** *2* (11), 3193-3206.

279. Culjat, M. O.; Goldenberg, D.; Tewari, P.; Singh, R. S., A review of tissue substitutes for ultrasound imaging. *Ultrasound in medicine & biology* **2010,** *36* (6), 861-873.

280. Wear, K. A., Measurements of phase velocity and group velocity in human calcaneus. *Ultrasound in medicine & biology* **2000,** *26* (4), 641-646.

281. Wear, K. A., Mechanisms of Interaction of Ultrasound With Cancellous Bone: A Review. *IEEE transactions on ultrasonics, ferroelectrics, and frequency control* **2020,** *67* (3), 454-482.

282. Maruvada, S.; Liu, Y.; Gammell, P.; Wear, K., Broadband characterization of plastic and high intensity therapeutic ultrasound phantoms using time delay spectrometry-With validation using Kramers-Kronig relations. *J Acoust Soc Am* **2018,** *143* (6), 3365.

283. Kinsler, L. E.; Frey, A. R.; Coppens, A. B.; Sanders, J. V., Fundamentals of Acoustics. 3rd ed.; John Wiley and Sons: New York, 1982.

284. Dai, X.; Yang, H.; Jiang, H., In vivo photoacoustic imaging of vasculature with a low-cost miniature light emitting diode excitation. *Optics letters* **2017,** *42* (7), 1456-1459.

285. Akarcay, H. G.; Preisser, S.; Frenz, M.; Ricka, J., Determining the optical properties of a gelatin-TiO_2 phantom at 780 nm. *Biomedical optics express* **2012,** *3* (3), 418-34.

286. Prahl, S. A.; Van Gemert, M. J. C.; Welch, A. J., Determining the Optical-Properties of Turbid Media by Using the Adding-Doubling Method. *Appl Optics* **1993,** *32* (4), 559-568.

287. Prahl, S. A. Inverse Adding-Doubling. https://omlc.org/software/iad/ (accessed September 8).

288. Ghassemi, P.; Wang, J.; Melchiorri, A. J.; Ramella-Roman, J. C.; Mathews, S. A.; Coburn, J. C.; Sorg, B. S.; Chen, Y.; Pfefer, T. J., Rapid prototyping of biomimetic vascular phantoms for hyperspectral reflectance imaging. *J Biomed Opt* **2015,** *20* (12), 121312.

289. Fonseca, M.; Zeqiri, B.; Beard, P. C.; Cox, B. T., Characterisation of a phantom for multiwavelength quantitative photoacoustic imaging. *Phys Med Biol* **2016,** *61* (13), 4950-73.

290. Hale, G. M.; Querry, M. R., Optical Constants of Water in the 200-nm to 200-microm Wavelength Region. *Appl Opt* **1973,** *12* (3), 555-63.

291. Byron, M. L.; Variano, E. A., Refractive-index-matched hydrogel materials for measuring flow-structure interactions. *Exp Fluids* **2013,** *54* (2).

292. Walker, H. K.; Hall, W. D.; Hurst, J. W., *Clinical Methods: The History, Physical and Laboratory Examinations*. 3rd ed.; Butterworth-Heinemann: St. Louis, MO, 1990.

293. Hariri, A.; Wang, J.; Kim, Y.; Jhunjhunwala, A.; Chao, D. L.; Jokerst, J. V., In vivo photoacoustic imaging of chorioretinal oxygen gradients. *Journal of biomedical optics* **2018,** *23* (3), 1-8.

294. Daigle, R. E. Ultrasound imaging system with pixel oriented processing. CN-101203183-B, 2015.

295. Thijssen, J. M.; Weijers, G.; de Korte, C. L., Objective performance testing and quality assurance of medical ultrasound equipment. *Ultrasound in medicine & biology* **2007,** *33* (3), 460-71.

296. Dahl, J. J.; Hyun, D.; Lediju, M.; Trahey, G. E., Lesion detectability in diagnostic ultrasound with short-lag spatial coherence imaging. *Ultrasonic imaging* **2011,** *33* (2), 119-33.

297. Zhou, X.; Akhlaghi, N.; Wear, K. A.; Garra, B. S.; Pfefer, T. J.; Vogt, W. C., Evaluation of Fluence Correction Algorithms in Multispectral Photoacoustic Imaging. *Photoacoustics* **2020,** *19*, 100181.

298. Barrett, H. H.; Myers, K. J.; Hoeschen, C.; Kupinski, M. A.; Little, M. P., Task-based measures of image quality and their relation to radiation dose and patient risk. *Physics in medicine and biology* **2015,** *60* (2), R1-75.

299. CIRS Inc. www.cirsinc.com/support/faq (accessed September 8).